

Alumination of Porous Silica and Quantitative Investigation of Factors Influencing Water and Methanol Adsorption

Von der Fakultät Chemie der Universität Stuttgart

zur Erlangung der Würde eines Doktors der Naturwissenschaften (Dr. rer. nat.)

genehmigte Abhandlung

vorgelegt von

Zheng Li

aus Shanxi, China

Hauptberichter: Jun.-Prof. Dr. Deven Estes

Mitberichter: Prof. Dr.-Ing. Elias Klemm

Prüfungsvorsitzender: Prof. Dr. rer. nat. Thomas Schleid

Tag der mündlichen Prüfung: 29.09.2022

Institut für Technische Chemie der Universität Stuttgart

2022

Erklärung über die Eigenständigkeit der Dissertation

Ich versichere, dass ich die vorliegende Arbeit mit dem Titel

“Alumination of Porous Silica and Quantitative Investigation of Factors Influencing Water and Methanol Adsorption”

selbständig verfasst und keine anderen als die angegebenen Quellen und Hilfsmittel benutzt habe; aus fremden Quellen entnommene Passagen und Gedanken sind als solche kenntlich gemacht.

Declaration of Authorship

I hereby certify that the dissertation entitled

“Alumination of Porous Silica and Quantitative Investigation of Factors Influencing Water and Methanol Adsorption”

is entirely my own work except where otherwise indicated. Passages and ideas from other sources have been clearly indicated.

Name/Name: _____

Unterschrift/Signed: _____

Datum/Date: _____

Contents

1. Zusammenfassung	1
2. Abstract	5
3. The Aims of the Work	8
4. Introduction	10
4.1 Introduction of Silica Materials	10
4.1.1 Introduction of Porous Silica	10
4.1.2 Introduction of Non-porous Silica	15
4.2 Introduction of Solid-state NMR Spectroscopy.....	16
4.2.1 Principles of Solid-state NMR Spectroscopy	16
4.2.2 Magic-Angel Spinning Technique.....	19
4.2.3 Cross-polarization Technique	19
4.3 Introduction of DRIFTS.....	21
4.4 Introduction of TGA-DSC	23
5. Experimental	24
5.1 Materials Preparation	24
5.1.1 Synthesis of Silicalite.....	25
5.1.2 Synthesis of SBA-15.....	25
5.1.3 Synthesis of SBA-16.....	25
5.1.4 Preparation of Silica Supported Silicotungstic Acid	25
5.1.5 Alumination of Silica Materials.....	26
5.1.6 Ion Exchange Method	26
5.1.7 Sample Activation.....	27
5.1.8 Summary of Porous and Non-porous Materials.....	27
5.2 Characterization Method.....	28
5.2.1 Saturation and Desorption of Water and Methanol	28
5.2.2 Loading of Basic Probe Molecules	30
5.2.3 Solid-state NMR spectroscopy	30
5.2.4 In-situ Diffuse Reflectance Infrared Fourier Transform Spectroscopy	32
5.2.5 TGA-DSC	32

5.2.6 Nitrogen Physisorption	34
5.2.7 X-ray Diffraction	34
5.2.8 Chemical Analysis	34
5.2.9 Scanning Electron Microscopy	35
5.2.10 Transmission Electron Microscopy	35
6. The Alumination of Porous Silica with Sodium Aluminate.....	36
6.1 Introduction.....	36
6.2 Physicochemical Characterization	38
6.3 Mechanism of Alumination	49
6.3.1 Parent materials.....	50
6.3.2 Transform into as-synthesized materials	52
6.3.3 Transform into Na-form materials	55
6.3.4 Transformation into H-form materials.....	59
6.3.5 Summary of Alumination Mechanism.....	60
6.4 Acid Properties of Aluminated Materials	62
6.5 Conclusions.....	68
7. Binding Sites and Strength of Water and Methanol in Micro- and Mesoporous Materials	70
7.1 Introduction.....	70
7.2 Physicochemical Characterization	72
7.3 Adsorption Sites for Water and Methanol	75
7.3.1 Adsorption Sites on Siliceous Materials	76
7.3.2 Adsorption Sites on Na-form Materials.....	78
7.3.3 Adsorption Sites on H-form Materials.....	81
7.4 Desorption Enthalpies of Water and Methanol Species	82
7.5 Conclusions.....	84
8. Influence of Confinement and Surface Sites on Methanol Adsorption ..	85
8.1 Introduction.....	85
8.2 Physicochemical Characterization	87
8.3 Methanol on Siliceous Materials	89
8.4 Methanol on Na-form Materials	94

8.5 Methanol on H-form Materials	97
8.6 Influence of Material Surface Groups and Confinement.....	104
8.7 Conclusions.....	106
9. Influence of Confinement and Surface Sites on Water Adsorption.....	107
9.1 Introduction.....	107
9.2 Water on Siliceous Materials	109
9.3 Water on Na-form Materials.....	114
9.4 Water on H-form Materials.....	119
9.5 Influence of Material Surface Groups and Confinement and Comparing with Methanol Adsorption.....	124
9.6 Conclusions.....	126
10. Conclusions and Outlook	127
References	129

List of Publications

Acknowledgment

Curriculum Vitae

Abbreviation and symbols

Abbreviations

1D	One-dimensional
2D	Two-dimensional
3D	Three-dimensional
A200	Aerosil® 200
Al ^{IV}	Tetrahedrally coordinated aluminum
Al ^V	Pentahedrally coordinated aluminum
Al ^{VI}	Octahedrally coordinated aluminum
atom%-D	Atomic ratio of deuteration
BAS	Brønsted acid sites
BET	Brunauer-Emmett-Teller
BJH	Barrett-Joyner-Halenda
CP	Cross polarization
DeA-Y	Dealuminated Y zeolite
DME	Dimethyl ether
DRIFTS	Diffuse reflectance infrared Fourier transform spectroscopy
DSC	Differential scanning calorimetry
EFAI	Extra-framework aluminum
FCC	Fluid catalytic cracking
HPA	Heteropoly acid
ICP-OES	Inductively coupled plasma optical emission spectrometry
LAS	Lewis acid sites
MAS	Magic angle spinning
MB	Membered
MQ	Multi-quantum
MTH	Methanol-to-hydrocarbons
MTO	Methanol-to-olefins
NMR	Nuclear magnetic resonance
NP	Nanoparticle
SEM	Scanning electron Microscopy

SMS	Surface methoxy species
SS	Solid-state
STA	Silicotungstic acid
TEM	Transmission electron microscopy
TEOS	Tetraethyl orthosilicate
TGA	Thermogravimetric analysis
TMPO	Trimethylphosphine oxide
TPABr	Tetrapropylammonium bromide
TRAPDOR	Transfer of populations in double resonance
USY	Ultra-stable Y zeolite
wt. %	Mass fraction
XRD	X-ray diffraction

Symbols

B	T	Magnetic field
C_q	MHz	Quadrupolar coupling constant
ΔE	kJ	Total energy upon desorption
\hat{H}	-	Hamilton Operator
ΔH	kJ·mol ⁻¹	Desorption heat
I	-	Nuclear spin
k	-	Absorption coefficient
m	g	Mass
M	mol·L ⁻¹	Solution concentration
n	mmol·g ⁻¹	Concentration of atoms, molecules, or surface sites
p	Pa	Pressure
R_∞	-	Diffuse reflectance
s	-	Scattering coefficient
t	s	Time
T	K	Temperature
V_{meso}	mL·g ⁻¹	Mesopore volume
V_{micro}	mL·g ⁻¹	Micropore volume
α, β	-	Euler angles
γ	s ⁻¹ ·a ⁻¹ ·m	Gyromagnetic ratio
δ	ppm	Chemical shift
η	-	Asymmetry parameter
σ_{CP}	s	Contact time
ω	s ⁻¹	Angular frequency

1. Zusammenfassung

Wechselwirkungen zwischen der Oberfläche fester Katalysatoren und den darauf adsorbierten Reaktanten bestimmen die katalytische Leistung in chemischen Reaktionen entscheidend mit. Daher ist das Verständnis solcher Wechselwirkungen entscheidend für die rationale Gestaltung fester Katalysatoren und die Optimierung der Produktverteilung. In dieser Dissertation werden die folgenden drei Unterthemen erörtert: (1) Einbringung von Aluminium in rein siliziumhaltige Materialien mit Hilfe von Natriumaluminat (NaAlO_2); (2) Identifizierung von Bindungsstellen und Messung der Bindungsenergien von Wasser im Vergleich zu Methanol, das auf mikro- und mesoporösen Materialien adsorbiert wird; (3) Aufklärung des Einflusses der definierten Geometrien der Poren auf die Adsorption von Wasser und Methanol.

Die Aluminierung von porösem Siliziumdioxid mit Natriumaluminat

Im ersten Teil (Kapitel 6) wurde der Mechanismus der NaAlO_2 -Modifikation an mikro- und mesoporösen Materialien (DeA-Y Zeolith, SBA-15 und SBA-16) untersucht. Die hergestellten Ionenaustauscher und Katalysatoren mit Säurezentren werden mittels Festkörper-NMR bei Rotation um den magischen Winkel (MAS) untersucht. Die alkalische NaAlO_2 -Lösung ist in der Lage die Silikatoberfläche teilweise aufzulösen. Dies geht mit der Bildung von $\text{Si}(\text{OH})_x$ -Gruppen ($x=1$ bis 3) einher. Einige dieser Gruppen reagieren anschließend mit NaAlO_2 und bilden das tetraedrische Aluminium, das als Gerüstaluminium bekannt ist. Eine Ausnahme stellt SBA-16 dar, da es auch Aluminium außerhalb des Gerüsts bildet, sogenanntes „Extra-Gerüstaluminium“. Die Aluminierungsleistung, d. h. die Menge des tetraedrisch eingebauten Gerüstaluminiums, hängt von der Behandlungstemperatur, dem Porendurchmesser und der Porenstruktur der Silikate ab. Diese Modifikation funktioniert am besten bei SBA-15 mit seiner hexagonalen Porenstruktur. Fast jedes eingebrachte Aluminiumatom führt hier zur Bildung eines Zentrums für den Austausch von Kationen. Allerdings können weniger als 20% dieser Zentren in Brønsted-Säure-Zentren (BAS) umgewandelt werden, da ein Teil des tetraedrischen Aluminiums bei der Kalzinierung in pentaedrisch koordiniertes Gerüstaluminium oder in oktaedrisch koordiniertes Extra-Gerüstaluminium übergeht. Die Säurezentrendichte und -Stärke wurden durch das Einbringen von Sondenmolekülen wie Ammoniak, Acetonitril und TMPO untersucht. Die auf den mesoporösen Materialien gebildeten BAS sind schwach und können nur durch starke

1. Zusammenfassung

Basenmoleküle nachgewiesen werden. Dies ist auf die flexible Koordination zwischen Si(OH)-Gruppen und tetraedrischen Aluminiumarten zurückzuführen. Auf mikroporösem DeA-Y-Zeolith werden starke BAS gebildet, die denjenigen ähneln, die in direkt synthetisiertem Zeolith gefunden werden. Die TMPO-Beladung in Verbindung mit der ^{31}P -MAS-NMR-Spektroskopie deutet auf das Vorhandensein verschiedener Brønsted- und Lewis-Säure-Zentren auf den H-Form Materialien hin.

Adsorptions-Zentren und Stärke der Adsorption von Wasser und Methanol an mikro- und mesoporösen Materialien

Im zweiten Teil (Kapitel 7) wurden die Adsorptionszentren von Wasser und Methanol auf Silikaten und Alumosilikaten, wie mikroporösen ZSM-5-Zeolithen und mesoporösen SBA-15-Materialien, mittels MAS-NMR-Spektroskopie und TGA-DSC untersucht. Bei siliziumhaltigem Silikalit und SBA-15 zeigen ^{29}Si -MAS-NMR-Studien, dass Silanolgruppen die wichtigsten Adsorptionsstellen für Wasser und Methanol sind. Wir beobachten eine stärkere Wechselwirkung mit Si(OH)-Gruppen vom Typ Q^3 für Methanol im Vergleich zu Wasser. Geminale Si(OH)-Gruppe des Typs Q^2 auf SBA-15 erhöhen dessen Hydrophilie. ^{23}Na -MAS-NMR-Spektren belegen die starke Wechselwirkung von Na^+ Kationen mit Wasser- oder Methanolköleülen auf Na-ZSM-5. Dies wird durch Desorptionenthalpien von 66 bis 74 kJ/mol unterstützt, die durch kalorimetrische Messungen ermittelt wurden. Die Na^+ -Spezies haben jedoch nur geringe Auswirkungen auf die Adsorption von Wasser und Methanol an Na-[Al]SBA-15. Desorptionenthalpien von 44-60 kJ/mol deuten auf eine Adsorption an weniger polaren Si(OH)-Gruppen hin. Es wird allgemein angenommen, dass die Brønsted-Säure-Zentren die Adsorption in H-formigen Materialien, z. B. in H-ZSM-5, dominieren. Aufgrund der geringen Menge und schwachen Stärke der Säurezentren von H-[Al]SBA-15 erfolgt die Wasser- und Methanoladsorption jedoch hauptsächlich an Si(OH)-Gruppen, wie im Fall von Na-[Al]SBA-15.

1. Zusammenfassung

Einfluss der definierten Geometrien der Poren und der Oberflächenzentren auf die Methanoladsorption

Im dritten Teil (Kapitel 8) wird erörtert, wie die definierten Geometrien der Poren und die Oberflächenzentren die Methanoladsorption beeinflussen. Die schrittweise Desorption von Methanol wird nach der Sättigung mikroporöser MFI-Zeolithe, mesoporöser SBA-15-Materialien und amorpher Silikate auf Siliziumwolframsäure-Trägern (STA) durchgeführt, alle in ihren isostrukturellen Siliziumdioxid-, Na- und H-Formen. Festkörper-NMR und DRIFTS werden eingesetzt, um die Oberflächenspezies zu identifizieren und ihre Mengen zu quantifizieren. In Sättigung sind auf allen Materialien flüssigkeitsähnliche Methanolspezies vorhanden. Die maximale Menge an Adsorbat in Sättigung wird in erster Linie von der zugänglichen Oberfläche bestimmt. Bei Silikaten dominiert die Adsorption an Si(OH)-Gruppen, insbesondere bei Materialien mit amorphen Porenwänden wie SBA-15. Für Methanol, das auf Silikalit adsorbiert wurde, wird jedoch kaum eine Oberflächenbeladung beobachtet. Dies ist auf die in Silikalit vorhandenen hydrophoben Mikroporen zurückzuführen. Methanol adsorbiert stark an Na⁺ und H⁺ in den Mikroporen von Na-ZSM-5 bzw. H-ZSM-5. Der starke Einschluss bewirkt eine hohe Stabilität der Methanol-Kationen-Komplexe, die auch bei höheren Temperaturen stabil sind. Nach der Desorption bei 423 K wurde die Bildung von Dimethylether (DME) durch ¹³C-MAS-NMR-Spektroskopie und DRIFTS bestimmt. Zum ersten Mal wurde das ¹H-MAS-NMR-Signal von verbrückenden Si(OH)Al-Gruppen, die durch DME gestört wurden, bei $\delta_{1H} = 14,4$ ppm beobachtet. In den Na- und H-Formen von SBA-15 und STA-Materialien sind die Methanol-Kationen-Komplexe in geringeren Mengen vorhanden und dissoziieren schnell aufgrund fehlender Stabilisierung durch einen Einschluss in Poren. Stattdessen binden Si(OH)-Gruppen das Methanol in den mesoporösen und nicht porösen Materialien stark. Unsere Beobachtungen weisen (1) darauf hin, dass der Einschluss in Mikroporen wichtig für die Bildung von Oberflächenkomplexen und damit entscheidend für die katalytische Umwandlung von Methanol und anderen Alkoholen ist; und (2), erklären warum häufig Nebenreaktionen auftreten, wenn Zeolithkatalysatoren reich an Si(OH)-Gruppen oder Defekten sind.

1. Zusammenfassung

Einfluss der definierten Geometrien der Poren und der Oberflächenzentren auf die Wasseradsorption

Im letzten Teil (Kapitel 9) verwenden wir identische Materialien und Methoden wie bei der Untersuchung der Methanoladsorption, um die Wasseradsorption in verschiedenen Porengeometrien und Hohlräumen und an verschiedenen Oberflächenzentren quantitativ zu untersuchen. Außerdem wird ein Vergleich der Adsorptionseigenschaften von Wasser und Methanol durchgeführt, um den Einfluss der Adsorbate selbst zu verdeutlichen. Bei der Sättigung hängt die anfängliche Maximalbeladung wieder hauptsächlich von der zugänglichen Oberfläche ab. SBA-15 übertrifft hier die anderen Materialien in Bezug auf die adsorbierten Wassermengen. Wie bei der Methanoladsorption bilden sich in allen Materialien flüssigkeitsähnliche Wasserspezies, wiederum mit Ausnahme von Silikalit. Dies ist durch die geringe Wechselwirkung der Wassermoleküle mit der Oberfläche der hydrophoben Mikroporen zurückzuführen. Bei der Desorption von Silikalit adsorbiert das Wasser an Si(OH)-Gruppen in Silanolnestern. In Na- und H-ZSM-5 bilden Wasser und Gegenionen in den Mikroporen stabile Komplexe. Bei den weniger eingeschränkten Materialien [Al]SBA-15 und STA@A200 sind die Komplexe dagegen nicht vorhanden oder zerfallen bereits bei niedrigen Temperaturen. Dies deutet darauf hin, dass der Einschluss in den Poren die Bildung von Oberflächenkomplexen mit Wasser unterstützt und diese stabilisiert, wie bereits bei Methanol beobachtet. Dann wurden die Adsorbatmengen von Wasser und Methanol verglichen. Auf ZSM-5 wechselwirkt Methanol stärker mit katalytisch aktiven BAS als Wasser. Dies erklärt, warum die BAS nicht durch Wasser blockiert werden können, welches zum Beispiel in stöchiometrischen Mengen bei der Umwandlung von Methanol als Nebenprodukt entsteht.

2. Abstract

Interactions between solid catalyst surface sites and reactants determine the catalytic performance. Therefore, understanding such interactions is crucial for rationally designing solid catalysts and optimizing the product distribution. In this dissertation, the following three sub-topics are discussed: (1) How to introduce aluminum in purely siliceous materials using sodium aluminate (NaAlO_2); (2) How to identify binding sites and measure binding energies of water compared with methanol adsorbed on micro- and mesoporous materials; (3) How to elucidate the influence of confinement on water and methanol adsorption.

The Alumination of Porous Silica with Sodium Aluminate

In the first part (chapter 6), the NaAlO_2 modification mechanism was studied on micro- and mesoporous materials (DeA-Y zeolite, SBA-15, and SBA-16). The produced ion exchangers and acid catalysts are investigated by various MAS NMR spectroscopic techniques. It is observed that the alkaline NaAlO_2 solution is able to partially dissolve the silica surface. This comes along with the formation of $\text{Si}(\text{OH})_x$ groups ($x = 1$ to 3). Some of these groups subsequently react with NaAlO_2 and generate the tetrahedral aluminum that is normally known as framework aluminum sites, except for SBA-16 that also forms extra-framework aluminum. The alumination performance, consisting of the quantity and coordination types of introduced aluminum, depends on the pore diameter and the pore structure of siliceous parent materials and the treatment temperature. This modification works best on the SBA-15 that has a hexagonal through-hole pore structure. Almost each introduced aluminum atom forms an ion exchangeable site. However, less than 20% of these sites can be finally transformed into Brønsted acid sites (BAS), because some tetrahedral aluminum converts to pentahedral and octahedral coordination upon calcination of NH_4 -forms into H-forms. The acid contents and properties were studied by loading probe molecules like ammonia, acetonitrile, and TMPO. It is found that the generated BAS on mesoporous materials are weak and only detectable by strong base molecules. This is due to the flexible coordination between $\text{Si}(\text{OH})$ groups and tetrahedral aluminum species. Strong BAS similar to those found in directly synthesized zeolite are formed on microporous DeA-Y zeolite. TMPO loading combined with ^{31}P MAS NMR spectroscopy indicates the presence of several distinct Brønsted and Lewis acid sites on H-form materials.

2. Abstract

Binding Sites and Strength of Water and Methanol Adsorption on Micro- and Mesoporous Materials

In the second part (chapter 7), the adsorption sites of water and methanol on siliceous and aluminum-containing microporous ZSM-5 zeolites and mesoporous SBA-15 materials were investigated by MAS NMR spectroscopy and TGA-DSC. For siliceous Silicalite and SBA-15, ^{29}Si CP MAS NMR studies reveal that silanol groups are the dominant adsorption sites for water and methanol. We observe a stronger interaction with Q^3 -type $\text{Si}(\text{OH})$ groups for methanol compared with water. The Q^2 -type $\text{Si}(\text{OH})$ group on SBA-15 enhances its hydrophilicity. ^{23}Na MAS NMR spectroscopy convinces the strong interaction of Na^+ cations with water or methanol molecules on Na-ZSM-5. This is supported by desorption enthalpies of 66 to 74 kJ/mol determined by the calorimetric measurements. However, the Na^+ species have little effect on water and methanol adsorption on Na-[Al]SBA-15. Desorption enthalpies of 44-60 kJ/mol indicate adsorption on less polar $\text{Si}(\text{OH})$ groups. The Brønsted acid sites are commonly believed to dominate adsorption in H-form materials, *e.g.* H-ZSM-5. However, due to the low quantity and weak strength on H-[Al]SBA-15, water and methanol adsorption mainly occurs on $\text{Si}(\text{OH})$ groups as in the case of Na-[Al]SBA-15.

Influence of Confinement and Surface Sites on Methanol Adsorption

In the third part (chapter 8) it is discussed how confinement and surface sites impact methanol adsorption. Stepwise desorption of methanol is performed after saturation of microporous MFI zeolites, mesoporous SBA-15 materials and amorphous silica supported silicotungstic acid (STA), all in their isostructural siliceous, Na-, and H-forms. MAS NMR and DRIFTS are applied to identify the surface species and quantify their amounts. In the saturation state, liquid-like methanol species are present on all materials. The saturation quantity is mainly controlled by surface areas. For siliceous materials, adsorption on $\text{Si}(\text{OH})$ groups is dominant, especially on materials with amorphous pore walls like SBA-15. However, a repulsive effect is observed for methanol loaded on Silicalite, due to the strong confinement in micropores. Methanol strongly adsorbs at Na^+ and H^+ in the micropores of Na-ZSM-5 and H-ZSM-5, respectively. The strong confinement causes a high stability of the methanol-cation complexes, which are stable at elevated temperatures. After desorption at 423 K, the formation of dimethyl ether (DME) was determined by ^{13}C MAS NMR spectroscopy and DRIFTS. For the first time, the ^1H MAS NMR signal of bridging $\text{Si}(\text{OH})\text{Al}$ groups disturbed by DME was observed at $\delta_{1\text{H}}$

2. Abstract

= 14.4 ppm. In Na- and H-forms of SBA-15 and STA materials, the methanol-cation complexes are in lower quantities present and dissociate fast due to the absence of sufficient confinement. Instead, Si(OH) groups bind methanol strongly in the mesoporous and non-porous materials. Our observations (1) indicate confinement of micropores is the key point for the formation of surface complexes, and therefore crucial for the catalytic conversion of methanol and other alcohols; (2) explain why side-reactions frequently occur if zeolite catalysts are rich in Si(OH) groups or defects.

Influence of Confinement and Surface Sites on Water Adsorption

In the last part (chapter 9), we use the same materials and methods as the investigation of methanol adsorption to quantitatively study the water adsorption under various confinements and on different surface sites. Furthermore, a comparison of the adsorption properties between water and methanol is performed to illustrate the influence on adsorbates themselves. In saturation, the initial loading mostly depends on the surface area and SBA-15 outperforms other materials in terms of the adsorbed water amounts. As during methanol adsorption, liquid-like water species are formed in all materials, again except for Silicalite. This is due to a strong repulsive effect in the siliceous micropores on water molecules. Upon desorption, nevertheless, water strongly binds at Si(OH) groups in silanol nests. In Na- and H-ZSM-5, water and counter ions form stable complexes in the micropores. Whereas the complexes are absent or break down fast on less confined [Al]SBA-15 and STA@A200 materials. This indicates that confinement is the core for the formation of surface complexes with water, like for methanol. More methanol is strongly retained in ZSM-5 materials, which explains why active sites are not blocked by water, the co-product omnipresent during the conversion of methanol conversions on zeolites.

3. The Aims of the Work

Porous materials usually contain ordered pore structures, sufficient pore volumes and large surface areas. These physical properties give them the potential to be applied in various areas, such as catalysis, adsorption, separation, energy storage, etc. It is worth noting that directly synthesized porous materials sometimes have their special disadvantages limiting their utilization scopes. Therefore, the post-modification of porous materials is necessary to improve the performance in a specific application or to expand their applications. For example, the directly synthesized Y zeolite usually has a low Si/Al ratio in a range of 1 to 4, leading to an outstanding acid density but also an instability of this material. To overcome this drawback, a dealumination treatment is performed to remove aluminum and increase the stability in fluid catalytic cracking (FCC). Conversely, mesoporous silica materials exhibit inert surface composed of SiO₂ and are rarely directly used as catalysts. The preparation of catalytically active mesoporous silica often requires various modification approaches to introduce active sites in mesopores. Alumination is commonly used to introduce Brønsted acid sites in mesoporous silica and diverse aluminum sources have been used for this purpose. Sodium aluminate is one of the most frequently used chemicals for the alumination process. However, the alumination mechanism, factors influencing alumination process, and acid properties of the aluminated materials are still unclear, which hinders a rational optimization of surface acid sites in porous, especially the mesoporous, silica materials.

In addition, the confinement effect plays a role in the physical and chemical properties of adsorbates that subsequently impact the catalytic reactions. Many confinement studies focus on how the topologies of zeolites influence chemical reactions, providing guidance for the design and optimization of catalysts. However, these researches are performed on materials with similar pore sizes and the same surface sites. A comprehensive investigation of confinement effects in micropores materials, mesoporous materials and non-porous materials with different surface sites is still missing. Therefore, the aims of the present work are in the following:

(1) The sodium-aluminate modification of porous silica is performed under different conditions, including temperature, the concentration of NaAlO₂, and pore size and pore structure of materials, to find out the impacts on this alumination process. The alumination mechanism is unveiled by different MAS NMR spectroscopy. And the acid properties are disclosed by loading probe molecules, like ammonia, acetonitrile, and TMPO, combining with

3. The Aims of the Work

^1H and ^{31}P MAS NMR measurements.

(2) Determining the binding sites and binding energies of water and methanol on micro- and mesoporous materials in their siliceous, Na- and H-forms are conducted by using MAS NMR spectroscopy and TGA-DSC measurement.

(3) The influence of confinements and surface sites in the adsorption process is studied using microporous, mesoporous and non-porous materials in their respective siliceous, Na- and H-forms. And the influence of the adsorbates themselves is studied by comparison of methanol and water under the same desorption procedure. Surface species are determined by ^1H MAS NMR and DRIFTS measurements. Based on these results, a comprehensive understanding of the factors influencing water and methanol adsorption on silica materials is gained. These investigations should be helpful in the synthesis and optimization of silica catalysts.

4. Introduction

4.1 Introduction of Silica Materials

4.1.1 Introduction of Porous Silica

Porous materials have attracted numerous scientific and industrial interest and are widely used in applications such as catalysis, ion exchange, and adsorption and separation. The porous solids naturally involve large pore volumes and surface areas, that enable an intense contact between surface and molecules. In addition, the size, volume and shape of the pore cavity can be important. It causes a confinement of molecules that differs between different pore structures, which changes the physical properties of molecules and thus influences chemical reactions happening with them. According to International Union of Pure and Applied Chemistry (IUPAC), porous materials are classified into microporous material with a pore size smaller than 2.0 nm, mesoporous material with a pore size in the range of 2 to 50 nm, and macroporous material with a pore size larger than 50 nm.^[1] In addition to the pore structures, the atoms on the porous solids directly relate with the surface properties and therefore influence the performance on a certain application. For example, when aluminum is introduced on the framework of siliceous zeolite, the surface polarity increases and the aluminated zeolite becomes an ion exchanger or acid catalysts.

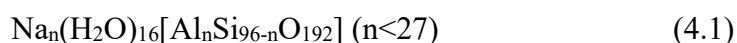
4.1.1.1 Introduction of Zeolite

Zeolites are crystalline silicates or aluminosilicates with ordered micropore structures. The zeolite framework is built by connections of so-called corner-sharing tetrahedra structures, TO_4 , where the “T” denotes the central atom, usually Si, tetrahedrally coordinated with four oxygen atoms. When the T sites are all silicon atoms or contain traces of other quadrivalent elements, *e.g.* tin, the whole zeolite is charge balance. However, when trivalent elements like aluminum or boron are induced into a zeolite, the generated negative charges must be compensated. This happens usually by extra-framework cations. In this condition, the zeolite becomes an ion exchanger or solid acid (when the cation is H^+). Although the fundamental unit is only the TO_4 , different connections of the TO_4 structure form various topologies of zeolite frameworks. Until now, more than 240 types of zeolites have been identified and recorded into the zeolite structure database of International Zeolite Association (IZA) with three-capital-letter codes.^[2] These zeolites can be classified, in accordance with their largest pore window, into small-pore (≤ 8 -membered (MB) ring), medium-pore (10-MB ring), large-pore (12-MB ring), and extra-large-pore (> 12 -MB ring) zeolites.^[3] Here, the item “n-MB ring” refers the

4. Introduction

number of T atoms (or O atoms) in a cycle of T and O atoms. Noteworthy, rings with the same number of atoms can have different effective widths. For example, the 12-MB rings in MOR, BEA and FAU type zeolites have free diameters of 0.65, 0.66 and 0.74 nm, respectively, which is explained by the different T-O-T angles in the rings. The small but different size of the pore windows combined with the different surface polarity make zeolites also very important to selectively separate molecular mixtures.^[4-7] That explains why zeolites are also called molecule sieves. In addition to the pore window, the size of the voids is also various in different zeolites and can be categorized to cages and cavities. A cage is a polyhedral void with narrow faces (< 6-MB ring), so that species larger than a water molecule cannot go inside, whereas a cavity is a void with at least a large face that the species larger than the size of a water molecule can go through.^[8] According to the literature, there are about 43 kinds of cavities among the known zeolites.^[9] These cavities, accompanied by different surface sites present on these materials, lead to different confinement effects and therefore their unique catalytic performance in a certain chemical reaction. For example, when a zeolite is synthesized with an organic structure-directing agents (OSDA) mimicking the transition state (TS), the formed cavities are able to stabilize the TS and endow outstanding reactivity and selectivity of this reaction.^[10]

MFI is one of the most important and widely used type of zeolites. The first MFI zeolite was synthesized by Robert J. Argauer and George R. Landolt in 1972 and named as Zeolite Scony Mobil-5 (ZSM-5).^[11] The chemical formula of MFI zeolites could be written as:



Here, the Na^+ counter ion can be replaced by other cations, such as H^+ , using traditional ion exchange method. The number of aluminum atoms in a MFI unit cell could vary over a wide range from 0 to 27. This allows MFI zeolites to be used in a variety of applications. For example, aluminum containing H-ZSM-5 zeolites are usually used as a solid acid catalyst, whereas the siliceous MFI zeolite, Silicalite, can be applied on, for example, water-oil separation.^{[12],[13]} As shown in figure 4.1, the MFI structure consists of two channels interconnected with each other.^{[14],[15]} Channels along the a-axis are sinusoidal channels with 10-membered-ring window and a pore size of 0.51×0.55 nm, while channels along the b-axis are straight channels with a 0.53×0.56 nm 10-membered-ring window. A typical MFI crystal has a hexagonal prismatic shape, that can be described as “coffin-like”. When an MFI zeolite is prepared with the usual OSDA, tetrapropylammonium (TPA), the crystal size on the three dimensions relate to each other as follows: $L_c > L_a > L_b$, whereby L_i denotes the length along the i-axis.^[15] A different

4. Introduction

OSDA, the trimer C6 TPA cation (tC6), can change the crystal shape into $L_c > L_b > L_a$.^[16] Considering the channel along b-axis is straight, indicating a preferred molecular diffusion property, researchers frequently try to decrease the thickness of the crystals along the b-axis.^{[17],[18]}

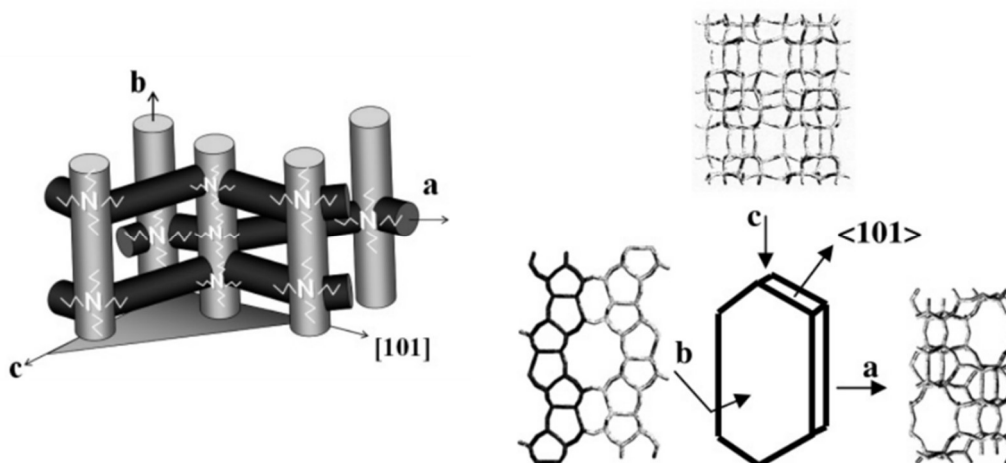


Figure 4.1 The schematic intersection of channels in MFI zeolites (left). The MFI zeolite framework along a-, b-, and c-axis (right).^[15]

4.1.1.2 Introduction of Mesoporous Silica

Compared to zeolites, the mesoporous silica materials have frequently larger pore sizes and surface areas, which lead to outstanding mass transport property and allow a high quantity of active sites, respectively. The uniform and adjustable mesopores and their large functionable surfaces make them useful in areas of adsorption and separation, catalysis, energy conversion and storage, medicine, and so on.^[19-25] Especially, the ordered mesoporous channels facilitate the applications involving large molecules, such as biomass conversion, drug delivery and so on.^{[21],[26],[27]}

In 1992, Beck et al. first reported the synthesis of a family of mesoporous silica known as M41S with tunable pore diameter from 1.5 to 10 nm.^{[28],[29]} The M41S materials includes the hexagonal form of MCM-41, the cubic form of MCM-48 and the lamellar form of MCM-50. Each of them is synthesized using alkyl quaternary ammonium cationic surfactants as template agent, *e.g.* cetyltrimethyl ammonium bromide, and runs mechanistically via a self-assemble of liquid crystals.^[30] Another famous series of mesoporous silicas are SBA (Santa Barbara acids) materials. Stucky et al. synthesized them by using commercial bi- and triblock copolymers as templates to form the order mesopores.^[31-33] The most famous SBA material is

4. Introduction

SBA-15, which has the same hexagonal structure as MCM-41 (figure 4.2). However, SBA-15 has a larger variation of pore size (4.6-30 nm) and thicker pore walls (3-9 nm) than MCM-41 after removal templates. These helps SBA-15 to overcome the disadvantages of poor hydrothermal stability and expensive template agent of MCM-41, providing a wider scope for modifications and applications.

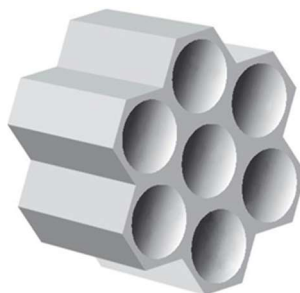


Figure 4.2 The hexagonal structure of mesoporous MCM-41 and SBA-15.

In contrast to zeolites, mesoporous silica normally only consists of amorphous SiO_2 , which is inert in most chemical reactions. Therefore, in order to sufficiently utilize the large pores and surface areas of mesoporous materials, it is necessary to modify the silica surface and introduce active sites on the surface or/and inside the mesopores. Taguchi and Schüth schematically summarized the possible methods in the functionalization of mesoporous materials (figure 4.3).^[34] In brief, the active sites can be introduced by direct synthesis or by post modification, such as substitution of Si by other elements like Al, Fe, etc., surface coating, immobilization of molecular catalyst or enzyme, preparing organic-inorganic hybrid framework, and so on.^[35-42] Among the different modification strategies, introducing heteroatoms in the mesoporous framework, and thereby introducing the acid sites or oxidation centers, is a simple but important way to extend the catalytic and adsorption and separation properties. However, it must be noted that, due to mesoporous silica is an amorphous material, the heteroatom substitution could lead to different sites with different local environments instead of the uniform and well defined sites as in crystalline zeolites.

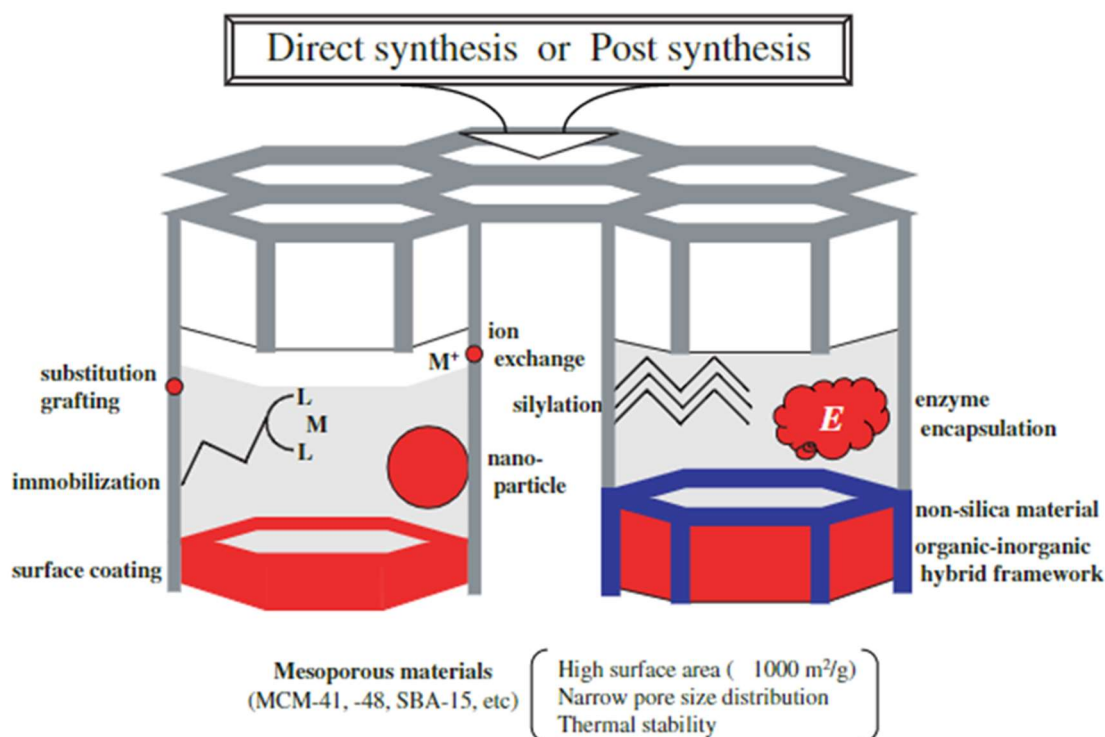


Figure 4.3 Methods for the functionalization of mesoporous material.^[34]

Directly hydrothermal synthesis is a common method for introducing heteroatoms and is conducted by adding the respective precursor during the formation and crystallization of the mesoporous pore walls. The heteroatoms are in situ generated by hydrolysis of the precursor in the reaction mixture and then built into the amorphous silicon structure. When the introduced ions are trivalent ions, such as B^{3+} , Al^{3+} , Fe^{3+} , etc., acid sites arise in the silica materials. While, when substitution of silicon atoms with heteroatoms, such as Mo^{4+} and V^{5+} , redox centers are created. Direct synthesis of [Al]SBA-15 has been successfully achieved using different aluminium and silicon sources. Yue et al. synthesized [Al]SBA-15 with a minimum Si/Al ratio of 10, using aluminum tri-*tert*-butoxide and tetraethyl orthosilicate (TEOS).^[43] In 2004, a two-step pH-adjusting method was reported in the preparation of [Al]SBA-15, and the Si/Al ratio can reach to 5.^[44] Li et al. creatively used a single source molecular precursor of di-*sec*-butoxyaluminumoxytriethoxysilane to directly synthesize the aluminum containing SBA-15, which introduced a large amount of aluminum and lead to Si/Al ratios in a range of 1 to 10.^[45] However, the direct synthesis strategy has certain disadvantages. The hydrolysis of metal precursors and silicon source should be matched with each other, otherwise it forms metal oxide and silicon oxide separately. Moreover, considering the thick pore wall of SBA-15, a lot aluminum in [Al]SBA-15 is then located inside the walls, which prevents it from participating

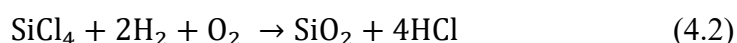
4. Introduction

in reactions that happen at the surface of these materials. Large particles of the heteroatom might also be deposited as amorphous structures inside pores or on its surfaces. In other words, the built-in efficiency and quality of generated sites is usually not high if a direct synthesis is performed.

Post modification means grafting heteroatoms onto the surface selectively, after the mesoporous silica was completely synthesized and potential templates were removed. Typically, metal chlorides, metal alkoxides, organometallic compounds, or metal complexes react with the silanol, Si(OH), groups on the mesoporous surface, anchoring the metals by forming M-O bonds. Several strategies for post alumination have been proposed. Luan et al. used sodium aluminate solution to produce ion-exchangeable Na-[Al]SBA-15.^[37] Also, it was shown that trimethylaluminum is able to react with Si(OH) groups and form BAS under dry conditions.^[46] Zhai et al. modified different mesoporous materials with aluminum isopropoxide.^[47] Lang et al. aluminated SBA-15 with AlCl₃ causing a Si/Al ratio of 10 after calcination at 723 K.^[48] But also the post alumination has its limitations. First, most post modification methods are performed under water and oxygen free conditions, which is hard to scale up. Second, the incorporation of heteroatoms depends on the diffusion of the aluminum source inside the pores. A slow diffusion can lead to a non-uniform distribution of active sites and sometimes even block the channels. Application of too much heat might furthermore causing a collapse of the amorphous mesopore frameworks and pores.

4.1.2 Introduction of Non-porous Silica

Compared to the porous silica, non-porous silica materials are lack of a molecular confinement leading to the best mass transfer properties. In 1940s, Kloepper developed a flame-pyrolysis method for preparing the fumed-silica materials that are named as Aerosil. This process is performed at a very high temperature (1500-1700 K), followed by a rapid quenching step.^[49] The whole process can be explained by the equation 4.2^[50]:



Here, H₂ and O₂ are in situ produced by the decomposition of water molecules. During this process, SiCl₄ is evaporated and hydrolyzed to form Si(OH)₄. Then Si(OH)₄ polymerizes into SiO₂ that grow into nanoparticles (NP). However, the size of the particle is various ranging from 5 to 50 nm.^[51] In 1968, Stöber et al. first prepared the size controlled non-porous silica

4. Introduction

with uniform diameters in a range of 50 to 2 μm .^[52] In their work alkoxy silane is hydrolyzed and condensed in an water-alcohol solution with the presence of ammonia as a catalyst. The net reaction equation can be written as equation 4.3:



Subsequently, Yokoi et al. developed the Stöber method by replacing the basic catalyst from ammonia to lysine or arginine and produced small silica NP with diameters of 4-12 nm.^[53] Furthermore, reverse water-oil microemulsions have been used in the synthesis silica NP. In this method, the hydrolysis and condensation of silicon alkoxides are performed inside the micropores of microemulsion.^{[54],[55]}

Like the mesoporous silica, introducing heteroatoms and actives on non-porous silica materials are usually necessary to improve the performance on applications like catalysis and medicine. For example, surface charge of silica NP can be controlled by using additions of 3-aminopropyltriethoxysilane or carboxyethylsilanetriol or zwitterion silanes.^[56-58] Furthermore, the active sites can be loaded on the amorphous silica surface by using wet impregnation, incipient-wetness impregnation, deposition–precipitation, etc.^[59-61]

4.2 Introduction of Solid-state NMR Spectroscopy

4.2.1 Principles of Solid-state NMR Spectroscopy

Solid-state NMR (SSNMR) is a non-invasive technique observing the change of nuclear shielding and offering thereby information about the coordination of atoms. The technique is herein used to investigate how physical adsorption and chemical reactions occur on solid materials. The common fundamentals of nuclear magnetic resonance (NMR) spectroscopy are described in previous literature.^[62] SSNMR can be used to any nucleus with nuclear spin, such as the herein relevant nuclei ^1H , ^{13}C , ^{27}Al , ^{29}Si , and ^{31}P . Since all these nuclei, except ^{27}Al , have a nuclear spin of $I = 1/2$, they are appropriate isotopes for the study of reactants and adsorbate complexes relevant in heterogeneous catalysis. A good accessibility of nuclei is crucial, because compared to liquid-state NMR the signals in SSNMR are strongly broadened due to anisotropic magnetic interactions. As a result, a high resolution of SSNMR spectra requires advanced experimental approaches to average all existing solid-state interactions.

The line broadening effect of SSNMR, which are described by the Hamiltonian (\hat{H}),

4. Introduction

result from the dominating interactions of the respective nuclear spin I .

$$\hat{H} = \hat{H}_{II} + \hat{H}_{IS} + \hat{H}_{CSA} + \hat{H}_Q \quad (4.4)$$

Here, \hat{H}_{II} and \hat{H}_{IS} represent the Hamiltonians of homonuclear and heteronuclear magnetic dipole-dipole interactions, respectively. \hat{H}_{CSA} , denotes the anisotropic chemical shift interactions. And \hat{H}_Q indicates quadrupole interactions. Detailed expressions for these Hamiltonians can be found in the literature.^[63] We note that for the nuclei with nuclear spins of $I = 1/2$, such as the ^1H , ^{13}C and ^{31}P nuclei, being not involved in an electric quadrupole interaction, only the first three terms are required.

The strongest relevant interaction for the $I = 1/2$ nuclei is usually of dipole-dipole character. The Hamiltonian \hat{H}_{II} for homonuclear interactions describes the dipolar coupling between the nuclei i and j with same nuclear spins I :

$$\hat{H}_{II \text{ homo}} = 1/2 \gamma^2 \hbar^2 r_{ij}^{-3} (\hat{I}_i \hat{I}_j - 3 \hat{I}_{iz} \hat{I}_{jz}) (3 \cos^2 \theta_{ij} - 1) \quad (4.5)$$

where γ presents nuclear gyromagnetic ratio of interacting nuclei i and j , r_{ij} denotes the internuclear distance, and θ_{ij} is the angle between r_{ij} and the external magnetic field B_0 (figure 4.4).

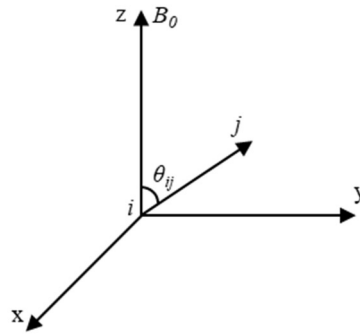


Figure 4.4 Sketch of internuclear vector r_{ij} (B_0 is parallel to z-axis).

In the case of dipole interactions between nuclei with different nuclear spins I and S (heteronuclear dipole interactions), the Hamiltonian $\hat{H}_{IS \text{ hetero}}$ is given by the following equation:

$$\hat{H}_{IS \text{ hetero}} = \frac{1}{2} \gamma_I \gamma_S \hbar^2 r_{IS}^{-3} \hat{I}_{Iz} \hat{I}_{Sz} (1 - 3 \cos^2 \theta_{IS}) \quad (4.6)$$

where γ_I and γ_S represent nuclear magnetogyric ratios of nuclei I and S , r_{IS} denotes the

4. Introduction

internuclear distance, and θ_{IS} is the angle between r_{IS} and the external magnetic field B_0 . The strong dependence of dipole interactions on the internuclear distance r_{ij} makes this type of interaction interesting for the studying of the local structure in the vicinity of the resonating nuclei and enables the determination of distances.

Chemical shift anisotropy (CSA) is another factor on NMR line broadening relevant for solid samples. In the principal axis system (PAS), the Hamiltonian of the chemical shielding interaction is given by^[63]:

$$\hat{H}_{\text{CSA}} = \gamma \cdot \hbar \cdot I \cdot \sigma_{\alpha\beta} \cdot B_0 \quad (4.7)$$

Where the shielding tensor σ can be reduced to its diagonal elements σ_{xx} , σ_{yy} , and σ_{zz} with^[63]:

$$|\sigma_{zz}| \geq |\sigma_{yy}| \geq |\sigma_{xx}| \quad (4.8)$$

The shift of the resonance frequency in the magnetic field B_0 is due to the σ_{zz} component in the laboratory frame (LAB). A rotational transformation with the Euler angles α and β leads to:

$$\sigma'_{zz} = \sigma_{xx} \sin^2 \beta \cos^2 \alpha + \sigma_{yy} \sin^2 \beta \sin^2 \alpha + \sigma_{zz} \cos^2 \beta \quad (4.9)$$

To simplify the equation 4.7, the isotropic part σ_{iso} , the shielding anisotropy $\Delta\sigma$ and the asymmetry parameter η are respectively introduced the by following equations:

$$\sigma_{iso} = \frac{1}{3} (\sigma_{xx} + \sigma_{yy} + \sigma_{zz}) \quad (4.10)$$

$$\Delta\sigma = \sigma_{zz} - \sigma_{iso} \quad (4.11)$$

$$\eta = \frac{\sigma_{yy} - \sigma_{xx}}{\Delta\sigma} \quad (4.12)$$

Transformation of the Hamiltonian into the LAB leads to:

$$\hat{H}_{\text{CSA}} = \gamma \cdot \hbar \cdot I_Z \cdot B_0 \left[\sigma_{iso} + \Delta\sigma \left[\left(\frac{3\cos^2\beta - 1}{2} + \frac{\eta}{2} \sin^2\beta \cos 2\alpha \right) \right] \right] \quad (4.13)$$

corresponding to a resonance frequency ω of:

$$\omega = \omega_0 \left[(1 - \sigma_{iso}) - \Delta\sigma \left(\frac{3\cos^2\beta - 1}{2} + \frac{\eta}{2} \sin^2\beta \cos 2\alpha \right) \right] \quad (4.14)$$

4.2.2 Magic-Angle Spinning Technique

Magic angle spinning (MAS) is a procedure that significantly reduces signal broadening coming from the previously described anisotropic magnetic interactions. In this procedure, the rotation (ω_{rot}) of the solid powder sample is performed along the axis that is at an angle of $54^\circ 44'$ to the direction of the external magnetic field B_0 (figure 4.5). It can be seen that rapid rotation around this macroscopic axis produces high-resolution of SSNMR spectra comparable to those of liquids.

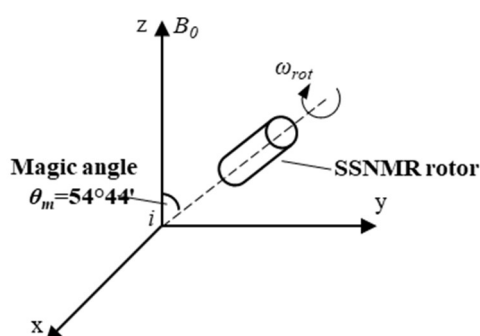


Figure 4.5 Sketch of magic angle spinning.

When $\theta = \theta_m = 54^\circ 44'$, the geometric terms on the right side of equations (4.5) and (4.6) become zero.

In the case of quadrupole interactions, the term $(3\cos^2\theta - 1)$ exists only in the first-order frequency distribution function.^[64] Since the time average of $(3\cos^2\theta - 1)$ is zero under fast magic angle spinning, the first-order quadrupolar interaction can be eliminated under these conditions. In contrast, the geometric term of the second-order quadrupolar interaction is reduced by only factor of 0.3 under magic angle rotation.^[64] Thus, the quadrupolar interaction cannot be completely averaged out via MAS and further techniques are used to increase the signal-noise ratio of such nuclei.

4.2.3 Cross-polarization Technique

Cross-polarization (CP) is a typical dual-resonance technique that can be applied to improve the sensitivity of rare isotopes such as ^{13}C and ^{29}Si nuclei by making use of a better accessible, more abundant nucleus in proximity.^[65] The principle of this technique is shown in

figure 4.6.

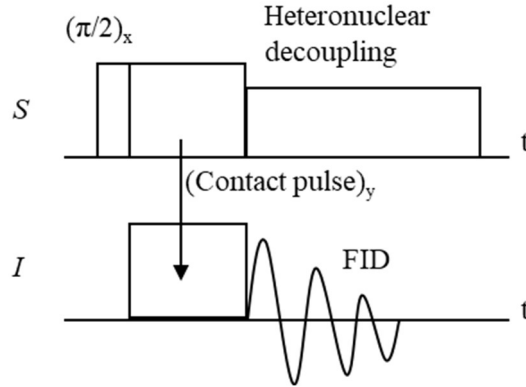


Figure 4.6 Pulse program of cross polarization measurement.

The experiment starts with a $\pi/2$ -pulse applied to the S -spins (for example ^1H). Upon the following contact pulse, the spin polarization shifts from the abundant S -spins to the investigated I -spins (e.g. ^{13}C nuclei) under the permission that the Hartman-Hahn matching conditions are satisfied^[64]:

$$\alpha_S \cdot \gamma_S \cdot B_{1S} = \alpha_I \cdot \gamma_{S1} \cdot B_{1I} \quad (4.15)$$

Briefly, the radio frequency (rf) pulse applied to the S -spins selectively induces transitions between the levels with the magnetic spin quantum numbers m and $m-1$. The parameters α_S and α_I are equal to 1 for $I = S = 1/2$. B_{1I} and B_{1S} denote the magnetic field amplitudes of the rf pulses applied to the I -spins and S -spins, respectively. After the contact period, the I -spins exhibit the free induction decay (FID) for the I -spins. The intensity $I_{CP}(\tau_{CP})$ of the corresponding signal is then as follows:

$$I_{CP}(\tau_{CP}) \propto \left(1 - \frac{\tau_{CP}}{T_{1\rho}}\right)^{-1} \left(\exp\left\{-\frac{\tau_{CP}}{T_{1\rho}}\right\} - \exp\left\{-\frac{\tau_{CP}}{T_{CP}}\right\}\right) \quad (4.16)$$

$T_{1\rho}$ is the time constant of the S -spin magnetization decay under the spin locking circumstance. The efficiency of cross-polarization depends on various factors influencing the intensity of the heteronuclear dipole interaction between the S -spins and I -spins, such as number and proximity of nuclei, their gyromagnetic ratios and their thermal movement. Thus the so-called CP time constant, T_{CP} , is inversely proportional to M_2^{IS} . Furthermore, it should be noted that the highest values of $I_{CP}(\tau_{CP})$ is obtained from rigid lattices. And if the nuclei show rapid thermal motions, the that $I_{CP}(\tau_{CP})$ will at some point even disappear.^[66] Heteronuclear

dipolar interactions can be suppressed by high-power decoupling (HPDEC) of the S-spins during the acquisition of the *I*-spin FID.

4.3 Introduction of DRIFTS

The infrared (IR) spectroscopy deals with the interaction of infrared radiation with matter. The IR portion is usually divided into three regions of the near-, mid-, and far-IR with wavenumbers around 14000-4000 cm⁻¹, 4000-400 cm⁻¹, and 400-20cm⁻¹ respectively. Among them, the mid-IR spectroscopy is the most widely used method because its wavenumbers correspond to the fundamental vibrations of chemical bonds. Fourier transform IR (FT-IR) spectroscopy was developed in the 1950s, based on the mathematical Fourier transform of an interferogram. The traditional transmission-absorption FT-IR has the advantages of fast analysis speed, high resolution, high sensitivity and high accuracy.^[67] However, a pressed self-supporting sample must be prepared for FT-IR, which is not applicable for the in situ measurements.^[68] Diffuse reflectance infrared Fourier transform spectroscopy (DRIFTS) collects and analyzes not only the reflected component but also the diffuse scattered component that comes from the transmission, refraction and reflection inside the sample (figure 4.7). Compared to FT-IR, the effortless sample preparation in DRIFTS preserves the original structure of powder materials, which is beneficial to the in situ measurements. It is noteworthy that the absorbance is not proportional to the sample concentration in DRIFTS due to the presence of both reflected and diffuse IR radiation. To solve this problem, Kubelka-Munk theory is applied here. Considering the DRIFTS sample is normally infinitely thick (several millimeters for mid-IR region) where increasing of the thickness does not change IR band intensities, a simplified Kubelka-Munk function (equation 4.16) of the relationship between R_{∞} is given^[68]:

$$F(R_{\infty}) = \frac{(1-R_{\infty})^2}{2R_{\infty}} = \frac{k}{s} \quad (4.17)$$

Here, $F(R_{\infty})$ is known as the Kubelka-Munk function. R_{∞} is the diffuse reflectance calculated from the ratio of the single-beam spectrum of the sample against that of the reference (*e.g.* KBr). k and s denote the absorption coefficient and the scattering coefficient, respectively. In this way, a relationship between R_{∞} and k is formed. Therefore, the change of band intensity enables to quantify the change of the concentration of a matter.

4. Introduction

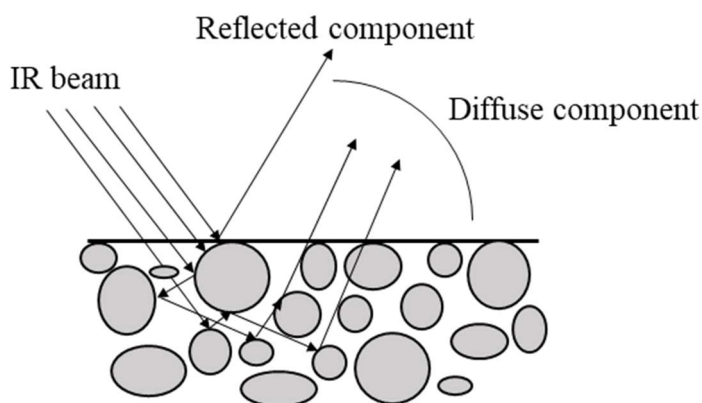


Figure 4.7 Sketch of IR path the diffuse measurement

Both SSNMR and DRIFTS are widely used in investigation of solid catalysts. SSNMR is able to observe multiple nuclei in the same sample and provides information about the solid structure. However, SSNMR measurement is slow, which can only detect the processes within the time scale of μs to ms (figure 4.8) and give an averaged signal of the whole material. In contrast, IR spectroscopy is fast and enables to observe the events in 10^{-13} to 10^{-15} s. This makes IR yield results of single molecule.^[67] Therefore, the combination of SSNMR and DRIFTS is essential to acquire a comprehensive knowledge of solid materials. In addition, correlations between SSNMR and IR results have been established. For example, for the hydroxyl groups, the chemical shift in ^1H MAS NMR is linear correlated with the wavenumber in IR^[69]:

$$\delta_H(\text{ppm}) = 57.1 - 0.0147\nu_{OH}(\text{cm}^{-1}) \quad (4.18)$$

When the protons are in hydrogen bonding, the equation 4.17 can be corrected by:

$$\delta_H(\text{ppm}) = 37.9 - 0.0092\nu_{OH}(\text{cm}^{-1}) \quad (4.19)$$

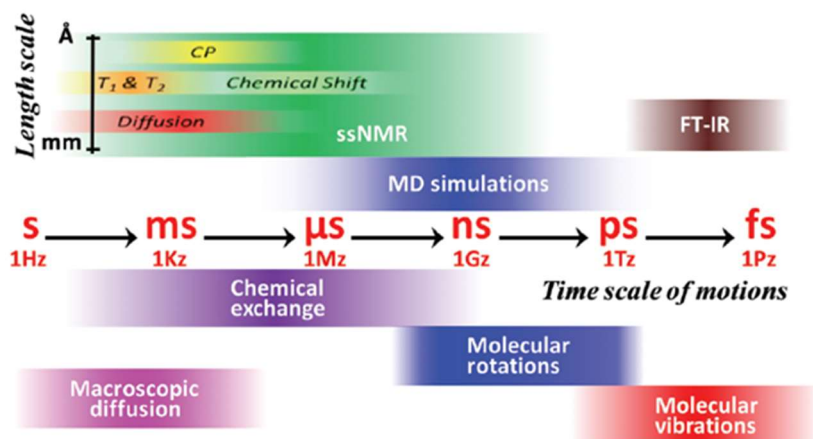


Figure 4.8 Time scale of different experimental methods.^[67]

4.4 Introduction of TGA-DSC

Thermogravimetric analysis (TGA) is a typical thermal analysis method determining the change of mass. While differential scanning calorimetry (DSC) measures the difference of the required heats between a sample and reference. When these two methods are combined, the change of mass and heat are simultaneously collected, which gives meaningful hints about what happens during a thermal treatment. An example is shown in figure 4.9.^[70] There are two clear signals in the DSC curve indicating two endothermic processes happen at 92 and 230 °C, whereas only a strong drop of sample mass appears at 230 °C. This reveals the melting and boiling temperature of naphthalene are at 92 and 230 °C, respectively. In addition, the heats of phase transition can be calculated when the mass of naphthalene is known. It must be noted that, the limiting temperature of TGA-DSC measurements depends on the lowest limiting temperature of the furnace, the carrier and the crucible. In addition, DSC measurement must be performed under a stable condition, *i.e.* a heating or cooling step with a constant ramp. That means the experimenter should expect a temperature, where physical or chemical reaction happens, and give enough space for reaching a stable heating or cooling rate.

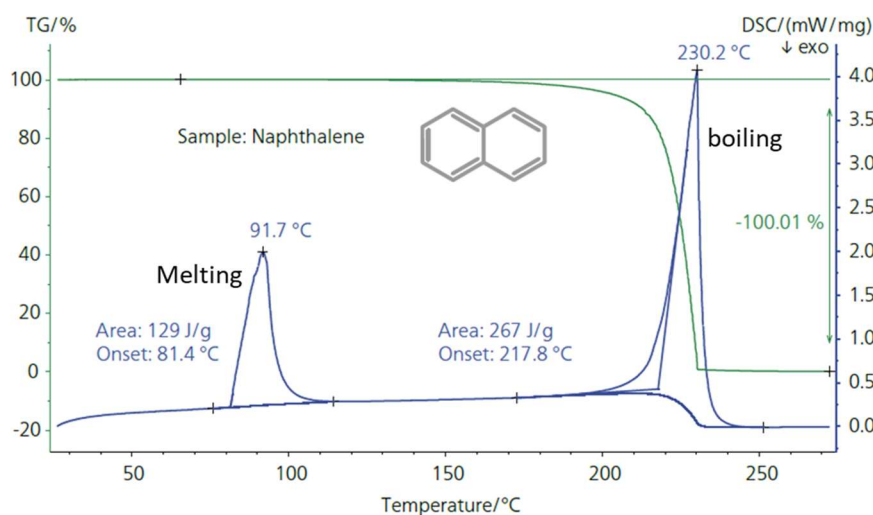


Figure 4.9 Melting and boiling point determination for Naphthalene. The green line indicates the change of sample mass and the blue line indicates the DSC curve.^[70]

5. Experimental

5.1 Materials Preparation

Table 5.1 Chemicals used in this study

Name	Chemical formula	Supplier	Purity
1-Butanol	CH ₃ (CH ₂) ₃ OH	Janssen Chimica	99.5%
Acetonitrile-d ₃	CD ₃ CN	Sigma-Aldrich	99.96 atom% D
Aerosil® 200	-	Evonik	-
Ammonia	NH ₃	Westfalen Gas	99.98%
Ammonium hydroxide	NH ₄ OH	Sigma-Aldrich	20 wt.% in H ₂ O
Ammonium nitrate	NH ₄ NO ₃	Merck	98.5%
DeA-Y	-	Degussa	-
Hydrochloric acid (37%)	HCl	Sigma-Aldrich	99%
H-ZSM-5	-	Tricat Inc.	-
Levasil 200N	-	Bayer	-
Methanol	CH ₃ OH	Scharr	99.8%
Methanol-d ₃	CD ₃ OH	Sigma-Aldrich	99.8 atom% D
Methanol- ¹³ C	¹³ CH ₃ OH	Sigma-Aldrich	99 atom% ¹³ C
Pluronic® F127	EO ₁₀₆ PO ₇₀ EO ₁₀₆	Sigma-Aldrich	-
Pluronic® P123	EO ₂₀ PO ₇₀ EO ₂₀	Sigma-Aldrich	-
Potassium nitrate	KNO ₃	Sigma-Aldrich	99%
Silicotungstic acid	H ₄ W ₁₂ SiO ₄₀	Sigma-Aldrich	p.a.
Sodium aluminate	NaAlO ₂	Sigma-Aldrich	Al (Al ₂ O ₃): 50-56%, Na (Na ₂ O): 37-45%
Sodium hydroxide	NaOH	Merck	>99%
Sodium nitrate	NaNO ₃	Merck	>99%
Tetraethyl orthosilicate	(C ₂ H ₅ O) ₄ Si	Sigma-Aldrich	>99%
Tetrapropylammonium bromide	(CH ₃ CH ₂ CH ₂) ₄ N(Br)	Fluka	>98%
Trimethylphosphine oxide	(C ₂ H ₅) ₃ PO	Alfa Aesar	>99%

5. Experimental

5.1.1 Synthesis of Silicalite

Levasil 200N sol was added into a solution containing ammonium hydroxide and tetrapropylammonium bromide (TPABr) in a ratio of 8TPABr-60NH₃-90SiO₂-750H₂O. The material was subsequently crystallized in a rotating steel autoclave with Teflon insert at 453 K for 48 h. The resulting material was then filtered, washed with deionized water, and calcined in a muffle furnace at 823 K for 6 h with a heating ramp of 1 K/min in air.^{[71],[72]}

5.1.2 Synthesis of SBA-15

A HCl solution was prepared with 130 mL H₂O and 20 mL of 37% concentrated HCl solution. It was used to dissolve 4 g of Pluronic[®] P123. After complete dissolution, 9.14 mL of tetraethyl orthosilicate (TEOS) was added to the mixture, stirred at 318 K for 7.5 h, and aged at 353 K for 15.5 h in a steel autoclave with Teflon insert. The resulting material was filtered, washed with deionized water, and then calcined in a muffle furnace at 823 K for 6 h with a heating ramp of 1 K/min in air.^[73]

5.1.3 Synthesis of SBA-16

2.5 g of Pluronic[®] F127 was dissolved in a solution containing 120 mL of H₂O, 4.5 mL of 37% concentrated HCl and 9.25 mL of 1-butanol. Then 13 mL of TEOS was added and stirred at 318 K for 24 h. The mixture was transferred into a steel autoclave with Teflon insert and aged for 24 h at 373 K. Afterwards, the gel was filtered, washed with deionized water and calcined in a muffle furnace at 823 K for 6 h with a heating ramp of 1 K/min in air.^[73]

5.1.4 Preparation of Silica Supported Silicotungstic Acid

Aerosil[®] 200 was pressed at a pressure of 150 kN for 1 h using a Weber PW20 Press with Model 8 vacuum press tool (compact diameter = 4.0 cm). Prior to using, this pressed material was ground and sieved into a particle range of 200-315 μm and named A200. Incipient wetness impregnation was carried out for a twofold loading of silicotungstic acid (STA) on A200. Thereby, each time, while stirring with a spatula, a solution of 0.4 g of STA in 0.7 mL of H₂O was dripped to 1 g of A200 via a cannula. The following drying step was performed at 393 K for 16 h and the sample is named H-STA@A200.^[60]

5. Experimental

5.1.5 Alumination of Silica Materials

For improving the alumination procedure during this work, the synthesis conditions were screened systematically. Thus, the amount of alumination agent and the alumination temperature were modified. Typically, 2 g of siliceous porous material, *e.g.* SBA-15, was put in 200 mL of sodium aluminate (NaAlO_2) solution and stirred for 16 h (detailed content and temperatures shown in table 5.2). The as-synthesized aluminosilicate was filtered, washed with deionized water, and calcined at 823 K for 6 h to get the Na-form of the respective aluminated materials. For directly addressing the respective alumination conditions, the following nomenclature was implemented: materials aluminated in Condition 1 were named with the suffix “-low”, in Condition 2 materials were named with the suffix “-high”, and in Condition 3 they were named with a suffix “-ht”.

Table 5.2 Alternative alumination conditions and the suffixes used in naming the synthesized materials

	m_{NaAlO_2} [g]	T [K]	suffix
Condition 1	0.12	298	-low
Condition 2	0.24	298	-high
Condition 3	0.24	333	-ht

5.1.6 Ion Exchange Method

5.1.6.1 Ion exchange of porous materials

The ion exchange of porous materials (zeolites and aluminated silica material) was conducted by adding 1.4 g material into 50 mL of 1 M nitrate solution and stirring at 353 K for 4 h for two times. For example, to get H-form material, 1.4 g of Na-form material was added to the NH_4NO_3 solution, while for acquiring Na-ZSM-5, commercial H-ZSM-5 was dispersed in a NaNO_3 solution. The resulting materials were filtered, washed nitrate free with deionized water and then calcined for 6 h at 823 K for microporous materials or at 673 K mesoporous materials in a muffle furnace.

5.1.6.2 Ion Exchange of Silica Supported Silicotungstic Acid

Due to the high solubility of STA, ion exchange of H-STA@A200 into the corresponding Na-form material, Na-STA@A200, in solution was not possible. Thus, the ion exchange was performed using an incipient wetness impregnation procedure, comparable to the procedure of

5. Experimental

STA loading on silica (section 5.1.4). Before ion exchange, chemical composition of H-STA@A200, especially the content of tungsten, was determined by ICP-OES. From stoichiometric considerations, it was assumed that the content of acidic H^+ was 4 times the content of tungsten atom. A 0.25 M NaOH solution containing stoichiometric Na^+ was dripped to the H-STA@A200 via a cannula accompanied by stirring with a spatula. The resulting sample was dried at 393 K for 16 h.

5.1.7 Sample Activation

The material was filled into a 4 mm glass tube for about 2-3 cm and then some glass wool was put on the top of the material to prevent pumping material into the vacuum line. The glass tube was connected to the vacuum line via a Quickfit, and heated with a 2-step temperature program. Usually for silica and aluminosilica materials it was firstly heated to 393 K in 2 h and kept for 2 h, and afterwards heated to 723 K in 3 h and kept for 12 h at a pressure below 10^{-2} mbar. However, for STA loaded materials the target temperature of the second heating step was set to 483 K in order to prevent decomposition of the Keggin units at elevated temperature. After cooling down, the material was sealed into the glass tube using a torch.

5.1.8 Summary of Porous and Non-porous Materials

By purchasing commercial materials and by applying the above-mentioned synthesis methods, finally five kinds of silica as well as their respective isostructural Na-, and H-form materials were received. Their names are listed comprehensively in table 5.3 to present an overview of solid materials investigated in this study. Again, as previously mentioned in 5.1.5, the suffixes “-low”, “-high” and “-ht” point to the different aluminations conditions that were applied. STA@A200 materials were prepared with incipient wetness impregnation (see 5.1.4 and 5.1.6.2). H-ZSM-5 is a commercial catalyst and its Na-form is obtained by ion exchange (see 5.1.6.1).

5. Experimental

Table 5.3 Porous and non-porous materials discussed in this study

Siliceous form	Na-form	H-form
A200	Na-STA@A200	H-STA@A200
DeA-Y	Na-DeA-Y-ht	H-DeA-Y-ht
SBA-15	Na-SBA-15-low	H-SBA-15-low
	Na-SBA-15-high	H-SBA-15-high
	Na-SBA-15-ht	H-SBA-15-ht
SBA-16	Na-SBA-16-low	H-SBA-16-low
	Na-SBA-16-high	H-SBA-16-high
SBA-16	Na-SBA-16-ht	H-SBA-16-ht
	Na-SBA-16-ht	H-SBA-16-ht
Silicalite	Na-ZSM-5	H-ZSM-5

5.2 Characterization Method

5.2.1 Saturation and Desorption of Water and Methanol

5.2.1.1 Water Saturation

The water saturation of the different materials was performed by adsorbing water molecules from saturated air. As shown in figure 5.1, therefore activated material was put into an opened vial and placed in a desiccator containing some saturated CaNO_3 solution in the bottom for at least 24 h. Then, the hydrated sample was transferred into a MAS NMR rotor, an aluminum crucible, or the in-situ DRIFTS chamber for the following MAS NMR, TGA-DSC, or DRIFTS measurement, respectively.

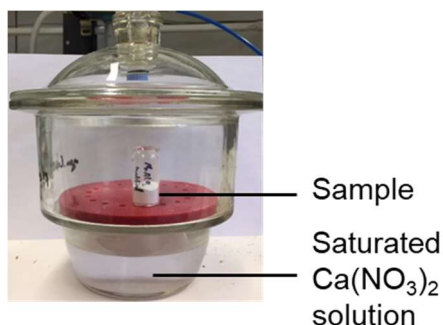


Figure 5.1 Water saturation procedure.

5. Experimental

5.2.1.2 Methanol Saturation

Similar like water saturation, methanol saturation was also performed via adsorption from the saturated gas phase. A glass tube containing pure liquid methanol lay in a nitrogen glove box and the activated sample was put in the left end of the glass tube (see figure 5.2). The valve was opened during loading process. After loading for at least 24 h, valve was closed and methanol loaded sample was fast transferred into a MAS NMR rotor or an aluminum crucible or the in-situ DRIFTS chamber for the following measurement. It was noted that, for the ^1H MAS NMR measurements, usually deuterated methanol (CD_3OH) was used to avoid the signal of methyl group of methanol. In addition, for the ^{13}C MAS NMR measurement, ^{13}C labeled methanol ($^{13}\text{CH}_3\text{OH}$) was used to increase ^{13}C abundance and therefore to made low-concentration reaction intermediate detectable.

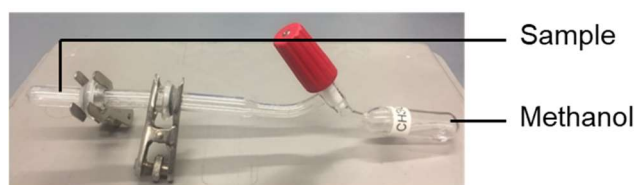


Figure 5.2 Methanol saturation procedure.

5.2.1.3 Water/Methanol Desorption

For ^1H MAS NMR measurements, the respective water or methanol saturated sample was filled into a glass tube as mentioned in the saturation step. Desorption was then performed at subsequently at increased temperatures (298 K, 323 K, 348 K, 373K, 423K, 473 K, 523 K, 573 K and 623 K) under vacuum ($p < 10^{-2}$ mbar). After desorption at one temperature for 30 minutes, the sample was disconnected from vacuum line, fast transferred into the glove box and sealed with a rotor cap under inert atmosphere. Before measuring using MAS NMR, gravimetric control is necessary for following quantification and implemented on a balance. After MAS NMR measurement, the rotor was opened in the glove box, filled in the glass tube and connected to the vacuum line for desorbing at the next temperature step.

For in-situ DRIFTS measurement, water or methanol saturated samples were filled in the in-situ chamber and continuously desorbed in 40 mL/min of N_2 flow with the same temperature program used for MAS NMR measurement. In between each 30-minute desorption step at one temperature, an IR image was quickly recorded.

5.2.2 Loading of Basic Probe Molecules

5.2.2.1 Acetonitrile Loading

Deuterated acetonitrile loading (CD_3CN) associated with ^1H MAS NMR is one of the methods for investigating acid strength on solid acids, especially on zeolites.^[74-77] In order to conduct the loading, the activated sample was prepared as described previously, packed into a 4 mm NMR rotor under dry nitrogen and a ^1H MAS NMR measurement performed. This step ensures a dry sample for the following probe molecule loading. After measurement, the rotor was opened in the glove box, put into a glass tube, connected to a vacuum line and evacuated for 10 min at 10^{-2} mbar. After evacuation, liquid CD_3CN was evaporated into the glass tube until a final pressure of 70 mbar was reached. After adsorption for 10 min, desorption of physisorbed CD_3CN was performed at 293 K for 12 h and the sample was measured by ^1H MAS NMR afterwards.

5.2.2.2 Ammonia Loading

Combination of ammonia loading and ^1H MAS NMR is commonly used for quantification of Brønsted and Lewis acid sites on solid catalysts.^{[75],[78],[79]} Similar like CD_3CN loading, an ^1H MAS NMR spectrum was collected for the activated sample. Then, the rotor filled with activated sample was transferred to the activation line for evacuation and contacted with 100 mbar of NH_3 gas for 10 min. The excessive NH_3 was subsequently removed in vacuum. To remove physisorbed NH_3 , the sample was heated up to 453 K for 2 h in vacuum with a heating rate of 3 K/min. After cooling down, the NH_3 loaded sample was weighed and measured with ^1H MAS NMR again.

5.2.2.3 Trimethylphosphine Oxide Loading

In contrast to the previous adsorptions of basic molecules from gas phase, trimethylphosphine oxide (TMPO) is solid. Thus, loading on different solid acids must be performed by placing 2 mg of TMPO on top of a rotor filled with 30 mg of dehydrated sample in glove box. The rotor was sealed with an O-ring-containing Torlon cap, put in a glass tube and heated at 433 K for 2 h. After cooling down, an equilibration for 12 h was required before ^{31}P MAS NMR measurement.

5.2.3 Solid-state NMR spectroscopy

The MAS NMR data were collected on a Bruker Avance III 400WB spectrometer at a magnetic field of 9.4 T. All measurements except ^1H were performed on sample in their fully

5. Experimental

hydrated states, if not otherwise stated. 4 mm rotors were used for measurements of ^1H , ^{23}Na , ^{27}Al , and ^{31}P nuclei with a spinning rate of 8 or 10 kHz, and 7 mm rotors were used for the ^{29}Si nucleus with a spinning rate of 3.5 kHz, if not otherwise stated. ^1H , ^{23}Na , ^{27}Al , ^{29}Si , and ^{31}P MAS NMR spectra were recorded at the resonance frequencies of 400.1 MHz, 105.8 MHz, 104.2 MHz, 79.5 MHz, and 161.9 MHz, respectively. For single-pulse excitation measurements, the pulse lengths are $\pi/2$ for ^1H , ^{29}Si , and ^{31}P , $\pi/4$ for ^{23}Na , and $\pi/8$ for ^{27}Al . Repetition times of 20 s for ^1H and ^{31}P , 0.5 s for ^{23}Na and ^{27}Al , and 30 to 120 s for ^{29}Si were used. ^{13}C CP MAS NMR measurements were acquired with a contact time of 3 ms and a repetition time of 5 s applying a 70–100% ramp during the Hartmann-Hahn contact period and `spinal64` decoupling during acquisition. The ^{29}Si CP MAS NMR measurements were performed with a contact time of 3 ms, a repetition time of 15 s, a 70–100% ramp and `tppm15` decoupling during the acquisition period. $^1\text{H}\{^{27}\text{Al}\}$ TRAPDOR measurements were performed on dehydrated samples with a repetition time of 20 s at 2.8 kHz spinning speed. All MAS NMR spectra were processed and simulated with the software DMFIT^[80] and TOPSPIN.

^{27}Al MQMAS NMR was measured Bruker Avance III 500 MHz spectrometer (11.7 T magnetic field) with a 3.2 mm triple resonance MAS probe by Dr. Bjørnar Arstad at SINTEF, Oslo, Norway. Measurements were performed with a three-pulse z-filtering sequence at the resonance frequency of 130.3 MHz and a spinning rate of 20 kHz.^[81] All data were processed by a shearing transformation.

For the quantification of ^1H MAS NMR measurements, a Na,H-Y zeolite sealed in a 4 mm rotor (35% Na^+ exchanged by ammonium, 58.5 mg, $n(\text{H}) = 1.776$ mmol/g) was used as an external standard and the quantity of ^1H can be calculated by the equation 5.1:

$$n(\text{H})_{\text{sample}} = \frac{n(\text{H})_{\text{standard}} \times m_{\text{standard}} \times I_{\text{sample}} \times RG_{\text{sample}} \times NS_{\text{sample}}}{m_{\text{sample}} \times I_{\text{standard}} \times RG_{\text{sample}} \times NS_{\text{sample}}} \quad (5.1)$$

where n is the quantity of the nucleus, m is the mass, I is the intensity of ^1H MAS NMR spectra, RG is the receiver gain and NS is the number of scans of the measurement. Ordinarily, the RG and NS are same. Therefore, equation (5.1) could be simplified to:

$$n(\text{H})_{\text{sample}} = \frac{n(\text{H})_{\text{standard}} \times m_{\text{standard}} \times I_{\text{sample}}}{m_{\text{sample}} \times I_{\text{standard}}} \quad (5.2)$$

5.2.4 In-situ Diffuse Reflectance Infrared Fourier Transform Spectroscopy

In situ diffuse reflectance infrared Fourier transform spectroscopy (In-situ DRIFTS) was recorded using a Nicolet iS50 FT-IR spectrometer equipped with a Harrick high temperature system consisting of a Praying Mantis[®] diffuse collection system and ATK-024-4 temperature controller. Prior to sample measurement, a background measurement was carried out by filling dry potassium bromide (KBr) in the in-situ chamber and using the same temperature program as later during the sample measurement (see 5.2.1.3). Data processing of in-situ DRIFTS spectra were accomplished by importing background measurement and applying Kubelka-Munk theory and atmosphere suppression using the OMNIC software package.

5.2.5 TGA-DSC

A Netzsch STA 449 F5 instrument, equipped with a Si/C furnace ($T_{\max} = 1873$ K) and Type S (Pt-10%Ru/Pt, $T_{\max} = 1923$ K) thermocouple, was used for thermogravimetric analysis and differential scanning calorimetry (TGA-DSC) measurements. Aluminum crucibles were used because of their high thermal conductivity and sensitivity for DSC detection.

Prior to sample measurements, temperature and heat calibration of TGA-DSC was necessary and implemented with a Netzsch standard calibration kit containing adamantane ($T_{\text{mp}} = 208.6$ K, $\Delta H = -22.0$ J/g), indium (In, $T_{\text{mp}} = 429.7$ K, $\Delta H = -28.6$ J/g), tin (Sn, $T_{\text{mp}} = 505.0$ K, $\Delta H = -60.5$ J/g), bismuth (Bi, $T_{\text{mp}} = 544.5$ K, $\Delta H = -53.1$ J/g), zinc (Zn, $T_{\text{mp}} = 692.1$ K, $\Delta H = -107.5$ J/g) and cesium chloride (CsCl, $T_{\text{mp}} = 749.1$ K, $\Delta H = -17.2$ J/g). Considering the following sample measurements would be conducted in the temperature range of 298-723 K with a heating ramp of 5 K/min, only the later 5 standard samples (In, Sn, Bi, Zn and CsCl) were used for calibration. The temperature program for different calibration materials listed in table 5.4 and the heating rate was same as the planned sample measurement, being 5 K/min. It is noteworthy to mention that the temperature program always includes 3 heating steps, *e.g.* for In, heating from 403 to 453 K with a heating rate of 5 K/min, and the last 2 heating steps were used for the evaluation. As recommended, for the measurement of Zn, only 2 heating steps were used in order to reduce the possibility of sublimation. Evaluation of onset temperatures and melting enthalpies were performed using Proteus Analysis software (NETZSCH). These results and mass of different materials (shown in the calibration kit) were finally filled in Temperature Calibration and Sensitivity Calibration software (NETZSCH).

5. Experimental

Table 5.4 Temperature program for calibration of TGA-DSC

Material	Temperature [K]	Repetition
In	403-453	3 times
Sn	463-533	3 times
Bi	503-573	3 times
Zn	653-723	2 times
CsCl	703-773	3 times

For sample measurements, a temperature program in the range from 298 to 723 K was applied as shown in figure 5.3. Aluminum crucibles filled with 5-11 mg water or methanol saturated samples (saturation method see section 5.2.1) were firstly heated from 298 K to 373 K to determine the adsorption enthalpy of weakly bounded molecules and then heated to 723 K to determine the adsorption enthalpy of strongly bounded molecules. In between the two heating steps, an isothermal step (373 K, 60min) and a cooling step (373-348 K, 5min) were performed. The isothermal step aims to completely remove weakly bounded molecules, while the cooling step ensures a stable heating rate in the second heating ramp since 373 K. A repetition of this heating-isotherm-cooling-heating process was implemented to create a baseline for the evaluation of DSC curves as described in literature.^[82] Evaluation of mass loss was from TGA curve in the first heating cycle. Evaluation of desorption energy from DSC curve was much more complicated. Generally, the heating steps with the same temperature range in both heating cycles, *e.g.* heating step 1 and 3 (see figure 5.3), was plotted against temperature in one figure and integrated with the same baseline. The resulting desorption energy was calculated by subtraction of integral in the second heating cycle from which in first heating cycle. Finally, desorption heat was obtained by the equation

$$\Delta H = \frac{\Delta E}{\Delta m} \quad (5.3)$$

where ΔE is the desorption energy and Δm is the mass loss.

5. Experimental

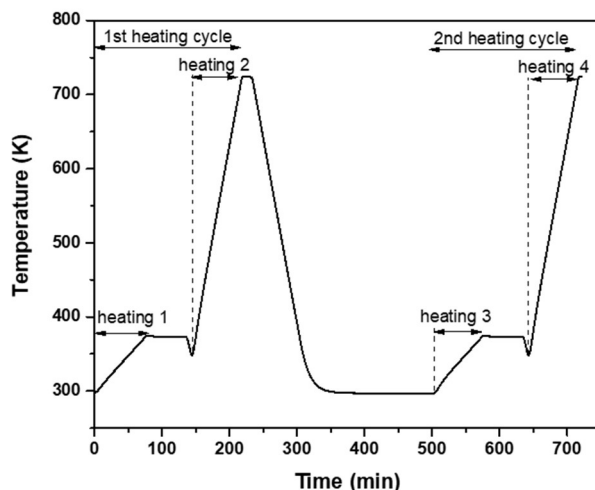


Figure 5.3 Complete temperature program applied for the TGA-DSC measurements.

5.2.6 Nitrogen Physisorption

Nitrogen physisorption measurements were conducted by Mrs. Ann-Katrin Beuer, Mrs. Dorothea Häussermann and Mr. Michael Benz on a Quantachrome Autosorb 3B device. Before N_2 adsorption at 77 K, samples were activated at 623 K for 16 h. Adsorption and desorption of N_2 gas was conducted in the relative pressure (p/p_0) range from 10^{-5} to 1. Surface areas were calculated in accordance with Brunauer-Emmett-Teller (BET) theory. The mesopore volume was calculated by subtraction of micropore volume, determined by the V-t method, from the total pore volume at $p/p_0 = 0.99$. Mesopore diameters were obtained from the adsorption branch applying the Barrett-Joyner-Halenda (BJH) method.

5.2.7 X-ray Diffraction

X-ray diffraction (XRD) measurements were performed on a Bruker D8 Advance diffractometer with a $CuK\alpha$ radiation. For microporous zeolites, XRD patterns were collected in the 2θ angular range of $4-50^\circ$ with a VANTEC-1 PSD detector. Mesoporous materials were measured using a Scintillation Counter detector in the 2θ angular range of $0.7-5^\circ$.

5.2.8 Chemical Analysis

Chemical compositions of different materials were determined by inductively coupled plasma optical emission spectrometry (ICP-OES). Typically, 3 mL of 10% fluoric acid mixed

5. Experimental

with 6 mL of aqua regia to dissolve 20-50 mg of the sample. The solution was diluted in a 250 mL volumetric flask with bi-distilled water and then measured on a Perkin Elmer Avio 200 ICP-OES instrument. All measurements were performed by Mrs. Heike Fingerle and Mrs. Nagme Merdanoglu.

5.2.9 Scanning Electron Microscopy

Scanning electron microscopy (SEM) images were taken by Dr. Hang Liu on a TESCAN VEGA3 XM instrument with a tungsten filament as electron source and 10 kV accelerating voltage. Secondary electrons were detected for imaging. For the measurements, the samples were prepared as follows: Few material was dispersed in acetone or ethanol in a vial with the help of ultrasonic for about 30 min. Some drops of the well dispersed mixture were dripped on a polished silicon wafer (Plano GmbH) for the following measurement.

5.2.10 Transmission Electron Microscopy

Transmission electron microscopy (TEM) images were acquired with a Philips CM-200 FEG TEM by Dr. Qian Song. Similar like the preparation of SEM sample, few materials were added into acetone or ethanol. Dispersion was performed with the help of ultrasonic for about 30 min, and then three drops of the well dispersed mixture were dripped on a copper mesh for the following TEM measurement. Evaluation of TEM images proceeded using Digital Micrograph software (Gatan).

6. The Alumination of Porous Silica with Sodium Aluminate

6.1 Introduction

Acid properties determine the success of many heterogeneous catalysts on their various industrial applications. Post modification is one of the popular methods to introduce acidity into heterogeneous systems and to adjust the acidity. Microporous zeolites normally have aluminum on their framework and acidic protons present as compensation of negative charge of aluminum. If the acid site density is too high to maintain the zeolite structure under reaction conditions, dealumination procedures are applied to remove framework aluminum. Steaming treatment of zeolite is a feasible process, often used to obtain ultra-stable catalysts, *e.g.* USY zeolite, with high Si/Al for the fluid catalytic cracking (FCC) of petroleum.^[83] However, extra-framework aluminum (EFAl), causing detrimental side reactions, forms during steaming. A subsequent acid leaching is therefore indispensable in order to eliminate the undesired performance.^[84] Unfortunately, this acid treatment can lead to unexpected further dealumination.^[85] Aluminaiton by pos-modification is therefore a promising way to re-introduce acid sites into dealuminated zeolites.

For the conversion of large substrates, pore diameters in mesoporous range (2 to 50 nm) are more suitable. The mesoporous silica with ordered pore structure are typically synthesized using polymer templates.^{[73],[86]} Some of them, such as SBA-15 and SBA-16, possess thick pore wall and high stability at elevated temperatures, which develops their potential to be catalysts under harsh reaction conditions. The acidic SBA-15 and SBA-16 can achieve either by introducing aluminum sources via the synthesis routes.^{[43],[87],[88]} Unfortunately, only a minor part of aluminum is incorporated into the lattice, rendering the surface of these catalysts to a certain extent undefined due to the formation of extra-framework aluminum (EFAL). An alternative is post modification of siliceous forms.^{[37],[44],[48],[89],[90]} Zhang et al. firstly reported the alumination of DeA-Y with sodium aluminate (NaAlO_2) solution.^[90] Luan et al. later applied this method on SBA-15.^[37] Comparing with other aluminum resource, AlCl_3 and $\text{Al}(\text{O}^i\text{Pr})_3$, the alumination with NaAlO_2 is the most commonly used method now as the cheap price of the only chemical, NaAlO_2 , the easy process and the incorporation of tetrahedral coordinated aluminum. Hamdan et al. also applied this method on MCM-41 and found high temperature promotes aluminum build in whereas MCM-41 transformed to zeolite A under too high temperatures.^[91] Optimum conditions for the alumination of SBA-materials were not presented until now.

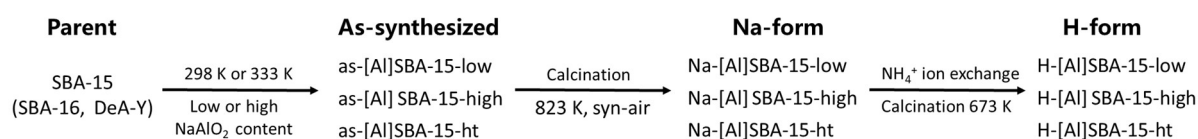
6. The Alumination of Porous Silica with Sodium Aluminate

Studies on the physicochemical and acid properties of parent and modified DeA-Y and SBA-15 materials after alumination have been reported. When alumination is executed with AlCl_3 , aluminum atoms react with the $\text{Si}(\text{OH})$ groups on the surface of DeA-Y and SBA-15.^[48] However, acid strength of BAS is weak on both DeA-Y and SBA-15. While, when alumination is conducted with $(\text{NH}_4)_3\text{AlF}_6$ solution, EFAl appears when Si/Al ratio is smaller than 10 even without removal of NH_3 .^[89] Talha et al. deposited a little aluminum (Si/Al = 50 or more) on SBA-15 using NaAlO_2 solution and found an intensive decrease of BET surface area as well as micropore volume combined with thickening of the pore wall.^[92] In addition, the density of silanol groups diminish after alumination. $^1\text{H}\{^{27}\text{Al}\}$ TRAPDOR MAS NMR measurements were performed by Hu et al. to illustrate the properties of hydroxyl groups after NaAlO_2 treatment.^[93] In their study, no Brønsted acid site (BAS) is observed in the aluminated SBA-15, whereas signal intensity of $\text{Si}(\text{OH})$ groups at 1.8 ppm decreases upon Al-irradiation, indicating proximity between aluminium atoms and $\text{Si}(\text{OH})$ groups. By loading of trimethylphosphine (TMP) and trimethylphosphine oxide (TMPO), only a very low quantity (10% of aluminium content) of BAS is detected, although ion exchange to H-form was not carried out. Different from Luan's result, an intensive signal at around 0 ppm presents in the ^{27}Al MAS NMR spectra, which indicates a lot of EFAl present in the [Al]SBA-15. However, no Lewis acid sites (LAS) are observed on these materials. Although literature reports the alumination procedure of NaAlO_2 and properties of aluminated materials, the mechanism of this post modification method and the influence of reaction parameters on acidity of NaAlO_2 modification are still unknown now.

Herein, we investigate the NaAlO_2 modification of microporous dealuminated Y zeolite and mesoporous SBA-15 and SBA-16 materials with MAS NMR technique to illustrate the mechanism and optimize the properties of the resulting Na- and H-form materials. Partial dissolution of silica structure and reaction with surface $\text{Si}(\text{OH})_x$ groups simultaneously happen in the NaAlO_2 solution. Removal of NH_3 from NH_4 -form leads to redistribution of aluminum atoms and generates extra-framework aluminum. An in-depth research of acid properties was conducted by loading materials with probe molecules. Combination of mechanism and acid property study helps improving the alumination process via adjusting reaction parameters. It is found that pore shape and size influence the alumination procedure. As result of our study, the alumination of porous silica with various pore system is understandable and applicable.

6.2 Physicochemical Characterization

For summarizing the samples and their synthesis procedure, Scheme 6.1 explains the modification route of porous materials. As mentioned in the experimental chapter, siliceous materials of SBA-15, SBA-16 and DeA-Y were synthesized or purchased as parent materials for aluminations. Three different conditions (see 5.1.5) were applied to synthesize different aluminated materials and the resulting materials were accordingly named with suffixes of “-low”, “-high” and “-ht”. The prefixes, “As-”, “Na-” and “H-” indicated different forms of materials produced during the whole modification process.



Scheme 6.1 Aluminations and subsequent ion exchange route of porous silica materials.

XRD patterns of parent and aluminated materials of SBA-15, SBA-16 and DeA-Y are shown in figures 6.1-6.3. For parent SBA-15, the hexagonal $p6mm$ mesophase is verified by small-angle diffraction pattern and reflections of the (100) plane, (110) plane, and (200) plane located at 0.96° , 1.67° and 1.93° , respectively. After aluminations, all three reflections appear likewise, but the reflection maxima slightly shift to the higher angle. The reflection of (110) plane in cubic $Im3m$ mesophase of all SBA-16 materials are found in the respective XRD pattern around 0.77° . These reflection angles for SBA-15 and SBA-16 are in good agreement with literature.^[73] The almost constant values prove an intact mesopore systems in SBA-15 and SBA-16 materials before and after aluminations. A series of characteristic reflections are found in the wide-angle powder XRD patterns of DeA-Y. They correspond well with the typical diffraction patterns of FAU type zeolites accessible in the IZA database.^[2] Similar powder diffraction patterns were collected from the aluminated DeA-Y samples. Noteworthy, no reflections of other phase appear before or after modification. This confirms the pure and intact phase of [Al]DeA-Y materials.

6. The Alumination of Porous Silica with Sodium Aluminate

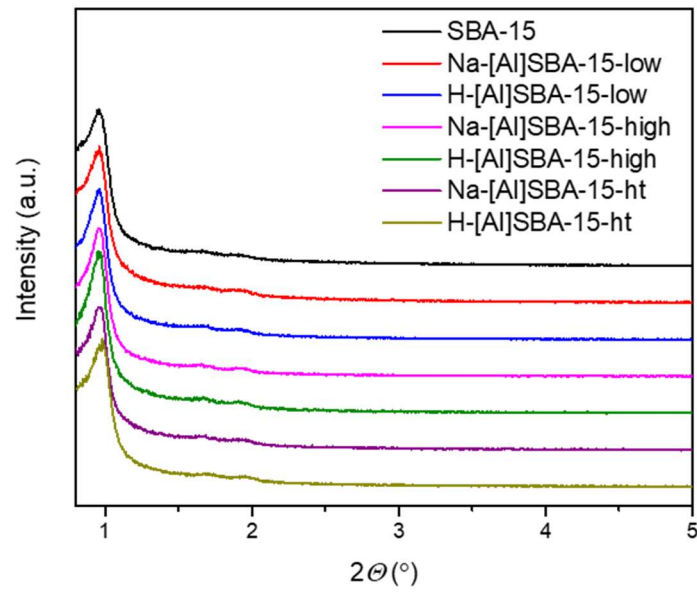


Figure 6.1 XRD patterns of parent SBA-15 and different [Al]SBA-15 materials.

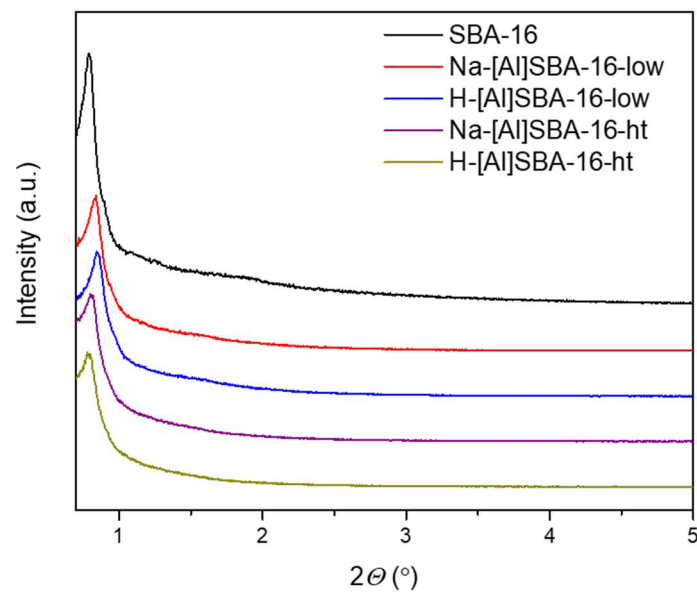


Figure 6.2 XRD patterns of parent SBA-16 and different [Al]SBA-16 materials.

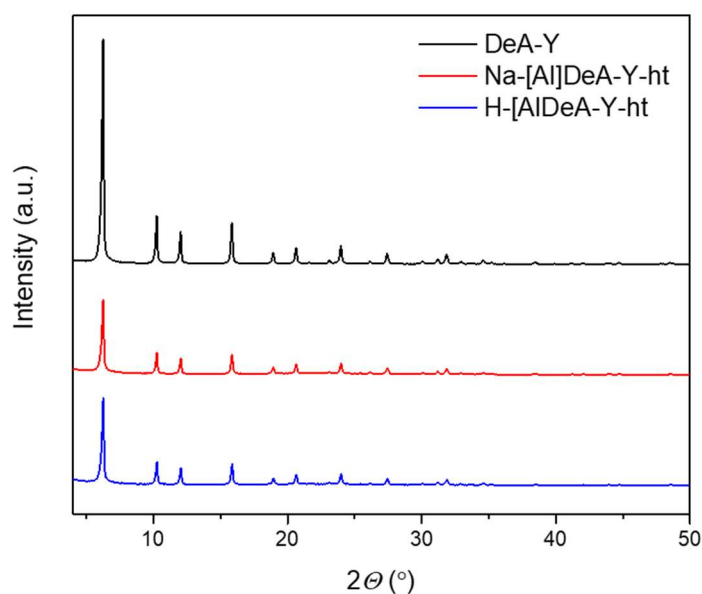


Figure 6.3 XRD patterns of DeA-Y and [Al]DeA-Y-ht materials.

Upon modification, materials with different quantities of aluminum were prepared. It is always important for industrial application to have high atom efficiency and to avoid unnecessary element enrichment. Therefore, a comparison of aluminum quantities between raw materials and products is necessary. As it is shown in table 6.1, most aluminum or NaAlO_2 is built into SBA-15 and thus only very small amounts (ca. 17%) of NaAlO_2 get lost. SBA-16 has a 3D-mesopore system and 62-71% of Al deposits on the silica surface at room temperature. High temperature improves the alumination efficiency on SBA-16 that is same as on SBA-15. It hints the pore structure strongly influence the diffusion of NaAlO_2 . If the pore structure is complicated, aluminum is difficult to link the deep inner surface under mild condition. For microporous DeA-Y zeolite, discrepancy between aluminum contents in raw material and in product is high even at high temperature. The reason could be that smaller amount of silanol groups (0.18 mmol/g) for building aluminum exists on DeA-Y.^[48] However, it should be noted that aluminum content in [Al]SBA-15-ht (0.7 mmol/g) is much higher than the initial quantity of silanol groups, which implies that partial framework is dissolved in the alkaline solution as explained in literature.^[90] Nevertheless, NaAlO_2 treatment is ineffective to generate enough silanol nests for insertion of aluminum. Thus, the NaAlO_2 modification is most effective in the straight-pore-structure SBA-15 materials.

Table 6.1 Aluminum contents of raw materials and products

Product	Al (raw) [mmol/g]	Al (product) [mmol/g]
Na-[Al]SBA-15-low	0.6	0.5
Na-[Al]SBA-15-high	1.3	1.0
Na-[Al]SBA-15-ht	1.3	1.1
Na-[Al]SBA-16-low	0.7	0.5
Na-[Al]SBA-16-high	1.3	0.8
Na-[Al]SBA-16-ht	1.3	1.1
Na-[Al]DeaY-ht	1.3	0.7

a) From ICP-OES experiments, accuracy $\pm 10\%$.

N₂ physisorption disclose important physicochemical properties of these materials. and the results are list in table 6.2. The BET surface areas of parent materials are typical for the respective structures and amount to more than 700 m²/g for the respective parent materials. However, modification leads to a strong decrease of BET surface areas. For SBA-15, the harsher the alumination condition (higher NaAlO₂ content and higher reaction temperature), the smaller the surface area received for the aluminated product. When alumination is performed at 333 K with high amount of NaAlO₂, the BET surface area of the final modification product H-[Al]SBA-15 is only half of the BET area that was measured for the parent SBA-15. Noteworthy, as result of alumination the initially present micropores vanish. Such a diminishing of surface area and micropores is commonly reported in literature^{[37],[92]} and is a result of the mild synthesis conditions for the parent SBA-15. A lower temperature (<403 K) makes SBA-15 unstable in aqueous environment and leads to the subsequent loss of the initially present micropores, and with them a share of the initial surface area, during the modification process.^[94] However one cannot exclude the possibility that micropores were filled by aluminum upon collapse. In contrast to the (in this study not important) micropores present in the parent, the mesoporosity of SBA-15 is almost unaffected by the applied modification. The mesopore volume only slightly decreases from 0.76 up to 0.61 mL/g and the calculated mesopore diameter remains also comparable. As shown in figure 6.4, the pore size distributions calculated after applying the BJH method on the adsorption branches of [Al]SBA-15-ht materials do not change even after harsh conditions.

6. The Alumination of Porous Silica with Sodium Aluminate

Table 6.2 Data of physicochemical properties of materials in this study

Material	Hydroxyl density [mmol/g]	Na content [mmol/g] ^{a)}	K/Na exchange [%] ^{a)}	surface area [m ² /g]	V _{micro} [mL/g]	V _{meso} [mL/g]
SBA-15	1.38	<0.01	-	700	0.08	0.76
Na-[Al]SBA-15-low	1.19	0.43	>99%	510	0.03	0.88
H-[Al]SBA-15-low	1.36	<0.01	-	430	0.01	0.69
Na-[Al]SBA-15-high	0.78	0.67	>99%	390	0.01	0.64
H-[Al]SBA-15-high	1.01	<0.01	-	390	0.01	0.67
Na-[Al]SBA-15-ht	0.82	0.98	>99%	370	0.00	0.64
H-[Al]SBA-15-ht	0.97	0.02	-	340	0.00	0.61
SBA-16	2.33	<0.01	-	750	0.20	0.28
Na-[Al]SBA-16-low	0.8	0.25	99%	330	0.00	0.40
H-[Al]SBA-16-low	2.12	<0.01	-	350	0.01	0.40
Na-[Al]SBA-16-ht	0.57	0.68	99%	170	0.00	0.36
H-[Al]SBA-16-ht	0.81	0.07	-	230	0.00	0.48
DeA-Y	0.18	0.01	-	820	0.28	0.16
Na-[Al]DeaY-ht	0.85	0.54	>99%	490	0.14	0.42
H-[Al]DeaY-ht	1.42	<0.01	-	540	0.16	0.30

a) From ICP-OES experiments, accuracy $\pm 10\%$.

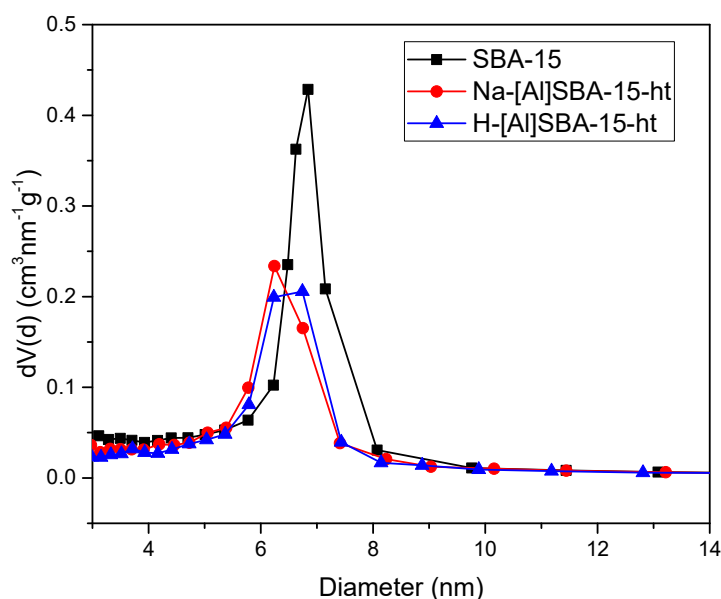


Figure 6.4 Pore size distributions of SBA-15, Na-[Al]SBA-15-ht and H-[Al]SBA-15-ht from the adsorption batch of physisorption measurements with BJH method.

A strongly plunge of BET surface area happens on SBA-16 materials and the surface areas of [Al]SBA-16-ht materials, 170-230 m^2/g , are less than a quarter of the parent's (750 m^2/g). Interestingly, NH_4^+ ion exchange and calcination of the NH_4 -form of SBA-16 into H-form increases the surface area in both “-low” and “-ht” materials. But the minor increase does not turn the trend and all the surface areas of [Al]SBA-16 are lower than half of the siliceous SBA-16. The decrease of BET surface area and absence of micropores in [Al]SBA-16 materials seem again because of the water treatment. It is noteworthy that the pore size distribution of high-temperature modified sample intensely broadens, as shown in figure 6.5, but this broadening was not revealed when modification was conducted in a milder condition. Therefore, SBA-16 shows a more unstable property than SBA-15, for which physisorption properties were extremely altered by surface dissolution and aluminum deposition. Comparing with SBA-15, it is probably due to the 3D pore system of SBA-16 containing smaller pores and bigger cavities, which means some highly soluble structures such as thin walls with a positive radius and high curvature appears in a pore.^[94,95] However, it must be confessed that the pores stay intact as supported by the XRD patterns discussed above and the TEM images show below.

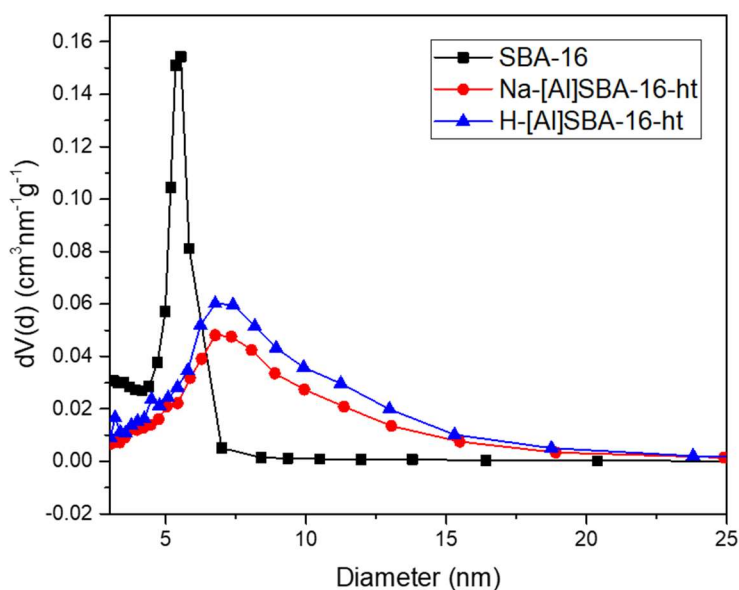


Figure 6.5 Pore size distributions of SBA-16, Na-[Al]SBA-16-ht and H-[Al]SBA-16-ht from the adsorption batch of physisorption measurements with BJH method.

Parent DeA-Y zeolite owns the highest BET surface area ($820 \text{ m}^2/\text{g}$) and micropore volume (0.28 mL/g) as well as the lowest mesopore volume (0.16 mL/g) among the three siliceous parent materials. However, this mesopore volume is already three times as large as it would be in the normal Y zeolite directly after formation of the FAU phase. This phenomenon is commonly attributed to the intra-crystalline mesopores produced during the dealumination process of the material.^{[96],[97]} The mesopore size distributions of DeA-Y zeolites (figure 6.6) are expansive, as they are no defined pore system, and further broadening after alumination. It is worthy noted that the presence of these irregular mesopores once has been deemed to explains why molecular diffusion in dealuminated zeolites is always better than in their parent.^[98] However, electron microscopy and PFG NMR studies confirm that most of these mesopores are surrounded by micropores and have few efficiency in connection with external surface.^{[97],[99]} The mesopore volume illustrates that post-modification in alkaline solution can induce mesopores not only for mesoporous materials SBA-16 but also for microporous zeolites, which is consistent with the previous finding in modification of ZSM-22 zeolite.^[100] After alumination, the BET surface area decreased to $490 \text{ m}^2/\text{g}$ in Na-[Al]DeA-Y-ht, while the mesopore volume increased to 0.42 mL/g . Subsequent modification to H-[Al]DeA-Y-ht slightly increased the BET surface area to $540 \text{ m}^2/\text{g}$, however, this is accompanied by again losing some mesopore volume to a final 0.30 mL/g . It is noted that, different from SBA-15 and

6. The Alumination of Porous Silica with Sodium Aluminate

SBA-16, the NaAlO_2 treatment does not destroy all the micropores in $[\text{Al}]\text{DeA-Y-ht}$ due to the low amount of silanol groups as mentioned above.

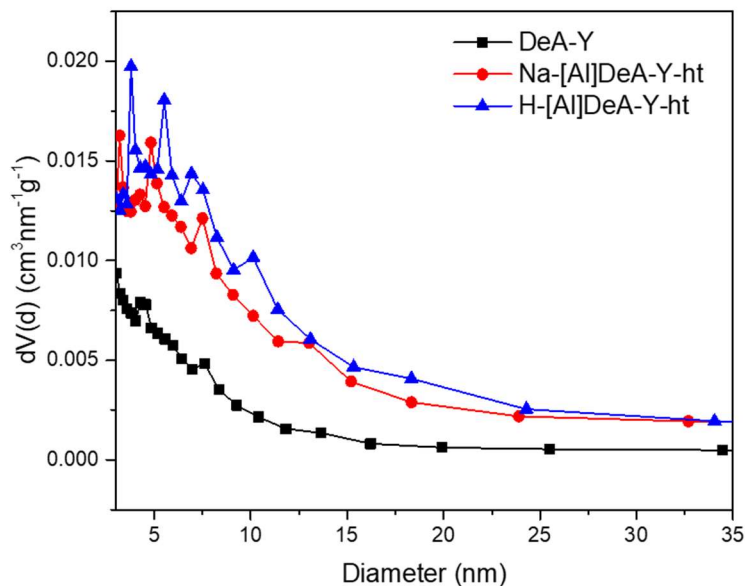


Figure 6.6 Pore size distributions of DeA-Y, Na-[Al]DeA-Y and H-[Al]DeA-Y from the adsorption batch of physisorption measurements with BJH method.

In a next step, the performance of materials as ion exchangers are checked. This ion-exchange property is meaningful as the counter ions of aluminated materials could then be adjusted and materials be used as catalysts for certain reactions or gas adsorption and separation applications.^{[37],[101-103]} As test case, herein we exchanged Na^+ ions on Na-form materials with ammonium (NH_4^+) and potassium (K^+) ions. The results of these exchanges are shown in the second and third columns in table 6.2. Most of Na^+ ion can be easily and fully transferred into their K^+ forms. XRD patterns show identical peaks for Na- and K-[Al]SBA-15-ht materials. In ^{27}Al MAS NMR spectra, signal maxima of both materials are at 53 ppm, which conforms all aluminum atoms are in tetrahedral coordination before and after ion exchange. Thus, on all materials we could ensure that within measurement accuracy all Na^+ counter ions can be ion exchanged into K^+ counter ions without destroy the structure of materials. Therefore, all ion exchange sites are fully accessible for other counter ions and the materials are thus suited as ion exchangers or catalyst supports.

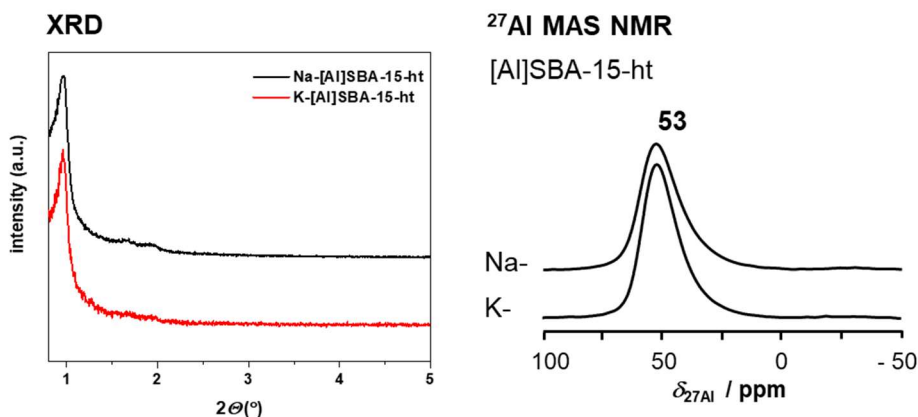


Figure 6.7 XRD patterns (left) and ^{27}Al MAS NMR spectra (right) of Na- and K-form of [Al]SBA15-ht.

The scanning electron microscopy (SEM) images of the parents and modified materials are shown in the following figures. SBA-15 is a rod-like material with a regular length of about $1\ \mu\text{m}$ (figure 6.8). In contrast, the particle size of cubic SBA-16 (figure 6.9) is larger (ca. $5\ \mu\text{m}$) but more irregular than SBA-15. Structures of the two mesoporous materials fit well literature and convince a successful synthesis. DeA-Y particles are, due to their commercial synthesis, much smaller and in a nanoscale range (figure 6.10). After each modification step, the materials exhibit similar particle shapes as their parents. In addition, TEM images of mesoporous materials clearly display the channels in SBA-15 (figure 6.11) and SBA-16 (figure 6.12). It is obvious that the one-dimensional pores in SBA-15 are intact and no obstruction appears even suffering from the harsher modification condition. TEM images of SBA-16 are slightly blurry due to the complicated 3D pore system and the bad resolution of instrument. But, from the collected images, no visible changes of pore structure can be found in modified SBA-16 materials.

6. The Alumination of Porous Silica with Sodium Aluminate

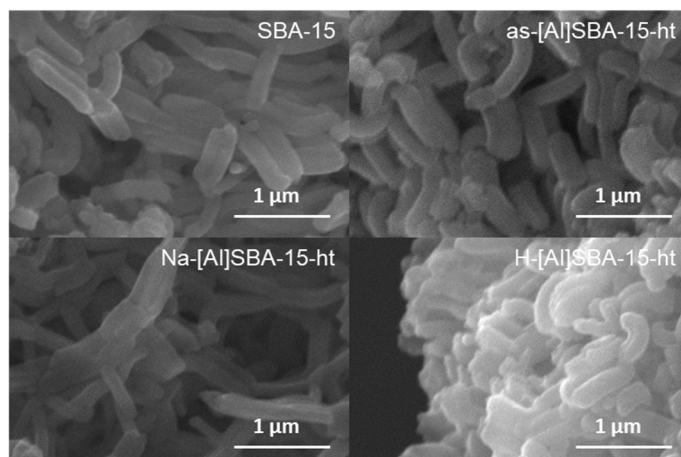


Figure 6.8 SEM pictures of SBA-15, as-[Al]SBA-15-ht, Na-[Al]SBA-15-ht and H-[Al]SBA-15-ht materials.

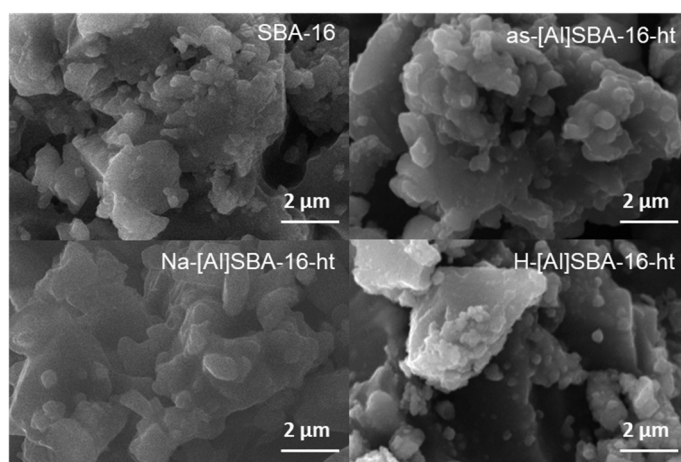


Figure 6.9 SEM pictures of SBA-16, as-[Al]SBA-16-ht, Na-[Al]SBA-16-ht and H-[Al]SBA-16-ht materials.

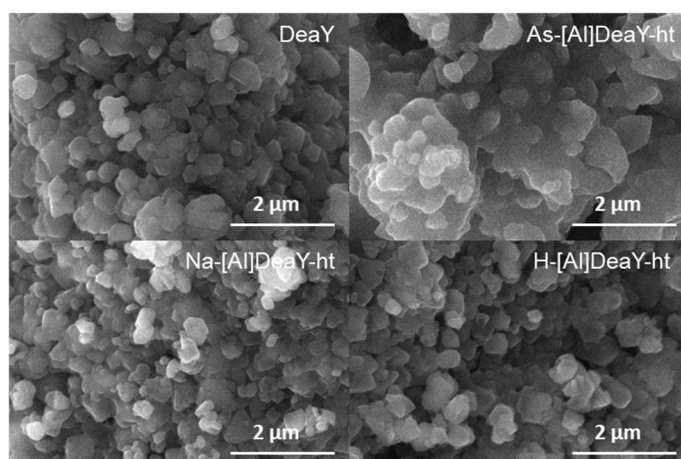


Figure 6.10 SEM pictures of DeA-Y, as-[Al]DeA-Y-ht, Na-[Al]DeA-Y-ht and H-[Al]DeA-Y-ht materials.

6. The Alumination of Porous Silica with Sodium Aluminate

A comparison of the mesopore diameters received from N₂ physisorption measurements applying the BJH-method (see figure 6.4 and figure 6.5) and pore diameters from TEM images is shown in table 6.3. The mesopore diameters of SBA-15 materials of parent and modifications are similar for N₂ physisorption measurement or TEM images. Noteworthy, the results from TEM images, where thickness of pore wall is included, are always larger than the corresponding results received from N₂ physisorption, where only the pore volume is taken into account. The mesopore diameter from N₂ physisorption increases after NaAlO₂ modification of SBA-16, whereas in the results from TEM it does not change remarkably. A possible explanation is, that under high-temperature alumination, the overall structure of SBA-16 is stable, but the pore system is partially dissolved as reported of MCM-41.^[94]

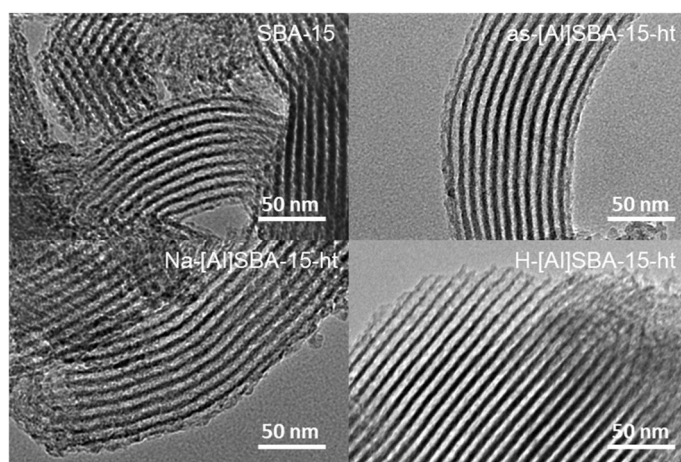


Figure 6.11 TEM pictures of SBA-15, as-[Al]SBA-15-ht, Na-[Al]SBA-15-ht and H-[Al]SBA-15-ht materials.

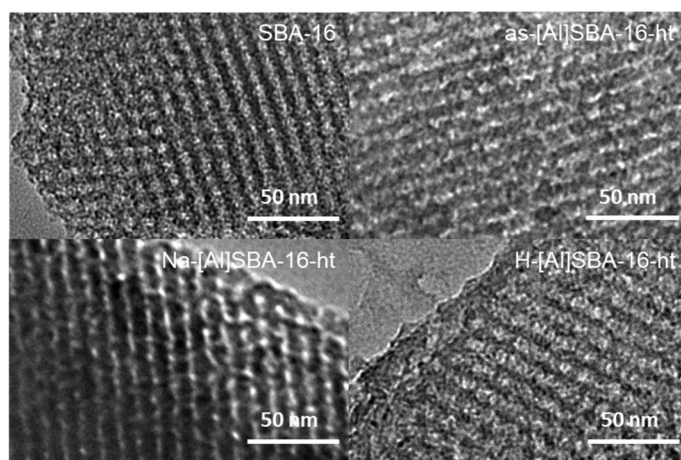


Figure 6.12 TEM pictures of SBA-16, as-[Al]SBA-16-ht, Na-[Al]SBA-16-ht and H-[Al]SBA-16-ht materials.

Table 6.3 Comparison of mesopore diameter of SBA-15 and SBA-16 from N₂ physisorption and TEM

Material	Mesopore diameter [nm]	
	N ₂ physisorption ^{a)}	TEM
SBA-15	6.8	8.3
Na-[Al]SBA-15-ht	6.7	8.8
H-[Al]SBA-15-ht	6.7	8.6
SBA-16	5.5	10.1
Na-[Al]SBA-16-ht	6.8	10.3
H-[Al]SBA-16-ht	6.8	10.5

a) From N₂ physisorption, adsorption batch.

In summary, the silica structure of SBA-15, SBA-16 and DeA-Y are partially dissolved and rebuilt under the alkaline condition and SBA-15 is much stable than SBA-16. However, XRD, SEM and TEM measurements confirm unchanged shapes of all kinds of materials after the stepwise modification.

6.3 Mechanism of Alumination

In order to uncover the mechanism of NaAlO₂ modification of siliceous materials, MAS NMR spectroscopy was applied during the various synthesis steps. It detects the sites present on the parent, as-synthesized form, Na-form and H-form of SBA-15, SBA-16 and DeA-Y samples, respectively. A complete overview of the surface sites can only be gained by combining multiple spectroscopy techniques. Thus, first a summary of their application shall be given. The single-pulse excitation ²⁹Si MAS NMR and the ²⁹Si CP MAS NMR spectra detect silicon nuclei without and with enhancement from nearby protons. These spectra are shown in figure 6.13. Table 6.4 lists the assignments of signals found in these ²⁹Si spectra. ²⁷Al MAS NMR and ²⁷Al MQMAS NMR spectra reveal the coordination of aluminum nuclei in aluminum-containing materials. The respective spectra are shown in figure 6.14 and 6.15. ¹H{²⁷Al} TRAPDOR MAS NMR (figure 6.16) allows to distinguish the aluminum-neighboring hydroxyl surface groups from other surface hydroxyl groups in the Na- and H-form materials. Spectra of Na⁺ ions are investigated by direct excitation ²³Na MAS NMR spectroscopy and shown in figure 6.17.

6.3.1 Parent materials

Considering the parent materials are porous silica, ^{29}Si MAS NMR and ^{29}Si CP MAS NMR measurements were applied to detect their matrixes and the results are shown in figure 6.13. The purely siliceous, mesoporous parents SBA-15 and SBA-16 contain three types of silicon nuclei, framework silicon ($\text{Si}(\text{OAl})$, Q^4 type) and two kinds of silanol groups ($\text{Si}(\text{OH})$, Q^3 type, and $\text{Si}(\text{OH})_2$, Q^2 type), with respective chemical shift of $\delta_{29\text{Si}}$ at -110, -101 and -92 ppm. Signals are broad due to the amorphous structure of SBA materials. As the quantum spin of ^{29}Si nucleus is 1/2, the ^{29}Si MAS NMR is a quantitative method and thus the signal intensity in ^{29}Si MAS NMR spectra reflects the quantity of different types of silicon.^[104] It is obvious that most silicon atom in SBA-15 and SBA-16 are located in the framework. Lots of $\text{Si}(\text{OH})$ and some $\text{Si}(\text{OH})_2$ appear in both of SBA. From the ratio of intensities, $(2\text{Q}^2+\text{Q}^3)/\text{Q}^4$, SBA-16 involves more silanol groups than SBA-15, which is consistent with results from ^1H MAS NMR (silanol groups: SBA-15, 1.38 mmol/g; SBA-16, 2.33 mmol/g). Signals of $\text{Si}(\text{OH})_x$ ($x = 1-2$) are enhanced using the cross-polarization technique. Therefore, the signal of Q^3 is most intensive in ^{29}Si CP MAS NMR spectra. DeA-Y zeolite only shows a slim signal at -107 ppm in ^{29}Si MAS NMR that can be assigned to framework silicon.^[105] Comparing with the spectrum of ^{29}Si CP MAS NMR, where signals at -101 and -92 ppm emerge, one can conclude that DeA-Y zeolite has few $\text{Si}(\text{OH})_x$ ($x = 1-2$) groups (0.18 mmol/g from complementary ^1H MAS NMR measurements).

6. The Alumination of Porous Silica with Sodium Aluminate

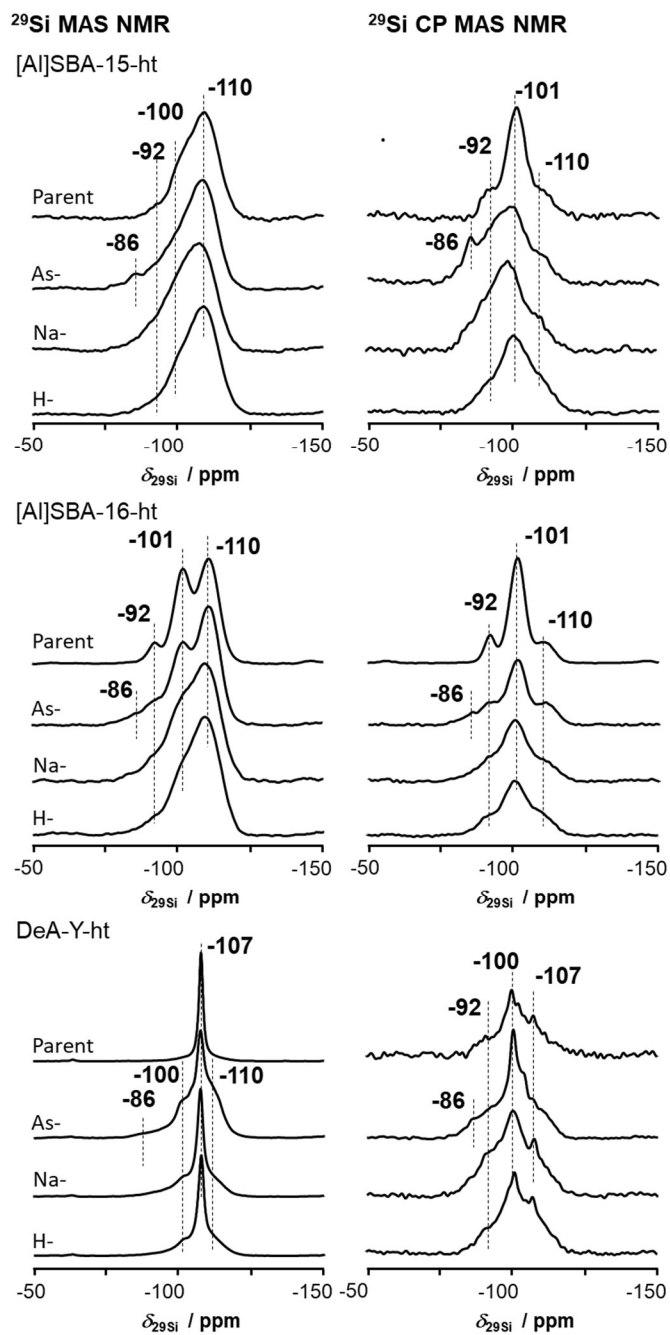


Figure 6.13 ²⁹Si MAS NMR (left) and ²⁹Si CP MAS NMR (right) of [Al]SBA-15-ht, [Al]SBA-16-ht and [Al]DeA-Y-ht samples (from top to bottom). Each series of samples contain the parent, as-synthesized form, Na-form and H-form materials.

Table 6.4 Peak assignments of ^{29}Si and ^{29}Si CP MAS NMR measurement

Chemical shift [ppm]	Si Species	References
-107 to -110	Si(0Al)	[106-110]
-101	Si(1Al), Si(2Al)	[106-108],[110]
	Si(OH)	[109-113]
-92	Si(3Al)	[107],[108]
	Si(OH) ₂	[109-114]
	Si(OH)(1Al)	[93]
-86	Si(4Al)	[105],[107-109],[112]
	Si(OH) ₃	[106],[109],[113],[114]

6.3.2 Transform into as-synthesized materials

After modification with NaAlO_2 solution, the as-synthesized materials were acquired. Since sodium and aluminum atoms should deposit on the siliceous parent materials during aluminations, not only ^{29}Si MAS NMR and ^{29}Si CP MAS NMR measurements but also measurements involving the additional nuclei ^{27}Al and ^{23}Na were performed on the as-synthesized materials.

Comparing the ^{29}Si MAS NMR spectra (figure 6.13, left) of as-[Al]SBA-15 and as-[Al]SBA-16 with their parents, signal at -101 ppm is weaker, signal at -92 ppm is broader and a new signal at -86 ppm appears. The similar tendency of signals also shows in ^{29}Si CP MAS NMR spectra (figure 6.13 right). By comparing the change of intensity of signal at -101 ppm with the Q^4 signal (at -110 ppm) in both ^{29}Si MAS NMR and ^{29}Si CP MAS NMR spectra, this signal is assigned into the mixture of Si(OH) and aluminum-containing species (Si(1Al) and Si(2Al)) forming in reaction of NaAlO_2 with the silanol (Si(OH) and Si(OH)₂) groups. In addition, the signal at -86 ppm is more likely attributed to Si(OH)₃ than to Si(4Al) species, due to wide absence of the latter in such materials and the strong enhancement in CP (cross-polarization) measurement. The signal intensity at -92 ppm in CP (cross-polarization) measurement is constant in [Al]SBA-16-ht but increases in [Al]SBA-15-ht compared to their parent materials, which denotes that more Si(OH)₂ groups in [Al]SBA-15 form after alkaline (pH of aqueous is 10 to 11.5) treatment. The chemical shift of -92 ppm denotes another aluminum-containing species, Si(OH)(1Al), which could be formed by the reaction of NaAlO_2 with Si(OH)₂. Considering CP and measurements involving ^{27}Al (see below), such a species is

6. The Aluminations of Porous Silica with Sodium Aluminate

more feasible than a mixture of Si(OH)_2 and Si(3Al) . The presence of a signal at -86 ppm and increase of signal at -92 ppm prove Si(OH) formation and thus a partial dissolution of siliceous structure in alkaline NaAlO_2 solution, as observed by others.^[92] For DeA-Y zeolite, after NaAlO_2 treatment, the slim signal of framework aluminum at -107 ppm diminishes and three new signals at -110, -92, and -86 ppm present in ^{29}Si MAS NMR spectrum. In the ^{29}Si CP MAS NMR spectrum, signals at -101, -92 and -86 ppm assigned to Si(OH)_x ($x = 1-3$) groups are detectable. The signal at -110 ppm in direct excitation measurement reveals a new kind of Q^4 silicon atoms. Considering the same chemical shift as Q^4 signal in SBA-15 and SBA-16, it hints an amorphous silica structure is formed also on crystalline DeA-Y zeolite during aluminations. Thus, the new silanol groups (Si(OH)_x ($x = 1-3$)) as well as the amorphous Q^4 structure support the partial dissolution of the zeolite framework, which also interprets why the final quantity of aluminium is much higher than the initial quantity of silanol groups (section 6.2, paragraph 3). This finding also explains literature findings, that aqueous alkaline solution is necessary for the realumination process of Y type zeolite.^[90]

In figure 6.14, ^{27}Al MAS NMR spectra offer the coordination type of aluminum in three as-synthesized materials. For as-[Al]SBA-15-ht and as-[Al]DeA-Y-ht, signals of ^{27}Al nuclei are found at about 55 ppm. This is in the common chemical shift range of tetrahedral coordinated aluminum in zeolite. Note that the peak is strongly shifted to higher field compared with the chemical shift of aluminum source, pure NaAlO_2 (around 80 ppm).^[115] This indicates the environment of aluminum atoms changes that aluminum atoms link on the silica surface via Al-O-Si bonds and that no precursor remained after aluminations treatment. No visible signal is found in the range of pentahedral coordination (25-40 ppm) and octahedral coordination (0-15 ppm).^[67] In contrast, as-[Al]SBA-16 contains octahedral coordinated aluminum, indicated by a signal at 5 ppm. Thus, we can conclude that the aluminations performance of SBA-15 is better than that of SBA-16 in not only element efficiency (table 6.1) but also the coordination structure. Al(OH) groups are not detectable for as-synthesized materials as a $^1\text{H}\{^{27}\text{Al}\}$ TRAPDOR MAS NMR measurement needs to be performed with dry sample, which would significantly change the surface of the materials. However, since they are present in Na-form materials (discussion see below, section 6.3.3), we can confirm that Al(OH) groups should also exist in as-synthesized materials.

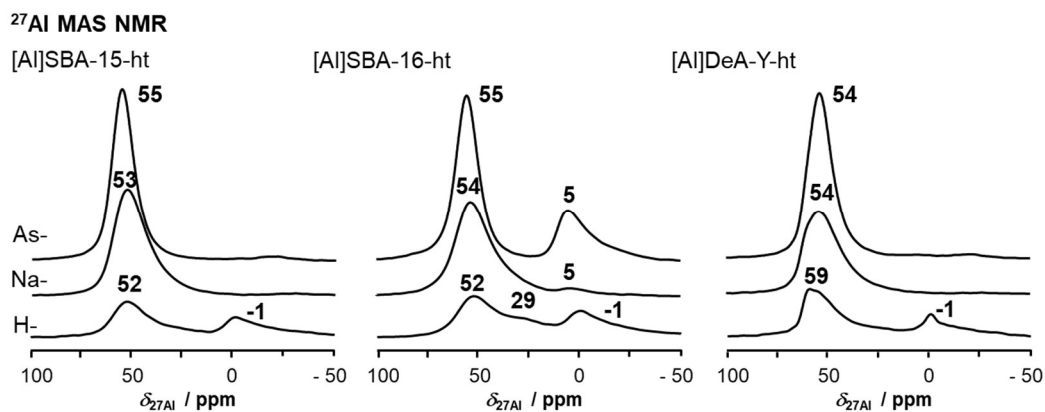


Figure 6.14 ^{27}Al MAS NMR spectra of the as-synthesized forms, Na-forms and H-forms (from top to bottom) of [Al]SBA-15-ht, [Al]SBA-16-ht and [Al]DeA-Y-ht samples (from left to right).

The ^{23}Na MAS NMR measurement shown in figure 6.15 disclose a strong difference of the state of Na^+ between pure NaAlO_2 and as-synthesized materials. This agrees well with previous findings on ^{27}Al nuclei, that all precursor was consumed. For untreated NaAlO_2 crystal, the ^{23}Na signal is broad and complicated due to the highly anisotropic structure. Although the hydration degree of NaAlO_2 significantly influences the quadrupolar coupling of ^{23}Na nuclei, qualitatively the shape of signal and chemical shifts of signal maxima agree well with literature.^[115] In agreement with this literature, three kinds of six-coordinate sodium atoms are assigned under the broad NaAlO_2 spectrum, with respective signal maxima at 9, 5 and -8 ppm. Among them, two species with signal maxima at 9 and -8 ppm have asymmetric octahedral structure and suffer from strong quadrupole coupling, while one species with isotropic chemical shift at 5 ppm is classified into an ideal octahedral structure. After transformation into as-[Al]SBA-15-ht, only one symmetric peak at -4 ppm is visible, which hints all Na atoms no longer belongs to the crystalline NaAlO_2 but are counter ions surrounded with water molecules in the aluminated porous material.

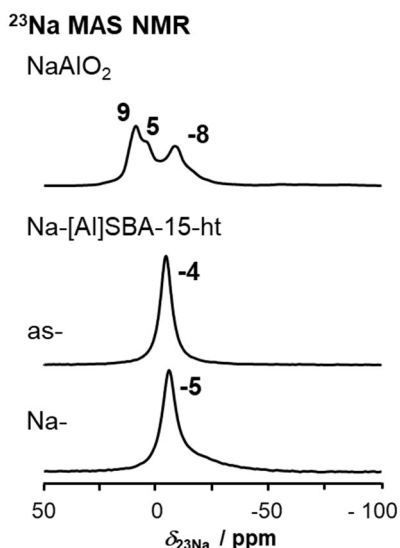


Figure 6.15 ^{23}Na MAS NMR spectra of the precursor NaAlO₂ and of fully hydrated Na-[Al]SBA-15-ht.

6.3.3 Transform into Na-form materials

The Na-form materials are obtained by calcination of as-synthesized materials. Changes in ^{29}Si MAS NMR and ^{29}Si CP MAS NMR spectra (figure 6.13) are analogous for all three kinds of samples, [Al]SBA-15-ht, [Al]SBA-16-ht and [Al]DeA-Y-ht. After calcination, signals at -86 ppm are absent. This confirms the vanishing of Si(OH)₃ groups. The numbers of other silanol groups (Si(OH)₂ and Si(OH)) also decline, as the observed intensities of signals at -92 and -101 ppm decreased strongly in ^{29}Si CP MAS NMR measurements. Similar change in silanol densities has been previously reported in AlCl₃ alumination process of SBA-15.^[48] These changes occur due to dehydroxylation reactions on the surface during the calcination treatment. On mesoporous materials, the Si(OH)(1Al) is the most probable groups attributed to the signal at -92 ppm, as we previously announced in the part on the as-synthesized form, considering the appearance of this signal in CP measurements and removal of all possible Si(OH)₂ groups in the calcination step. For Na-[Al]DeA-Y-ht, however, the signal intensity of -92 ppm is low in direct excitation measurements. It becomes much stronger after applying the cross-polarization technique. Therefore, it is concluded that the potential presence of Si(3Al) motifs can be ignored and that mainly Si(OH)₂ groups give rise to the signal at -92 ppm. Noteworthy, the signal intensity of the amorphous Q⁴ at -110 ppm also diminishes, whereas peak intensity of crystalline Q⁴ signal at -107 ppm increases. The reversal of signal intensities suggests that some of the amorphous silicon domains formed during NaAlO₂-solution treatment were reintroduced into the zeolite crystalline framework upon calcination.

6. The Alumination of Porous Silica with Sodium Aluminate

The ^{27}Al MAS NMR spectra (figure 6.14) reveal that, in all Na-form materials, most aluminum atoms are present in tetrahedral coordination. Only Na-[Al]SBA-16 contains trace amount of octahedral coordinated EFAl aluminum and shows thus a weak peak at 5 ppm. Comparing with the as-[Al]SBA-16-ht, the decrease of 5-ppm-signal intensity indicates a transformation of aluminum from octahedral to tetrahedral structure. This transformation happens on amorphous aluminosilicate only, due to its flexible aluminum coordination of aluminum with silica surface.^[116] However, formation of bulk AlO_6 cannot be excluded in Na-[Al]SBA-16-ht as the complex pore structure and low diffusion property inside pores may lead to agglomeration of aluminum species. Note that, Na-[Al]DeA-Y may have two kinds of framework aluminum as a shoulder is found on the left side of the main peak.

The 2D ^{27}Al MQMAS NMR spectra of three kinds of Na-form materials are shown in figure 6.16, left column. For SBAs, the broad signal manifold in the range of 40 to 70 ppm exhibits a signal maximum at around 60 ppm. Signal broadening is common in such disordered amorphous aluminosilicates, because of the large distribution of the isotropic chemical shifts and the quadrupolar coupling. We find that centers of signal are on the diagonal of the 2D spectra. This points out that most aluminum atoms are in a highly symmetric state. The shoulder of the signal implies another tetrahedral coordinated aluminum site, with a larger asymmetric quadrupolar shift. Therefore, this shoulder most probably associates with the flexibly coordinated aluminum. Only for Na-[Al]SBA-16-ht, a small signal centered at 0 ppm must be assigned to EFAL deposits of aluminium in octahedral coordination. In addition, a weak signal at ca. 30 ppm is found in the MQMAS spectrum of Na-[Al]SBA-16-ht. This signal was assigned to another kind of extra-framework aluminum in pentahedral coordination previously by MQMAS measurement on amorphous USY zeolite.^[116] On the other hand, Samoson et al. assigned a likewise signal to disturbed tetrahedral aluminum in a, thus, strong quadrupolar interaction.^[117] In contrast to the identical tetrahedral aluminum in Na-form of SBA materials, a slim signal at 60 ppm and a broad signal at a higher field are found in the MQMAS spectrum of Na-[Al]DeA-Y-ht (figure 6.16, bottom, left). Summarizing, the 2D measurements under higher magnetic field (11.7 T) definitely confirm the observations from the 1D ^{27}Al MAS NMR spectra. Especially they confirm that two kinds of tetrahedral coordinated aluminum exist in DeA-Y zeolite, in agreement with the previous finding.^[118]

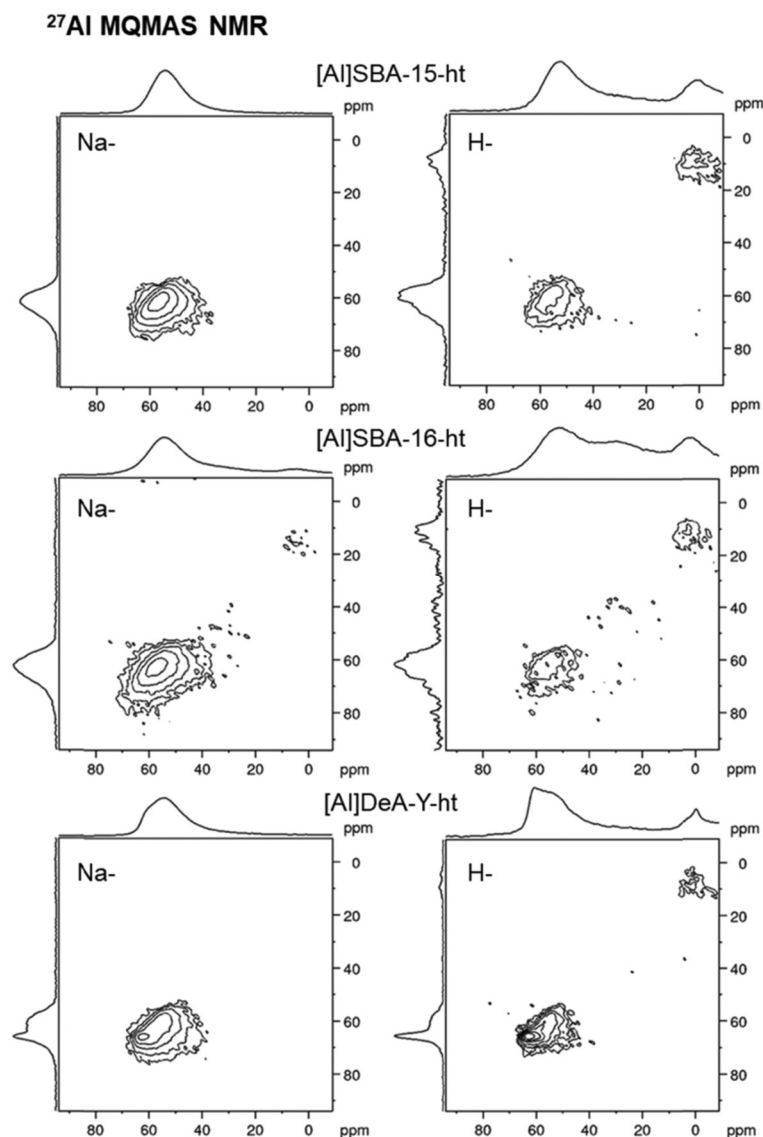


Figure 6.16 ^{27}Al MQMAS NMR spectra of Na- (left) and H-forms (right) of [Al]SBA-15-ht (top), [Al]SBA-16-ht (mid) and [Al]DeA-Y-ht (bottom).

In the left column of figure 6.17, $^1\text{H}\{^{27}\text{Al}\}$ TRAPDOR measurements unveil the aluminum neighboring hydroxyl groups in Na-form materials. When the Al-irradiation is stopped, all spectra show major signals at 1.8 ppm, which indicates the abundant presence of surface silanol groups, Si(OH). Weak shoulders at around 0 ppm, shown in Na-[Al]SBA-15-ht and Na-[Al]DeA-Y-ht samples are usually assigned to Al(OH) groups on the external surface or in large cages of the zeolite.^[75] The spectra collected under the irradiation of the aluminum nuclei show likewise only a signal at 1.8 ppm. However, it is obvious in the resulting difference spectra that signal intensity of silanols is lost. This means that some of the silanol groups are close to aluminum atoms. In other words, aluminum atoms are present in the silica surface and

6. The Alumination of Porous Silica with Sodium Aluminate

not just physically deposited on it. It is worth noting that no signal at 4 ppm presents in any TRAPDOR spectrum of Na-form materials. This indicates the absence of acidic Si(OH)Al groups on them and confirms that acid sites are, if present, completely exchanged with Na-cations.

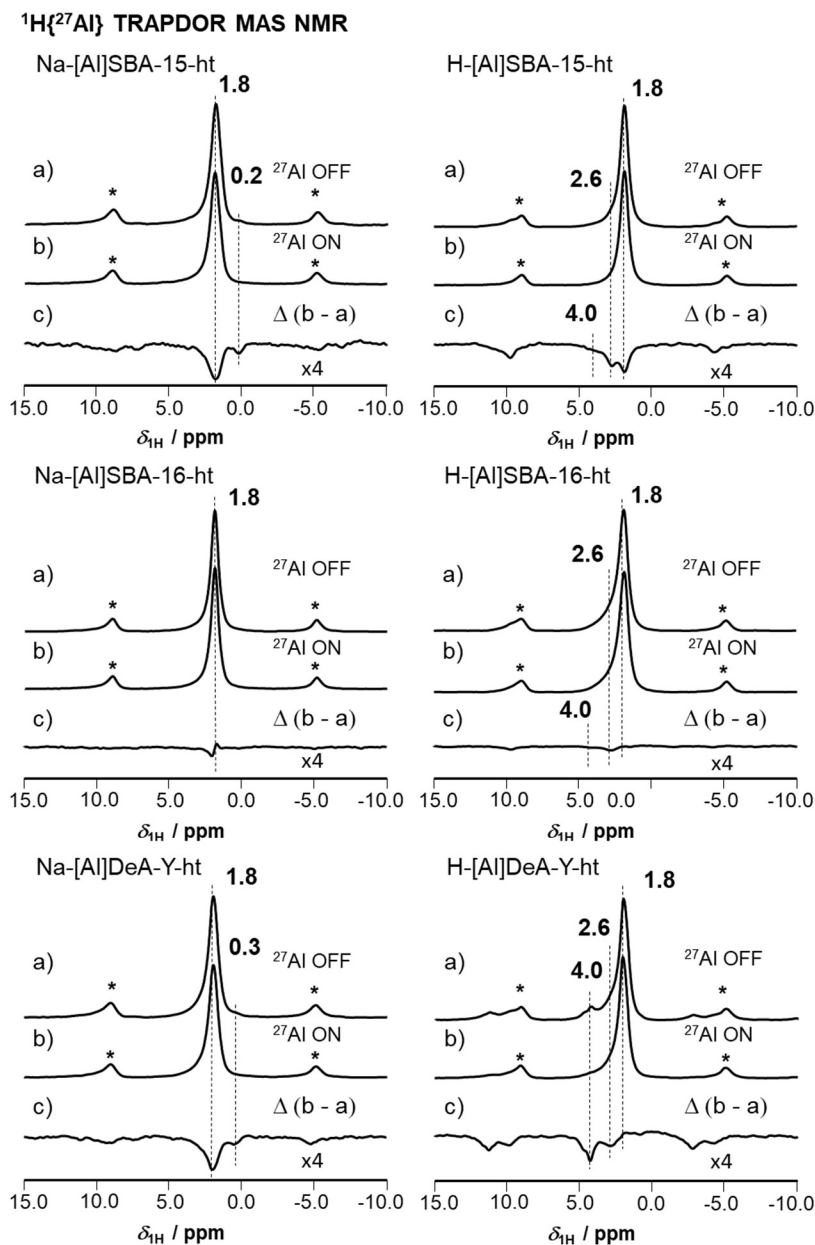


Figure 6.17 $^1\text{H}\{^{27}\text{Al}\}$ TRAPDOR MAS NMR spectra of Na- (left) and H-forms (right) of [Al]SBA-15-ht, [Al]SBA-16-ht and [Al]DeA-Y-ht samples. (a) ^1H MAS NMR spectra, (b) ^1H MAS NMR spectra with irradiation of ^{27}Al , (c) resulting difference spectra.

Last, we discuss the results from ^{23}Na MAS NMR spectroscopy (see figure 6.15). After the calcination step, the observed signal maximum at -5 ppm in hydrated [Al]SBA-15-ht is identical to the as-synthesized form. Thus, the majority of sodium does not change in its nature or coordination.

6.3.4 Transformation into H-form materials

After ion exchange using NH_4NO_3 and following calcination, the H-form materials were obtained from Na-form materials. The shape of signals in ^{29}Si MAS NMR and the ^{29}Si CP MAS NMR spectra of H-form materials are comparable to the ones observed previously for the Na-forms (figure 6.13). This shows that in the silicon bulk only few changes are taking place upon transformation into the H-form. In ^{29}Si MAS NMR spectra, intensities of signal at -92 ppm and at -101 ppm decrease, especially for the first signal. On the other hand, in ^{29}Si CP MAS NMR measurements these signals are as strong as in spectra of the Na-forms. Thus abundant $\text{Si}(\text{OH})_x$ ($x = 1, 2$) groups are still present on the H-form materials and dominate the CP spectra, whereas clearly changes in the bulk must be associated with changes in neighboring aluminum. Thus, the change of intensities in direct excitation measurement are due to removal of aluminum from the silicon bulk, taking place during in the ion exchange step. The density of hydroxyl groups increased as quantitative measurements shown in table 6.2 confirmed, which supports the in ^{29}Si CP MAS NMR measurements. The supplemental OH groups thus form on the defect sites generated during dealumination process.

In the ^{27}Al MAS NMR spectra of H-forms (figure 6.14, bottom) a main signal tetrahedral-aluminum (in the range of 50-60 ppm) is observed. In addition, all spectra show signal at around 0 ppm after removal of NH_3 by a calcination step. A hump at ca. 30 ppm is obvious for H-[Al]SBA-16-ht. The spectrum agrees with literature and the two signals at about 0 and 30 ppm are accordingly assigned to extra-framework five- and six-fold coordinated aluminum.^{[37],[87],[93],[116]} The newborn signals in ^{27}Al MAS NMR spectra again indicate the removal of aluminum from the bulk framework. It is then deposited in form of EFAL, which agrees with the findings from ^{29}Si and ^{29}Si CP MAS NMR measurements.

High field ^{27}Al MQMAS NMR measurements of H-form materials are shown in figure 6.16, right column. Two signals with centers at ca. 60 ppm and 0 ppm are again located on the diagonal. Like the MQMAS NMR spectra of Na-forms, a shoulder deviates from the diagonal. It is again assigned to aluminum in flexible coordination, as its asymmetric structure leads to an increase in the anisotropic quadrupolar interaction. Signals of pentahedral coordinated

6. The Alumination of Porous Silica with Sodium Aluminate

aluminum are only present in the spectrum of H-[Al]SBA-16-ht and found at around 30 ppm on the diagonal. Overall, all the ^{27}Al MQMAS NMR results are in agreement with our 1D ^{27}Al MAS NMR as well as with literature.^[87]

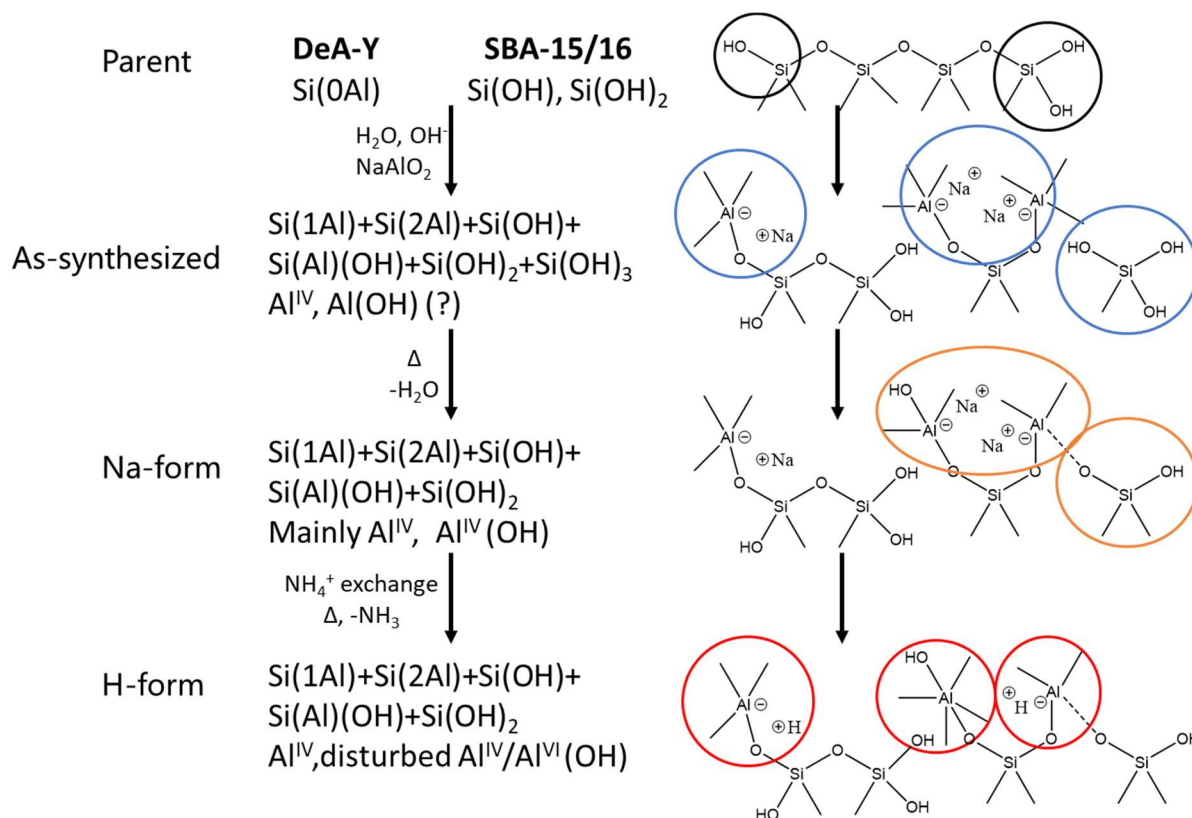
Information about hydroxyl groups on H-forms is again illustrated by applying $^1\text{H}\{^{27}\text{Al}\}$ TRAPDOR measurements (figure 6.17, right). As for Na-forms, the main signal at 1.8 ppm is assigned to the surface silanol Si(OH) groups. Signals at 0 ppm, contributing to external surface Al(OH) groups, vanish in H-forms and new signals of extra-framework Al(OH) appear at 2.6 ppm as result of aluminum extraction from the surface.^[75] In addition, the spectrum of H-[Al]DeA-Y shows a peak at around 4.0 ppm which is the typical chemical shift of acidic Si(OH)Al groups. Negative signals shown in difference spectra of $^1\text{H}\{^{27}\text{Al}\}$ TRAPDOR measurements indicate the influence of Al irradiation on the protons. For H-[Al]SBAs, some aluminum atoms are still close to the surface Si(OH), like in their Na-forms. This explains the negative peak at 1.8 ppm. A negative signal present at 2.6 ppm certifies the assignment to Al(OH) groups. A shoulder at around 4.0 ppm vaguely appears only in the difference spectra and is tentatively assigned to a low amount of acid sites.^{[89],[119]} This ambiguous signal hints to the fact that the acidity of H-form SBAs is weak. Spectrum recorded for H-[Al]DeA-Y shows a different picture. The intensity of signal at 1.8 ppm is nearly constant and no negative peak is found in the difference spectra. This shows that all the surface Si(OH) groups are far away from aluminum atoms in this acidic DeA-Y zeolite. Nevertheless, this is different from the TRAPDOR result of Na-[Al]DeA-Y, where a negative peak at 1.8 ppm is present in the difference spectrum. This implies a movement of aluminum atoms during preparing the H-form, away from Si(OH) groups. It agrees with the finding in ^{27}Al MAS NMR measurements. Signals at 2.6 and 4.1 ppm are almost completely reduced upon Al irradiation, because the associated hydroxyl groups are directly bond to bulk aluminum atoms.

6.3.5 Summary of Alumination Mechanism

Upon applying the MAS NMR technique on ^1H , ^{23}Na , ^{27}Al and ^{29}Si nuclei, a comprehensive understanding on the mechanism of modification with NaAlO_2 solution is gained. It is comprehensively visualized in scheme 6.2. For all parent materials, framework silicon (Si(0Al)) is the main component. Some Si(OH)_x (x = 1-2) groups are present on the surface, terminating it. During the treatment in alkaline NaAlO_2 solution, the silicon structure is partially dissolved, which leads to the formation of new silanol groups, Si(OH)_x (x = 1-3).

6. The Alumination of Porous Silica with Sodium Aluminate

Meanwhile, aluminum atoms are bound on the silica surface by the reaction between NaAlO_2 and surface silanol groups. It is noted that all aluminum atoms are in tetrahedral coordination. This supports the build-in of aluminum into the framework. After calcination, $\text{Si}(\text{OH})_3$ group vanish from spectra of Na-forms and almost all aluminum atoms are keeping their tetrahedral coordination. It is worth to note that the intensity of octahedral coordinated aluminum decreases in Na-[Al]SBA-16 materials. This indicates a flexible coordination of $\text{Si}(\text{OH})\text{Al}$ groups present. Finally, after ion exchange with NH_4NO_3 and calcination, the respective H-forms are received. Due to the removal of NH_3 in the calcination step, five- and six-coordinated aluminum is present. It reveals the framework aluminum is partially removed and deposits on the surface forming extra-framework aluminum (EFAL) species. From results of acid property (see the following section 6.4), we conclude that on aluminated mesoporous SBA-materials all Brønsted acid sites (BAS) are weak. This agrees well with the explanation that the BAS are in flexible coordination, in contrast to their state in crystalline material. In agreement with this, the acid strength of realuminated DeA-Y zeolite is as strong as the direct synthesized Y zeolite.



Scheme 6.2 Mechanism of sodium-aluminate alumination of siliceous porous DeA-Y, SBA-15, and SBA-16 materials. Chemical bonds linking only Al or Si on one side are either connected to silica framework or to hydroxyl groups.

6.4 Acid Properties of Aluminated Materials

To investigate the acid properties of aluminated H-form materials, three probe molecules, ammonia (NH_3), trimethylphosphine oxide (TMPO) and acetonitrile- d_3 (CD_3CN), were loaded on respective calcined samples. NH_3 loading was applied to determine the quantity of both Lewis and Brønsted acid sites at the same time.^[79] As shown in figure 6.18, ^1H MAS NMR measurement of parent and Na-forms show a main signal at 1.8 ppm that is again assigned to Si(OH) groups. In addition, for parent DeA-Y zeolite, a weak shoulder at around 4.0 ppm was assigned to traces of acidic Si(OH)Al groups. After NH_3 loading, for parent SBA-15 and SBA-16 as well as all Na-forms, no new signal appears in their ^1H MAS NMR spectra which indicates weak interaction of surface sites on these materials with this basic probe molecule. In other words, neither Lewis nor Brønsted acid sites in reasonable quantities are detectable on these materials. This is in good agreement with the previous finding that Na^+ ions on the zeolite scarcely interact with NH_3 .^[101] Whereas, loading of NH_3 generates a strong signal at 6.5 ppm in the ^1H MAS NMR spectrum of parent DeA-Y. This indicates the formation of NH_4^+ ions and hints at the presence of strong Brønsted acid sites (BAS) on it. Still, the quantity of BAS remains low, below 0.02 mmol/g.

Like parents and Na-forms, all three ^1H MAS NMR spectra of calcined H-form samples contain a main signal at 1.8 ppm of Si(OH) groups. A shoulder at 4.0 ppm of Si(OH)Al groups appears only in the spectrum of H-[Al]DeA-Y-ht (figure 6.18, bottom). The spectra and assignments are identical, as the result of $^1\text{H}\{^{27}\text{Al}\}$ TRAPDOR measurements (section 6.3.4). After adsorbing ammonia molecules from gas phase, new signals of NH_4^+ ions appear at 6.5 ppm for all H-forms. This reflects the presence of strong BAS on the materials. Except for the clear and sharp signal at 6.5 ppm, a broad hump raises up from around 5.0 to 0 ppm. Since the weak bound, physisorbed NH_3 should be removed during the evacuation at 453 K, the broad signal must be assigned to species as result of a strong interaction between Lewis acid sites (LAS) and ammonia.^[48] Results from quantification of ^1H MAS NMR spectra are shown in table 6.5. With the increase of aluminum content on SBA-15, more BAS and LAS appear on H-[Al]SBA-15 materials. However, the acid site densities of all H-forms remain low compared with their total aluminum contents (table 6.5). This is again in good agreement with the $^1\text{H}\{^{27}\text{Al}\}$ TRAPDOR measurements, as no strong signal appeared at ca. 4.0 ppm there. The reason of the low content of acid sites is the transformation of tetrahedral framework aluminum atoms which gives rise to acidity in Si(OH)Al groups, into five- or six-coordinated species during the calcination of NH_3 -forms. This was previously shown in the ^{27}Al MAS and ^{27}Al

6. The Alumination of Porous Silica with Sodium Aluminate

MQMAS NMR spectra in section 6.3. Furthermore, taking it into account that the formation of H-forms is from burning of NH₃-forms, the low acid densities of these materials from NH₃ loading results indicates the coordination type of aluminum atoms is irreversibly changed. It is worth noting that collapse of the SBAs' micropores could make some bulk aluminum atoms untouchable by probe molecules like NH₃, which depends on access from the pores respectively the surface of the catalysts.

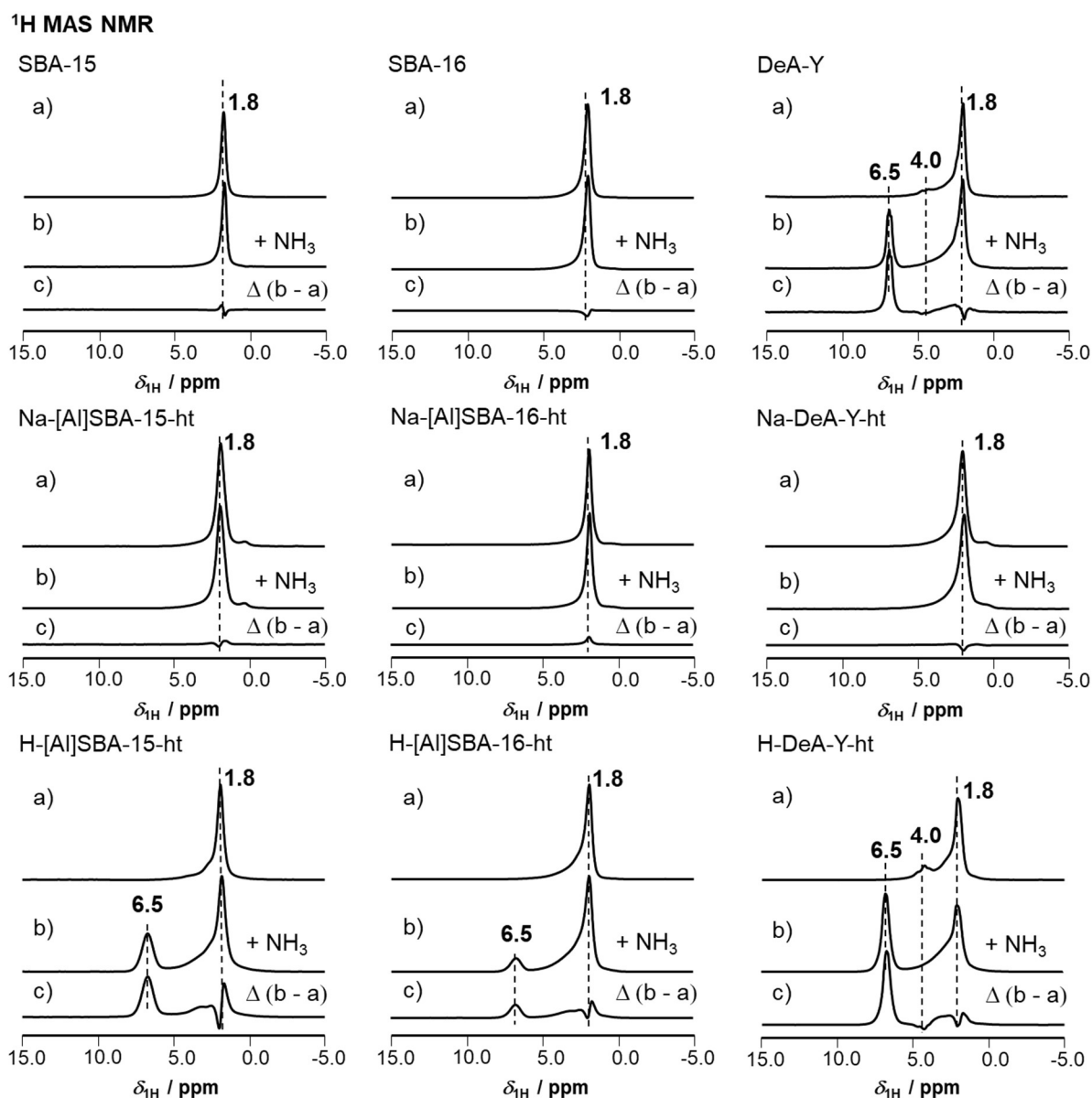


Figure 6.18 ¹H MAS NMR spectra of activated (a), NH₃ loaded (b) and resulting difference spectra of SBA-15 (left), SBA-16 (middle) and DeA-Y(right) materials in their respective parent forms, Na-forms and H-forms (from top to bottom).

Table 6.5 Aluminum content and quantification of acid sites from NH₃ and TMPO adsorption measurements

Materials	Al content [mmol/g] ^{a)}	NH ₃		TMPO	
		BAS	LAS	BAS	LAS
		[mmol/g]	[mmol/g]	[%]	[%]
H-SBA-15-low	0.5	0.05	0.08	57	43
H-SBA-15-high	1.0	0.10	0.18	62	38
H-SBA-15-ht	1.1	0.12	0.19	61	39
H-[Al]SBA-16-ht	1.1	0.03	0.08	43	57
H-[Al]DeAY-ht	0.7	0.12	0.09	55	45

a) From ICP-OES experiments, accuracy $\pm 10\%$.

Loading of trimethylphosphine oxide (TMPO) combined with ³¹P MAS NMR measurement is a typical method for elucidating different types of BAS and LAS simultaneously.^{[120],[121]} For parent materials, major signals are located at 40-45 ppm and assigned to bulk physisorbed TMPO, as shown in figure 6.19. Different from other parent materials, a hump at around 65 ppm present in the spectrum of parent DeA-Y zeolite is found, due to the remaining acidity on it. Individual peaks were disclosed by applying Gaussian/Lorentzian functions and upon using the chemical shifts from literature.^{[121],[122]} A weak peak at 30 ppm is assigned to isolated physisorbed TMPO molecules. This tiny signal indicates small pores or cavities in parent SBA-16 are present. Four peaks could be separated in the spectrum of DeA-Y. Two strong signals at high field were both due to bulk TMPO with different cluster size, while signals of TMPO interacting with LAS and BAS are found at 64 and 70 ppm (table 6.6), respectively. The presence of acid sites on parent DeA-Y is in line with the result from NH₃ loading.

6. The Alumination of Porous Silica with Sodium Aluminate

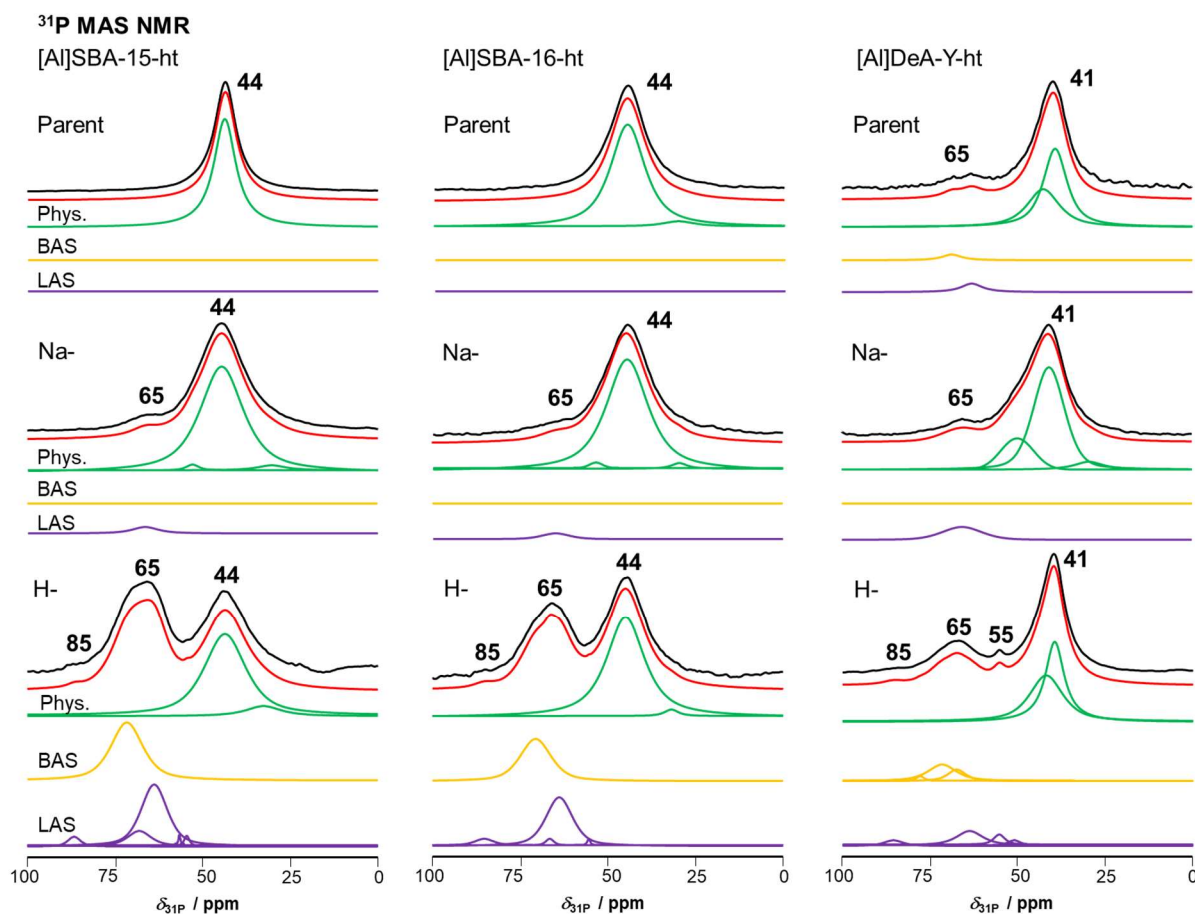


Figure 6.19 ^{31}P MAS NMR spectra of TMPO loading on [Al]SBA-15-ht, [Al]SBA-16-ht and [Al]DeA-Y-ht samples (from left to right) in their respective parent, Na- and H-forms. Spectra combine (from top to bottom) original spectra (black), sum of simulated spectra (red), and simulated individual peaks of physisorbed TMPO (green), TMPO adsorbed on Brønsted acid sites (yellow) and on Lewis acid sites (purple).

Table 6.6 ^{31}P MAS NMR shifts and assignments of TMPO species

Chemical shift [ppm]	TMPO Species	References
30	Isolated, physisorbed	[121]
40 to 45	Bulk, physisorbed	[75],[121],[122]
48	TMPO on Na^+	[123],[124]
50 to 65	TMPO on LAS	[125-128]
65 to 80	TMPO on BAS	[79],[121]
80 to 90	TMPO on LAS+BAS	[121],[122]

Similar like spectra of parent materials, signals of bulk TMPO dominate ^{31}P MAS NMR spectra of Na-forms. A signal at 48 ppm cannot be ignored on Na-[Al]DeA-Y-ht. In previous,

6. The Alumination of Porous Silica with Sodium Aluminate

a study assigned it to physisorbed TMPO on DeA-Y zeolite in presence of Na⁺ cations.^[123] Others assigned it to TMPO interacting with Na cations on Y zeolite.^[124] Therefore, we likewise explain this signal with TMPO interacting with Na⁺. Considering the Lewis acidity of Na⁺ is weak or negligible, the signal is finally classified to being bulk physisorbed TMPO. A weak shoulder at 65 ppm is found on all spectra of Na-forms. However, instead of two individual peaks in parent DeA-Y, only one peak is enough for deconvolution. Assignment of this signal is controversial. In some literature, authors assign it as TMPO interacting with BAS on zeolite H-Y or [Al]MCM-41 without comparing with their corresponding Na-form materials.^{[123],[125],[126]} In contrast, a recent research determined the 65-ppm signal to TMPO binds with Lewis-acidic tri-coordinated aluminum on the framework of ZSM-5.^[127] In our case, the NH₃ loading has confirmed a full exchange of Na cations. No BAS are present in Na-forms. Furthermore, in the discussion of alumination mechanism, ²⁷Al MAS NMR spectra have suggested a type of flexible coordination on Na-form materials. Thus, this signal at 65 ppm in our Na-forms must be assigned to TMPO on the newly detected Lewis acid species.

Both BAS and LAS form in H-forms as result of a NH₃ loading. Since aluminum removal and transform as well as formation of new species during the preparation of H-forms could be verified by MAS NMR measurements, it is not surprising that chemical shifts, δ_{31P} , of adsorbed TMPO species are close to each other and lead to complex deconvolution figures and peak manifolds.^{[123],[125]} As shown in figure 6.19, bottom, up to 7-9 peaks have been classified in spectra of H-[Al]SBA materials and H-[Al]DeA-Y-ht zeolites. Some of the signals are weak and assigned to similar sites as the nearby main peak in order to avoid overinterpretation. Physisorbed TMPO species involve the same chemical shifts as in parent and Na-forms. It is worth noting that no peak at 48 ppm appears in the spectra of H-[Al]DeA-Y, which confirms a full ion-exchange into the H-form. Chemical shifts of peaks of TMPO on BAS are usually in a range of 65-80 ppm, while chemical shifts of peaks of TMPO on LAS are lower and in a range of 50-65 ppm.^{[79],[121],[124]} Although chemical shifts of TMPO on BAS are normally higher than TMPO on LAS, peaks at 84-88 ppm were assigned to interaction with LAS as there is little possibility of strong BAS on zeolite.^[128] However, various advanced 2D MAS NMR spectra, accompanied by DFT calculations, suggest that the super-acidic sites are formed by tri-coordinated aluminum close to BAS.^[127] Considering, all assignments of this low-field peak associates with LAS in literature, we finally assigned it as Lewis acid sites. Therefore, if only the clearly visible peaks were considered, one BAS at 69 ppm and two LAS 65 and 85 ppm could be clearly identified in high-temperature modified H-form SBA materials. Nevertheless,

6. The Aluminations of Porous Silica with Sodium Aluminate

crystalline H-[Al]DeA-Y-ht contains three types of BAS at 67, 71 and 78 ppm and at least three types of LAS at 55, 65, 85 ppm. The different types of BAS are explained by the different location of the sites, in mesopores, in supercages and in sodalite cages.

Comparison of BAS and LAS densities from TMPO loading is challenging as the high loading of TMPO donates a strong signal of physisorbed species. It is known that more than one TMPO molecule can be protonated by a BAS and therefore causes an overestimation of BAS densities.^[128] Still the evaluation of acid site density from TMPO loading still present a reasonable result comparing with NH₃ loading (table 6.5).

Except acid density and types of acid sites, information about acid site strength of the BAS is also a crucial parameter for solid acid catalysts. In order to achieve this goal, acetonitrile-d₃ (CD₃CN) was loaded on different H-form materials and the corresponding ¹H MAS NMR spectra are shown in figure 6.20. For all materials, a broad signal in range of 1.5 to 5.0 ppm appears at the expense of Si(OH) groups at 1.8 ppm. This signal is eliminated after evacuation for 12 h by removing physisorbed species on the surface, which reveals the weak acidity of Si(OH). Therefore, we can conclude the flexible coordinated BAS are too weak to irreversibly protonate weak base (CD₃CN), although acidity present when they interact with strong base like NH₃. In contrast, for H-[Al]DeA-Y-ht, a peak at 11.5 ppm after CD₃CN loading appears. It remains after vacuum treatment with only a slight shift to 10.9 ppm. This indicates strong BAS on the microporous material, as they are able to withhold the weak base. The thus determined adsorption-induced chemical shift ($\Delta\delta_{1H}$) of this site is 6.8 ppm, which is in line with the reported value of $\Delta\delta_{1H} = 7.0$ ppm derived from a material with similar Si/Al ratio.^[77] It is worth noting that this signal is likewise presents on parent DeA-Y after CD₃CN loading. However, the intensity on the parent is only 17% of on the aluminated DeA-Y. Thus, it is confirmed that the BAS on microporous DeA-Y zeolite are really formed upon aluminations with NaAlO₂ solution and that the new sites are of same strength as the sites in the direct synthesized zeolites.

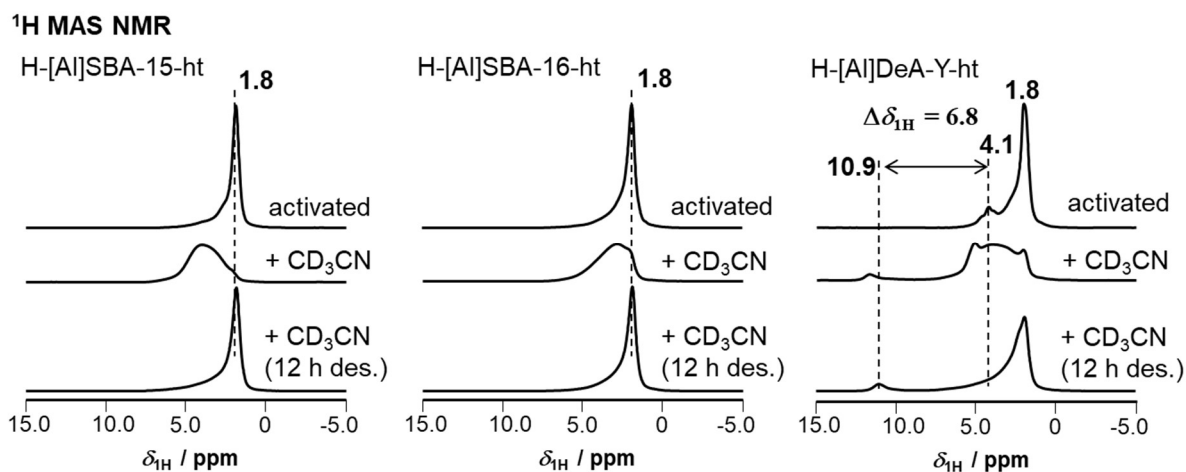


Figure 6.20 ^1H MAS NMR spectra of activated and CD_3CN loaded H-[Al]SBA-15-ht, H-[Al]SBA-16-ht and H-[Al]DeA-Y-ht samples.

6.5 Conclusions

In this work, with the help of various solid-state NMR techniques, we demonstrate how a meaningful post aluminations method for preparing an/a ion exchanger and solid acid catalyst on micro- and mesoporous silica works. The introduced aluminum content can be optimized by applying different quantities of NaAlO_2 and/or varying the reaction temperatures. Most aluminum binds on the surface of SBA-15, whereas the complex 3D pore system of SBA-16 hinders the diffusion of aluminum leading to some deposits. In addition, the final Si/Al ratio is limited by the low density of initial binding sites, Si(OH) groups. XRD patterns as well as SEM and TEM images confirm an intact mesopore system in SBA-15 and SBA-16 materials during the whole modification process. In addition, X-ray diffraction verified a pure FAU-type phase of parent and aluminated DeA-Y zeolites. N_2 physisorption measurements disclose the elimination of the micropore structures, initially presenting on SBA materials, with diminishing BET surface area and mesopore volume on all materials upon aluminations. The more aluminum build in, the smaller the BET surface area. However, the average mesopore diameters are still comparable, indicating that mesopores are unaffected by the modification method.

The mechanism of the modification is unveiled by MAS NMR measurements. Partial dissolution of all materials and formation of $\text{Si}(\text{OH})_x$ ($x = 1-3$) groups were verified. They are explained by a partial dissolution of the silica structure by the treatment with alkaline NaAlO_2 solution. This corroborates the usefulness of higher reaction temperatures for building in more aluminum during aqueous treatment. Tetrahedral coordinated aluminum is the main species in

6. The Aluminations of Porous Silica with Sodium Aluminate

as-synthesized and Na-forms, no matter what kinds of the aluminum containing species are present. It is noted that Na-forms are useful as ion exchangers and exchange can be performed without destroying the framework. On H-forms, especially for H-[Al]SBA-16, extra-framework aluminum irreversibly forms from the tetrahedral coordinated framework aluminum during the removal of NH_3 . Therefore, it is not surprising that less than 25% of Na^+ , was finally transformed into BAS.

The acid sites were characterized by loading with basic probe molecules like NH_3 , TMPO, and CD_3CN . Quantitative information on acid sites is acquired from quantitative NH_3 loadings. It shows that only H-forms and to some extent parent DeA-Y zeolite contain BAS and LAS. Up to 0.12 mmol/g BAS and 0.19 mmol/g LAS form in preparing H-forms. The difference of acidity between parent DeA-Y and its isostructural Na-form indicates BAS are removed in NaAlO_2 solution. TMPO probe detects the tri-fold coordinated framework aluminum sites with the ^{31}P signal at 65 ppm in Na-forms. However, this kind of LAS is not detectable with NH_3 . TMPO loading reveals the presence of 1 BAS and 2 LAS on H-[Al]SBA material, while 3 BAS and 3 LAS can be distinguished on H-[Al]DeA-Y-ht. A larger variety of BAS and LAS in DeA-Y could be caused by its various (micro- and secondary meso-) pore structures. The BAS density of H-[Al]SBA-16-ht is only 0.03 mmol/g, which is only 1/4 of the BAS quantity in H-[Al]SBA-15-ht even though both materials are of same Si/Al ratios. Thus, not only aluminum quantity but also a suitable site for aluminium introduction is crucial for generating large quantities of BAS. The weak base CD_3CN was used for determining the acid-site strength of BAS. Acid sites on aluminated SBAs are weak and usually not able to protonate CD_3CN irreversibly. Only the H-[Al]DeA-Y-ht owns strong BAS and their acid-site strength is comparable to directly synthesized Y zeolites. We can conclude that aluminations by NaAlO_2 solution treatment is a useful method for preparing ion exchangers and acid catalysts, especially for materials with simple and well-accessible pores like SBA-15.

7. Binding Sites and Strength of Water and Methanol in Micro- and Mesoporous Materials

7.1 Introduction

Adsorption and desorption of reactants are significant aspects in the catalysis process. Furthermore, the formed surface species are often crucial for the mechanism of the reaction that occurs on a solid catalyst. Therefore, the understanding of the adsorption behavior is essential for learning the reaction pathway and mechanism of the catalytic process, especially for heterogeneous catalysis. Water and methanol are representative substances participating in many reactions of industrial interest. Firstly, water is widely known as a polar solvent, a reactant, and a co-product in diverse chemical reactions.^[129-133] It is almost always present if bio-based feedstock is used. For example, in the alcohol dehydration reaction, even a small amount of water on the surface of catalysts can stabilize the adsorbed alcohol further and, therefore, reduce the dehydration rate.^[129] The reaction of cyclohexanol dehydration occurs on different routes, as the presence of water changes the active acid sites from bridge OH groups to hydronium ions.^[132] The formation of hydronium ions in micropores of zeolites can prevent the adsorption of reactant, resulting in a decrease of reaction rates.^[134] Besides, the selectivity of reactions and the stability of catalysts are also influenced by water.^{[133],[135],[136]} Thus, water present as co-feed or co-product does significantly influence chemical reactions through its formed surface species. Secondly, methanol, as one of the main feedstocks in C1 chemistry, is also an essential and typical adsorbate in heterogeneous catalysis and a good model for longer chain alcohols like ethanol. There are many routes in development that use methanol as platform chemical for the chemical industry, usually from CO₂-neutral sources. Methanol could for example be generated through methane oxidation or CO₂ hydrogenation.^{[137],[138]} Subsequently, methanol is the feedstock to produce value-added chemicals and fuels, through the methanol to olefins (MTO) or other similar processes.^[139] Also during these reactions, water generally occurs as a solvent or co-products, which may compete with the adsorption of methanol. Therefore, it is meaningful to investigate the adsorption properties of water compared with methanol on typical catalysts, such as porous materials.

Solid-state NMR is a valuable technique for studying the states and natures of molecules adsorbed on solid surfaces. In gas phase, the ¹H chemical shift of pure water molecule is at 0.31 ppm, while the chemical shift of liquid water is at 4.8 ppm.^{[140],[141]} The increase of the chemical shift value is due to the formation of H-bond between water molecules. As the

7. Binding Sites and Strength of Water and Methanol in Micro- and Mesoporous Materials

adsorbate, water adsorbed on Na-zeolite provides a chemical shift at 3.5 ppm.^[142] When the counter ion changes into H⁺, chemical shift of protonated water is at around 9 ppm in the fully hydrated zeolite.^[143] This is happening as the proton is able to fast exchange with the protons of the water, or in other words the signals of protons involved average due to fast exchange. Similar to water, chemical shifts of hydroxyl groups in methanol molecules were reported at 0.02 ppm in gaseous state, at 4.7 ppm in liquid state, and at 3.6 ppm adsorbed on Na⁺ cations.^{[142],[144],[145]} Although various solid-state NMR researches studied the adsorption of water or methanol on porous materials, a direct comparison of adsorption behavior and especially the adsorption sites of the molecules between isostructural materials with different pore sizes is still absent.

Another important adsorption property is the heat of adsorption or desorption, which quantitatively reflects the strength of surface interaction with adsorbate molecules. Experimental methods, such as temperature programmed desorption, isothermal adsorption, etc. are commonly used in this investigation. The heat of evaporation for liquid water and methanol are 41 kJ/mol and 37 kJ/mol, respectively.^{[146],[147]} When water and methanol are adsorbed on zeolites, adsorption heats are in a range of 20 to 80 kJ/mol.^[148-151] Normally, the adsorption heats of water and methanol on siliceous material are low, for example, the heat of water desorption from Silicalite, a MFI-type zeolite, is reported to be 20 kJ/mol.^[150] In contrast, the heat of water desorption from aluminum-containing MFI zeolites reaches up to 80 kJ/mol.^[148] However, the high desorption heat is always determined at a low loading of adsorbates. Thus, it reflects adsorption heat on the most active surface sites. When more molecules are adsorbed on one site, the adsorption or desorption heat is varied by the influence of intermolecular interaction.

In this work, we compared the adsorption properties of water and methanol on two series of materials, microporous MFI-type zeolites and mesoporous SBA-15 materials. The reason for choosing MFI zeolite is its wide application in bio-transformations. This zeolite can be synthesized in a wide range of aluminum contents and does not need to be aluminated before application. In order to get a comprehensive understanding of the influence of adsorption sites, each series of materials contains their siliceous form, Na-form and H-form. Adsorption sites are revealed with the help of solid-state NMR measurements, and desorption heats are determined by thermogravimetric analysis and differential scanning calorimetry (TGA-DSC) measurements. In addition, each material was studied 1) in their saturation state to clarify the adsorption properties of water or methanol clusters, 2) after desorption at 373 K to investigate

adsorption properties of remaining molecules that normally directly bond with adsorption sites, and 3) after desorption at 723 K to verify the intact sample without coverage of adsorbates.

7.2 Physicochemical Characterization

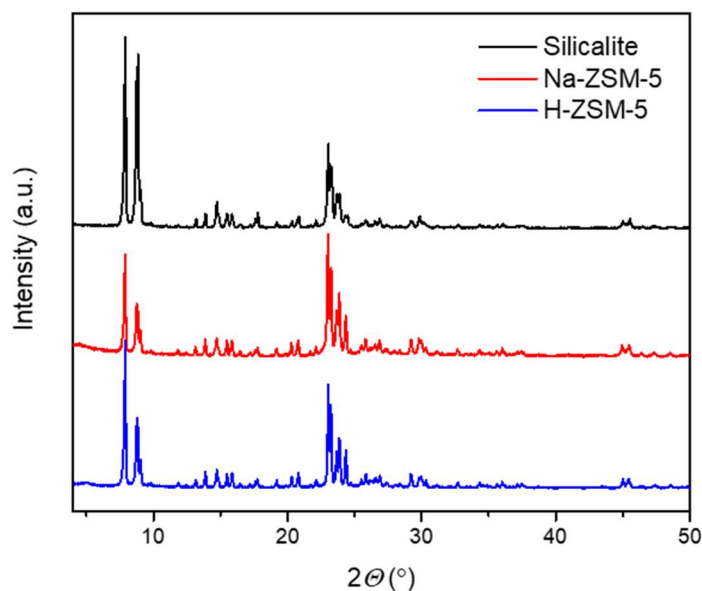
The chemical composition data measured by ICP-OES and the N₂ physisorption results of the materials in this study are summarized in table 7.1. Siliceous materials, *i.e.* Silicalite and SBA-15, contain only trace aluminum and sodium. For aluminum-containing materials, the isostructural Na- and H-forms show identical amounts of aluminum, whereas only a negligible Na content is found in the H-form materials. Therefore, the ion exchange is complete and happened without removal of aluminum. The BET surface areas of MFI-type zeolites are comparable and in the range of 345 to 375 m²/g. No more than 0.1 mL/g of mesopore volumes are found in these materials, which are typical values for the highly crystalline MFI-type materials.^{[72],[101]} Alumination of SBA-15 was performed under condition 2 (see section 5.1.5). Upon modification of SBA-15, surface area decreased from 870 to 522 m²/g and finally to 442 m²/g for H-[Al]SBA-15. Meanwhile, initially present micropores almost vanished and the mesopore volume was reduced from 0.93 to 0.72 mL/g, along with a decrease in mesopore diameter from 7.1 nm to 6.7 nm. These changes revealed by N₂ physisorption measurements agree well with the discussion in chapter 5. It should be noted that the physicochemical properties of SBA-15 materials are comparable, but not the same as the results discussed in chapter 5 due to the parent SBA-15s are not from the same batch.

Table 7.1 Physicochemical properties of the materials in this study

Material	Si/Al ratio ^{a)}	Al content [mmol/g] ^{a)}	Na content [mmol/g] ^{a)}	Surface area [m ² /g]	V _{micro} [mL/g]	V _{meso} [mL/g]	mesopore diameter [nm] ^{b)}
Silicalite	>800	<0.01	<0.01	350	0.12	0.10	-
Na-ZSM-5	24	0.60	0.60	345	0.12	0.06	-
H-ZSM-5	24	0.60	<0.01	372	0.13	0.07	-
SBA-15	>1600	<0.01	<0.01	870	0.14	0.93	7.1
Na-[Al]SBA-15	12	1.11	0.86	522	0.05	0.75	6.7
H-[Al]SBA-15	12	1.15	<0.01	442	0.03	0.72	6.8

a) Determined by ICP-OES; accuracy $\pm 10\%$; b) From N₂ physisorption, adsorption branch.

X-ray diffraction (XRD) measurements verify the phase purity of MFI-type zeolites (figure 7.1) and SBA-15 materials (figure 7.2). Only diffraction peaks identified as a typical MFI structure can be recognized, excluding the existence of other competing phases. Small-angle X-ray scattering patterns of SBA-15 materials show sharp peaks at around 0.95° and two weak humps at 1.60-1.85° indicating their mesoporous structure.

**Figure 7.1** XRD patterns of MFI-type zeolites.

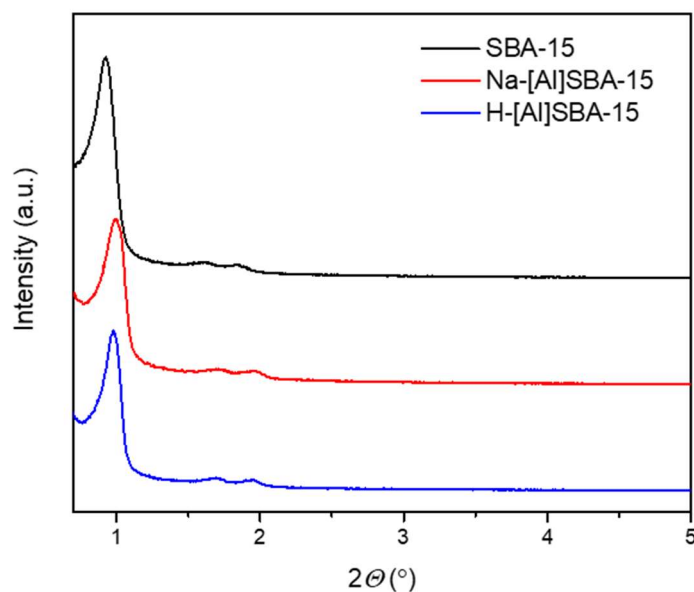


Figure 7.2 XRD patterns of parent SBA-15 and aluminated SBA-15 materials.

The ^{27}Al MAS NMR spectra of all materials under study are shown in figure 7.3. Aluminum signals remain absent for siliceous materials, which agrees well with the results from ICP-OES measurements. For aluminum-containing materials, the major peaks are found at around 55 ppm. This peak can be assigned to tetrahedral aluminum (Al^{IV}). It is worth noting that these Al^{IV} peaks in [Al]SBA-15 materials are much broader than for MFI zeolites due to their amorphous structures, causing the large distribution of the isotropic chemical shifts and an increase of quadrupolar coupling constant. A weak signal is present at 0 ppm for H-ZSM-5 due to the presence octahedrally coordinated aluminum (Al^{VI}). This aluminum is considered to be located outside of the framework, and thus called “extra-framework aluminum”. For H-[Al]SBA-15, this Al^{VI} signal is more prominent and the pentahedrally coordinated aluminum (Al^{V}) is also visible as a hump at around 30 ppm. The presence of extra-framework aluminum (Al^{V} and Al^{VI} aluminum) implies a re-distribution of aluminum atoms during the removal of NH_3 , as discussed in chapter 6. In summary, we found that all materials possess pure structures and aluminum sites with the expected properties.

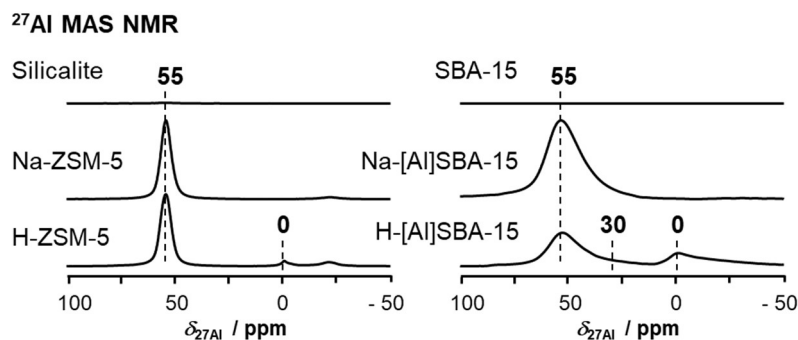
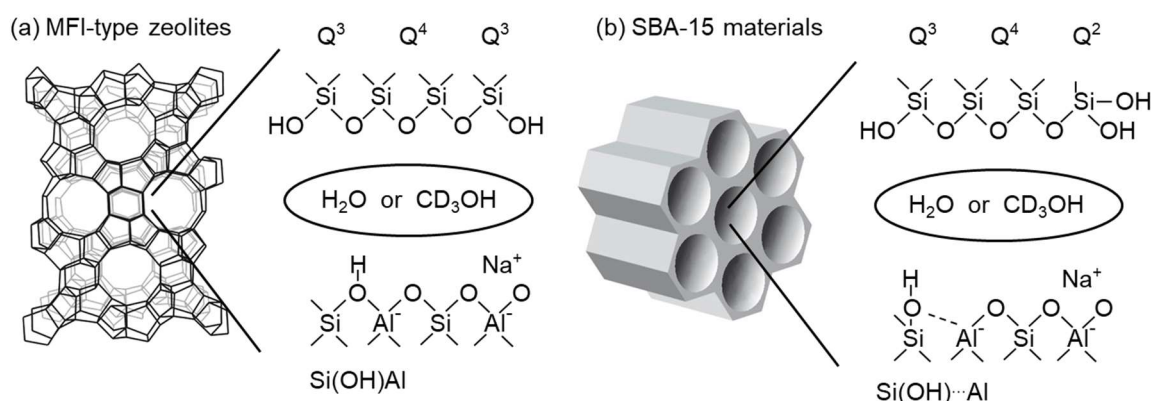


Figure 7.3 ²⁷Al MAS NMR spectra of MFI-type zeolites (left) and SBA-15 materials (right) in their siliceous forms (top), Na-forms (middle) and H-forms (bottom).

7.3 Adsorption Sites for Water and Methanol

The surface groups in the siliceous and aluminum-containing samples are summarized in Scheme 7.1, which are the potential sites for water and methanol adsorption. As mentioned in chapter 5, siliceous materials normally have the Q⁴-type framework silicon and some Q³-type terminal Si(OH) groups. As for amorphous SBA-15 materials, the geminal Q²-type Si(OH)₂ groups additionally exist. For the aluminum-containing materials, aluminum is strictly fitted into the crystalline MFI frameworks. However, in the case of [Al]SBA-15 materials, aluminum could only flexibly coordinate with silanol groups in mesopores. The different coordination styles influence the acid properties on H-form materials and may also affect the adsorption behavior of water and methanol.



Scheme 7.1 Surface structure of siliceous (top) and aluminum containing forms (bottom) of MFI zeolites (a) and SBA-15 materials (b).

7. Binding Sites and Strength of Water and Methanol in Micro- and Mesoporous Materials

The ^{29}Si CP MAS NMR experiment is suitable for investigating water or methanol adsorption on siliceous materials, because the signal of ^{29}Si nucleus can be selectively strengthened by the nearby ^1H nucleus via ^1H - ^{29}Si cross polarization. The involved ^1H atoms could be from either the $\text{Si}(\text{OH})_x$ groups or the strongly adsorbed adsorbates, like H_2O .

For Na-form materials, framework tetrahedral aluminum atoms bring negative charges, which can be compensated by the presence of counter charges, *e.g.* sodium cations. Spin quantum numbers of both ^{23}Na and ^{27}Al nuclei are larger than $1/2$, determining the dominance of quadrupole interactions in their MAS NMR spectra. The isotropic chemical shift of a quadrupolar nucleus is influenced by the coordination number and the strength of quadrupole interaction, described by quadrupolar coupling constant C_q , is influenced by the electric field around the quadrupolar nucleus.^[152] Thus, the adsorption of molecules on a quadrupolar nucleus can be reflected by the simultaneous change of the isotropic shift and C_q value.

Normally, the major adsorption sites of H-form materials are their Brønsted acid sites (BAS), as the catalytic reactions occur on these sites. As mentioned in chapter 5, the acid-site strength is affected by the aluminum position. BAS in crystalline zeolites, such as DeA-Y, originate from rigid $\text{Si}(\text{OH})\text{-Al}$ bonds showing a strong acidity. While, BAS in H-[Al]SBA-15 derive from a flexible binding between silanol groups and aluminum ($\text{Si}(\text{OH})\text{---Al}$), showing a weak acidity. Both strong and weak BAS can be quantitatively detected by ammonia loading and then determining the formed NH_4^+ cations by quantitative ^1H MAS NMR.

In the next sections, the above-mentioned NMR tools are applied to investigate the potential sites for water and methanol adsorption on different materials.

7.3.1 Adsorption Sites on Siliceous Materials

As shown in figure 7.4, in ^{29}Si CP MAS NMR spectra, signal intensities change a lot when the dehydrated samples are saturated with water or methanol. For Silicalite, two signals are at -103 and -113 ppm, which can be assigned to Q^3 type $\text{Si}(\text{OH})$ groups and Q^4 -type framework silicon atoms, respectively. Water saturation leads to a decrease of the Q^3 signal, whereas the Q^4 signal is constant. A similar decline of the Q^3 -signal intensity has been reported by Wang et al. on hydrated H-ZSM-5 zeolite, although bridge $\text{Si}(\text{OH})\text{Al}$ groups are the major sites on their sample.^[143] This weakness of Q^3 signal indicates a weaker polarization transfer between ^1H and ^{29}Si nuclei and represents an increase of O-H distance of the $\text{Si}(\text{OH})$ groups

after water loading. Therefore, we can conclude that water is adsorbed on Si(OH) groups in Silicalite. In addition, this diminishing signal also hints the H atoms on water molecules do not contribute to the polarization transfer, which may be due to the long distance between water and Si atoms or the high mobility of water molecules. On the other hand, in the case of methanol saturated Silicalite, not only Q³- but also Q⁴-type silicon show an intense decrease of signal intensities. Thus, we assume a stronger interaction of Si(OH) groups with methanol than with water.

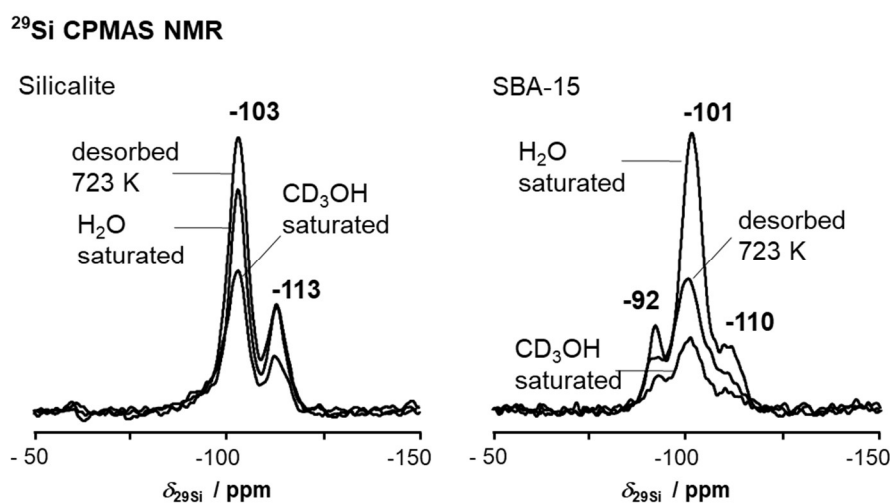


Figure 7.4 ^{29}Si CP MAS NMR spectra of Silicalite (left) and SBA-15 (right) after desorption at 723 K and after saturation with water (H_2O) or methanol (CD_3OH).

The ^{29}Si CP MAS NMR spectrum of dehydrated SBA-15 involves 3 signals at -92, -100 and -110 ppm. These signals are assigned to Q²-, Q³- and Q⁴-type species, respectively. After methanol saturation of SBA-15, a similar decrease of signal intensity occurs as that of methanol-loaded Silicalite. Thus, methanol molecules must strongly interact with the surface silanols of SBA-15. In contrast, for water saturated SBA-15, intensities of all three signals significantly increase. This observation may be because of water adsorption on Q²-type groups that the geminal structure of Si(OH)₂ stabilize water molecule by forming more than one H-bond. In this way, H atoms on water join the ^1H - ^{29}Si polarization transfer and the increase of signal intensity overcompensates the decrease part from the O-H bond extension of silanols. Overall, on siliceous materials, the adsorption sites of water or methanol are Si(OH)_x (x = 1-2) groups.

7.3.2 Adsorption Sites on Na-form Materials

The ^{23}Na MAS NMR and ^{27}Al MAS NMR spectra were applied to investigate water adsorption behavior of the Na-ZSM-5 and Na-[Al]SBA-15, as shown in figure 7.5. The analysis of the water adsorption can be sketched out into three key states, *i.e.* saturation, after desorption at 373 K and after desorption at 723 K. For Na-ZSM-5, after water saturation, a slim signal appears at -4 ppm in the ^{23}Na MAS NMR spectrum. Signal maximum shifts from -4 to -20 ppm after desorption at 373 K. This change of isotropic shifts indicates a decline of coordination number after the removal of water molecules. In addition, the signal finally reaches -24 ppm after desorption at 723 K, which hints a further decrease of coordination number, which means the remaining water molecules after the first desorption step are adsorbed on Na^+ cations. Meanwhile, the shape of ^{27}Al MAS NMR considerably changed considerably after water desorption. The signal maximum decreases from 55 to 47 ppm and the signals enormously broaden with an increase of C_q values from 0.8 MHz to 4.5 MHz. This signal broadening is caused by the change of the electronic field during water desorption. However, by simulation of the signals, the isotropic shifts locate at 55 ppm after desorption at 373 K and 723 K, which are the same as the chemical shift in the water-saturated state. This reveals that aluminum atoms keep in tetrahedral coordination. In other words, water molecules are not directly coordinated with aluminum atoms. Since Na^+ cation is the counter ion of framework aluminum, the change in ^{27}Al MAS NMR spectra is attributed to the various coordination number of water molecules at Na^+ species.

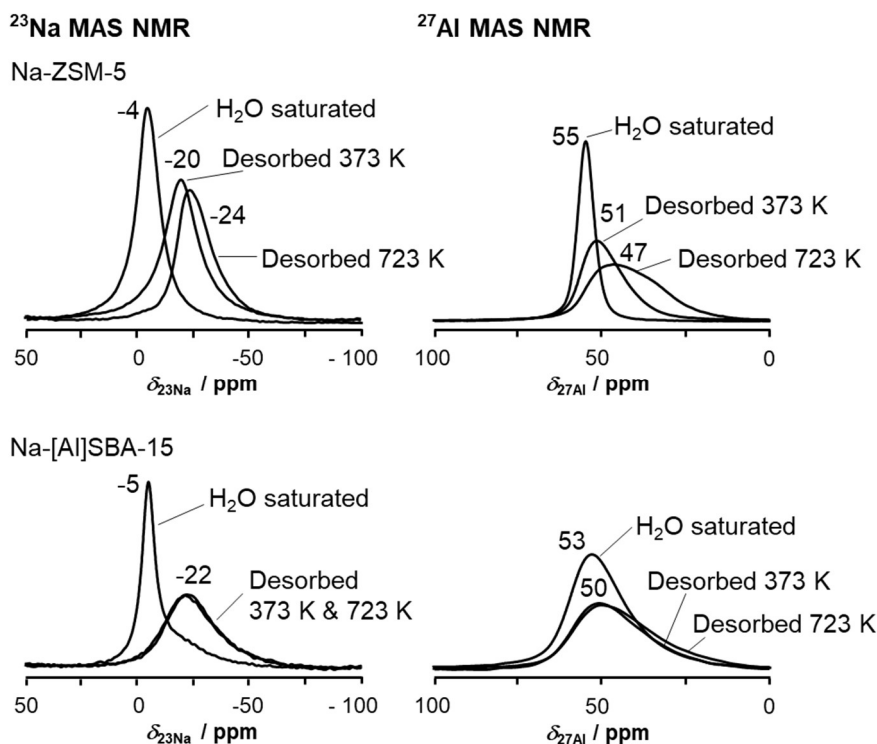


Figure 7.5 ^{23}Na MAS NMR and ^{27}Al MAS NMR spectra of Na-ZSM-5 (top) and Na-[Al]SBA-15 (bottom) after water saturation, after desorption at 373 K and after desorption at 723 K. The chemical shift values are shifts of observed signal maxima.

Similar changes in ^{23}Na and ^{27}Al MAS NMR spectra (figure 7.5, bottom) are observed for Na-[Al]SBA-15. Evacuation of water at 373 K leads to a strong increase in electric field gradient. As a result, the resonance of ^{23}Na nucleus shifts from -5 to -22 ppm, and the signal of ^{27}Al nucleus broadens with a slight shift of signal maxima from 53 to 50 ppm. However, upon further desorption at 723 K, ^{23}Na or ^{27}Al MAS NMR signals are almost identical to the respective signals after desorption at 373 K. Thus, we can conclude that, on Na-[Al]SBA-15, only few water molecules gather around Na^+ cations after desorption at 373 K, which may be due to either low water contents or interaction of water with other adsorption sites.

The methanol adsorption behavior was investigated continuously using ^{23}Na MAS NMR and ^{27}Al MAS NMR spectra. The ^{23}Na MAS NMR signal of CD_3OH saturated Na-ZSM-5 appears at -12 ppm (figure 7.6, top). Consequent desorption steps at 373 K and 723 K cause the piecemeal change of chemical shifts to -21 ppm and finally to -24 ppm. Referred to the water desorption, this difference of isotropic shifts indicates the variation of methanol coordination at Na^+ cations. The ^{27}Al MAS NMR signals broaden with an increase of C_q values from 1.6 MHz (signal maximum at 53 ppm) to 4.5 MHz (signal maximum at 47 ppm). However,

the isotropic shifts of ^{27}Al signals are again constantly at around 55 ppm. Therefore, like water molecules, methanol molecules preferentially interact with Na^+ species, and the change of ^{27}Al MAS NMR spectra are because of the increase of electronic field after methanol desorption from Na^+ cations.

The ^{23}Na and ^{27}Al MAS NMR spectra of methanol on Na-[Al]SBA-15 in different states are shown in figure 7.6, bottom. Desorption at 373 K induces the significant change of ^{23}Na signals, whereas no additional change occurs after the next desorption step at 723 K. For ^{27}Al MAS NMR, the difference also only appears between states of CD_3OH saturation and desorption at 373 K. Therefore, for Na-[Al]SBA-15, no methanol remains at the sodium or the aluminum species after desorption at 373 K. However, it does not mean no methanol persists in this material.

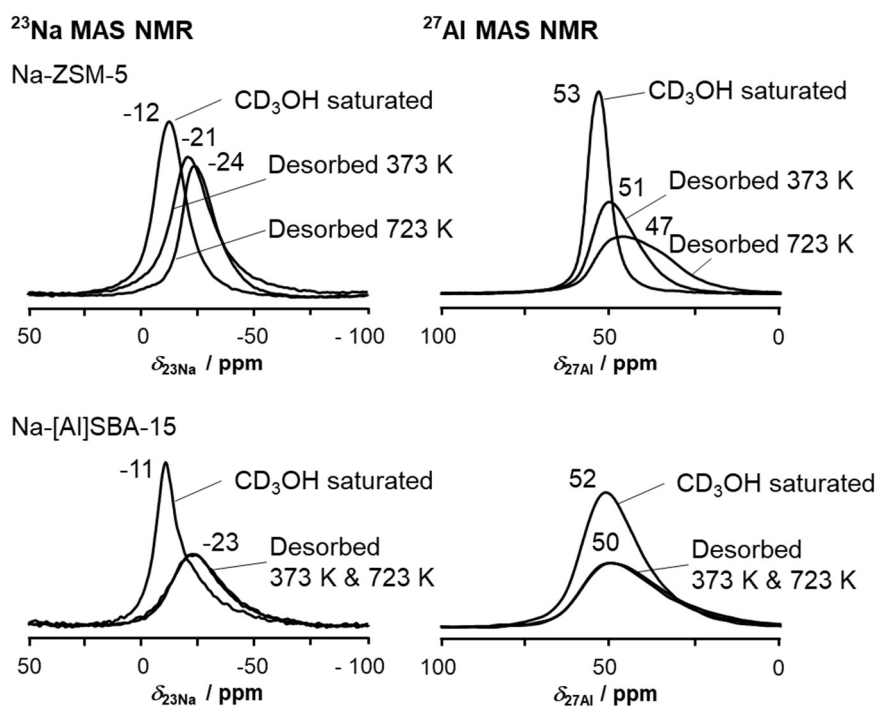


Figure 7.6 ^{23}Na MAS NMR and ^{27}Al MAS NMR spectra of Na-ZSM-5 (top) and Na-[Al]SBA-15 (bottom) after CD_3OH saturation, after desorption at 373 K and after desorption at 723 K. The chemical shift values are shifts of observed signal maxima.

7.3.3 Adsorption Sites on H-form Materials

In this section, we mainly focus on the quantities of acid sites in H-ZSM-5 and H-[Al]SBA-15. These sites are usually considered as the binding sites. However, in order to have a better organization of the whole dissertation, the persuasive evidence of adsorption sites of water and methanol on H-form materials are discussed in section 8.5 and 9.4. ^1H MAS NMR spectra of intrinsic and NH_3 loaded samples are shown in figure 7.7. For dehydrated H-ZSM-5 zeolite, a strong signal of bridging OH groups ($\text{Si}(\text{OH})\text{Al}$) is present at 3.8 ppm, accompanied by a shoulder of $\text{Si}(\text{OH})$ groups at 1.8 ppm.^[75] A new signal at 6.7 ppm appears after NH_3 loading, which is assigned to NH_4^+ cations. Quantification with an external standard determines 0.49 mmol/g ammonium ions, *i.e.* 0.49 mmol/g BAS, on H-ZSM-5. Theoretical studies have reported that the $\text{Si}(\text{OH})\text{Al}$ groups can protonate water and methanol.^[153]

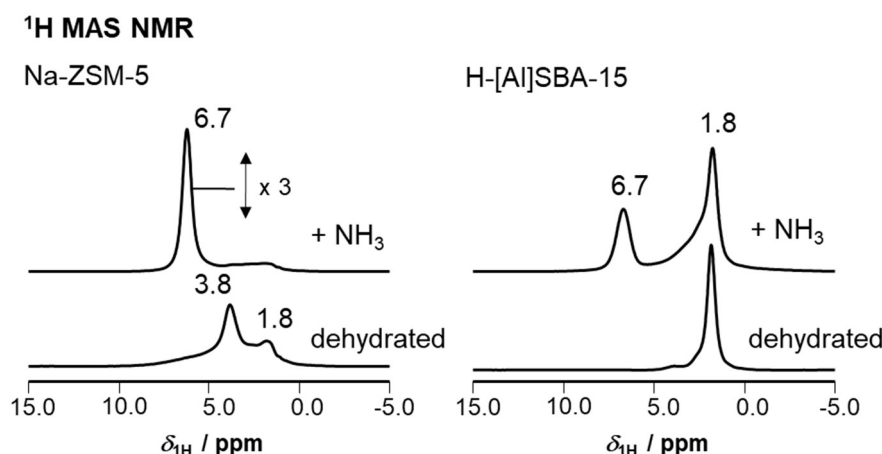


Figure 7.7 ^1H MAS NMR spectra of H-ZSM-5 (left) and H-[Al]SBA-15 (right) in their dehydrated state (bottom) and after NH_3 loading (top).

The signal of $\text{Si}(\text{OH})$ groups at 1.8 ppm dominates the ^1H MAS NMR spectrum of dehydrated H-[Al]SBA-15. Trace amounts of the low-field signal of BAS sites are able to be distinguished on this aluminated SBA-15. After adsorption of NH_3 , the signal of NH_4^+ cations is present at 6.7 ppm. However, the quantity of BAS is low and only 0.18 mmol/g, which is 16% of the total aluminum quantity in H-[Al]SBA-15. As discussed in chapter 5, the BAS in this modified SBA-15 are formed by the flexibly coordinated $\text{Si}(\text{OH})\text{---Al}$ structures and are of weak strength. However, this kind of weak acid sites are still possible to interact with base probe molecules, as observed by others.^{[154],[155]}

7.4 Desorption Enthalpies of Water and Methanol Species

TGA-DSC measurements are applied to determine the desorption enthalpies of water and methanol from porous materials. Considering intermolecular interactions between adsorbate molecules, quantities of adsorbates must influence the desorption enthalpies. Therefore, we analyze the weakly adsorbed molecules at the temperature range from 295 to 373 K and the strongly adsorbed molecules at the temperature range from 373 to 723 K, respectively. All the data are summarized in table 7.2.

Table 7.2 Enthalpies ΔH , of water and methanol desorption from MFI zeolites and SBA-15 materials determined by TGA-DSC measurements

Materials	ΔH [kJ/mol]			
	Weakly adsorbed water ^{a)}	Strongly adsorbed water ^{b)}	Weakly adsorbed methanol ^{a)}	Strongly adsorbed methanol ^{b)}
Silicalite	38	n.d. ^{c)}	39	n.d. ^{c)}
Na-ZSM-5	27	66	33	74
H-ZSM-5	31	63	34	n.d. ^{c)}
SBA-15	41	n.d. ^{c)}	42	n.d. ^{c)}
Na-[Al]SBA-15	38	44	40	60
H-[Al]SBA-15	35	46	41	57
Liquid ^{d)}	39		37	

a) Water or methanol desorbed between 295 and 373 K; b) Water or methanol desorbed between 373 and 723 K; c) Not determined; d) Evaporation heats of liquid water or methanol.

For Silicalite, most water or methanol molecules are weakly bound and are removed below 373 K. The enthalpies of water and methanol desorption from saturated Silicalite are around 38-39 kJ/mol. These values are close to the evaporation heats of water (39 kJ/mol) and methanol (37 kJ/mol), indicating the adsorbates are present as a bulk clusters in these saturated samples.^{[146],[147]} Some literature reported much lower water-desorption heats of 10 to 25 kJ/mol.^{[146],[156]} However, these results are based on a very low loading, where the water/Si(OH) interaction dominates the desorption heat without the influence of intermolecular interactions from bulk species. In our desorption measurements, it is impossible to determine the ΔH after desorption temperature higher than 373 K due to the low quantity of the remaining water or methanol molecules.

7. Binding Sites and Strength of Water and Methanol in Micro- and Mesoporous Materials

Desorption heats of weakly adsorbed water or methanol decrease to 27-34 kJ/mol in ZSM-5 zeolites. These low values imply adsorbates are not existing as bulk clusters in these materials. Considering that water or methanol is mainly adsorbed by Na^+ demonstrated in section 7.3.2, adsorbate molecules may form shells around the Na^+ and be weakly physisorbed. On H-ZSM-5, instead of a core-shell structure, H^+ cations are in fast exchange with protons of water or methanol, and partial protonation of adsorbates occurs as published in literature.^[157] After the removal of the weakly adsorbed molecules, the remaining adsorbates strongly bond with cations (Na^+ or H^+) and exhibit a high desorption heat of 63-74 kJ/mol. However, it is worth noting that the desorption heat of strongly bound methanol on H-ZSM-5 is not detectable because methanol conversion initializes since 425 K, which will be discussed in chapter 8.

Mesoporous SBA-15 materials have a much larger pore diameter (6.7-7.1 nm) than that of microporous MFI zeolites (around 0.56 nm). Therefore, in the saturated state, weakly adsorbed water or methanol forms aggregates in mesopores and contributes to desorption enthalpies of 35-41 kJ/mol and 40-42 kJ/mol, respectively. These values are close to the evaporation heats of 39 kJ/mol (liquid water) and 37 kJ/mol (liquid methanol). Desorption enthalpies of remaining adsorbates from aluminated SBA-15 are 44-60 kJ/mol, which are 16-20 kJ/mol lower than values of ZSM-5 materials. It indicates, on mesoporous aluminosilicates, the remaining water or methanol molecules may not be bonded at Na^+ cations or BAS. Another indication for H-[Al]SBA-15 is no sharp signal appears in the DSC curve of methanol desorption, which means acid catalyzed methanol conversion does not happen on these materials.

In addition, from TGA-DSC measurements, the desorption enthalpies of methanol on these materials are always higher than the values of water, despite their opposite tendency of evaporation heats. This result explains why alcohols conversion continuously proceeds on aluminosilicates without deactivation by the generation of water on active sites.

7.5 Conclusions

By using solid-state NMR and TGA-DSC techniques, we investigate the adsorption sites and desorption enthalpies of water and methanol on siliceous forms, Na-forms and H-forms of MFI-type zeolites and SBA-15 materials. These results provide an important reference for understanding the adsorption/desorption process of water or methanol on porous materials.

For siliceous materials, Si(OH)_x groups are the adsorption sites of water and methanol. Bulk species of adsorbates are formed in pores and intermolecular interactions govern the desorption enthalpies that are close to the evaporation heat of liquid water and methanol. In microporous Na-ZSM-5, Na^+ cations are major adsorption sites. Adsorbates may form a shell around Na^+ , which leads to a low desorption heat (27-33 kJ/mol) of the weakly adsorbed molecules and a high desorption heat (66-74 kJ/mol) of strongly bound molecules. In contrast, adsorbate clusters dominate in saturated the Na-[Al]SBA-15 with desorption enthalpies around 40 kJ/mol. In addition, the remaining molecules are not directly bonded at Na^+ as indicated by the ^{23}Na MAS NMR and lower desorption enthalpies (46-60 kJ/mol) compared with Na-ZSM-5. As quantified by ^1H MAS NMR, 0.49 mmol/g of BAS are the main sites for water or methanol adsorption on H-ZSM-5. The tendency of the desorption enthalpies is similar to its isostructural Na-form. The desorption enthalpies of weakly adsorbed water and methanol (31-34 kJ/mol) are lower than their respective evaporation heats. However, the strongly bonded water performs a desorption enthalpy of 63 kJ/mol. It should be noted that the desorption enthalpy of strongly bound methanol is unmeasurable as the chemical reaction initializes at around 423 K. For H-[Al]SBA-15, the existence of 0.18 mmol/g BAS from flexible-aluminum-coordinated Si(OH) sites only slightly affect water and methanol adsorption. Most adsorbates form clusters with desorption enthalpies in a range of 35 to 41 kJ/mol and the desorption enthalpies of strongly bound species are 46 to 57 kJ/mol. No reaction happens when methanol desorbs from H-[Al]SBA-15 at high temperature, indicates adsorption sites for methanol, maybe also for water, are not BAS but maybe Si(OH) groups.

8. Influence of Confinement and Surface Sites on Methanol Adsorption

8.1 Introduction

Methanol is an intermediate platform chemical, synthesized from abundant feedstocks such as methane, carbon dioxide, coal, biomass, etc., and can then be transferred into value-added chemical commodities.^[158-162] In 1977, the methanol to hydrocarbons (MTH) conversion over H-ZSM-5 was firstly reported by Mobil and has been rapidly developed over the past decades in terms of selectivity and importance for the chemical industry.^[163] For conducting the MTH reaction on acidic zeolites, Brønsted acid sites (BAS) are recognized as the active sites by identification of surface intermediates like surface methoxy species (SMS).^{[164],[165]} However, also other surface groups and counter ions can participate in these reactions and their presence can thus either deactivate or optimize the MTH reaction.^{[101],[166]}

IR and solid-state NMR measurements are frequently applied to experimentally investigate the methanol-related surface species on solid catalysts. Mirth et al. investigated adsorptions of methanol on H-, Na- and K-ZSM-5 and determined the formed complexes by IR spectroscopy.^[167] ¹H MAS NMR measurement typically determines the chemical shift (δ_{1H}) of the hydroxyl group to elucidate the state of methanol. Methanol-*d*₃ (CD₃OH) is commonly used in this study to avoid the influence of methyl-group signal in ¹H MAS NMR spectra. Chemical shifts of pure liquid and gaseous methanol are at 4.7 ppm and 0.02-0.3 ppm, respectively.^{[144],[145]} When methanol interacts with Na cations, the proton signal of the corresponding OH-group appears at around 3.5 ppm.^[144] In contrast, for methanol loading on H-form zeolites, δ_{1H} is at around 9 ppm.^{[144],[157],[168],[169]} It is worth noting that this chemical shift is an averaged value, because this signal is a coalescence of signals of bridging Si(OH)Al groups and H-bonded methanol, which are in fast proton exchange. In order to separate these two species, Hunger et al. performed low-temperature MAS NMR measurements at 77 K, suppressing the effect of proton exchange during the detection time and making individual signals detectable.^[157] In their study, when the methanol/BAS ratio is 1:1, the chemical shifts of CD₃OH and Si(OH)Al were found at 4.1 and 14.2 ppm, respectively. While a higher methanol/BAS ratio of 3 increases the chemical shift of Si(OH)Al groups to 16.5 ppm.

Besides the decisive role of the active sites, the confinement effect was also found to play an important synergistic role in heterogeneous catalytic reactions, which recently received much attention.^{[170],[171]} Microporous confinement is able to stabilize the reaction intermediates,

8. Influence of Confinement and Surface Sites on Methanol Adsorption

like the *tert*-butyl carbocation, in isobutene conversion.^{[172],[173]} By shape-selectivity effects the micropore topologies and cages of zeolites impact the reaction mechanism and, therefore, the product distribution in MTO reaction.^[174] In addition, on mesoporous materials an effect of the mesopore size on the hydration mechanism is reported when studying the pore filling process of MCM-41 and SBA-15.^[175] Although the steric restriction of micropore and mesopore is sometimes crucial for the selectivity and lifetime of a catalyst, materials without confinement, such as metal oxides and active species supported on oxides, are also commonly used for catalysis because shape selectivity effects in pores are not needed or due to the better diffusivity. For example, the silicotungstic acid (STA) and its ion-exchanged form on amorphous silica was applied for isomerization and dehydration of ethanol.^{[60],[176]} Despite its great importance for catalysis, only few researches investigate the influence of confinement on the complexes formed by methanol on solid catalysts.

Herein, we combine solid-state NMR and DRIFTS measurements to quantitatively investigate the methanol desorption process at elevated temperature. Different methanol/surface complexes on solid materials are then proposed accordingly. In order to gain a comprehensive understanding of influencing factors on methanol adsorption process, three series of model materials with different confinements and surface functionalities (table 8.1) are used in this study. From the spectroscopic results, the function of confinement is then differentiated from the effect of surface sites. It is found that strongly adsorption sites vary in different confinements and the confinement of microporous zeolite stabilizes complexes formed by methanol and Na- or H-cations ions. These findings may be helpful for designing new catalysts used in the conversion of alcohols and other polar biomass-derived chemicals.

Table 8.1 Porosity and functionality of materials in this study

Porosity	Siliceous form	Na-form	H-form
Microporous (MFI-type)	Silicalite	Na-ZSM-5	H-ZSM-5
Mesoporous (SBA-15 materials)	SBA-15	Na-[Al]SBA-15	H-[Al]SBA-15
None-porous (Aerosil [®] 200)	A200	Na-STA@A200	H-STA@A200

8. Influence of Confinement and Surface Sites on Methanol Adsorption

In order to clearly explain the interactions between surface sites and adsorbates, some symbols are introduced in the following discussion and a summary is shown in table 8.2. Firstly, “@” symbolizes the surface complexes without exchange with other species. For example, $\text{CD}_3\text{OH}@\text{Si}(\text{OH})$ indicates undisturbed or isolated methanol-Si(OH) complexes. It is worth noting that fast proton exchange internally happens in this kind of species, *i.e.* the protons in the hydroxyl group and silanol group exchange with each other. Secondly, “ $\langle \rangle$ ” symbolizes the exchange between different species. For example, $\text{CD}_3\text{OH}\langle \rangle\text{CD}_3\text{OH}@\text{Si}(\text{OH})$ indicates the exchange of methanol clusters with the methanol adsorbed at Si(OH) groups. Finally, “/” symbolizes the ratio between adsorbates and surface sites. For example, 3.7 $\text{CD}_3\text{OH}/\text{Si}(\text{OH})$ indicates the average ratio between CD_3OH molecules and Si(OH) groups in whole materials is 3.7.

Table 8.2 Symbols used in discussion of interactions between surface sites adsorbates

Symbol	Indication
@	Individual adsorbed species
$\langle \rangle$	Species in exchange with each other
/	Ratio between adsorbates and surface sites

8.2 Physicochemical Characterization

The physicochemical properties of materials are listed in table 8.3. It should be noted that the MFI-type zeolites and SBA-15 materials are the same batch materials as used in chapter 7. In brief, the N_2 physisorption shows typical results of MFI zeolites, where BET surface areas are around $350 \text{ m}^2/\text{g}$ and negligible mesopore volumes of $<0.1 \text{ mL/g}$. Post alumination of siliceous SBA-15 causes decreases in BET surface areas, mesopore volumes and micropore volumes. As discussed in section 7.2, the XRD patterns (figure 7.1 and 7.2) verify the pure phases of these two series materials. The ^{27}Al MAS NMR spectra of aluminum-containing materials (figure 7.3) show tetrahedrally coordinated aluminum in ZSM-5 samples and Na-[Al]SBA-15. Additional extra-framework pentahedral and octahedra aluminum appear after ion exchange of Na-[Al]SBA-15 and subsequent transfer into its H-form, H-[Al]SBA-15. Non-porous Aerosil[®] 200 (A200) exhibits a comparably small BET surface area of $198 \text{ m}^2/\text{g}$ and nearly no micropore volume. After loading of silicotungstic acid (STA), the surface areas further decrease to around $120 \text{ m}^2/\text{g}$.

8. Influence of Confinement and Surface Sites on Methanol Adsorption

It is important for our following discussion to quantify the surface groups of all the materials. For siliceous materials, only Si(OH) groups are detectable and their content varies in a range of 0.39 to 2.20 mmol/g. However, it should be noted that, if taking the BET surface areas into account, the Si(OH) densities are much comparable and are in a range of 1.9-2.5 $\mu\text{mol}/\text{m}^2$. Na-ZSM-5 contains 0.6 mmol/g Na^+ cations and trace amount of Si(OH) groups. Slightly more Si(OH) groups and 0.49 mmol/g BAS are found in H-ZSM-5. However, for aluminum-containing SBA-15 materials, their surface groups consist of not only Na^+ or H^+ cations but also of lots of Si(OH) groups (0.59-1.14 mmol/g). Similar results are found in STA@A200 materials where in addition to the cations around 0.55 mmol/g Si(OH) are present. It is worth noting that traces of Brønsted acid sites (BAS) remain in Na-STA@A200. This is due to the incipient wetness impregnation method applied to transfer the sample into the Na-form, and a similar observation is also identified in the literature.^[60] Overall, all materials are thus in their typical conditions.

Table 8.3 Physicochemical properties of the materials in this study

Material	Si/Al ^{a)}	Si(OH) content [mmol/g] ^{b)}	Na^+ content [mmol/g] ^{a)}	BAS (H^+) content [mmol/g] ^{c)}	S_{BET} [m^2/g]	V_{micro} [mL/g]	V_{meso} [mL/g]
Silicalite	>800	0.66	-	-	350	0.12	0.10
Na-ZSM-5	24	0.08	0.60	-	345	0.12	0.06
H-ZSM-5	24	0.19	-	0.49	372	0.13	0.07
SBA-15	>1600	2.20	-	-	870	0.14	0.93
Na-[Al]SBA-15	12	1.14	0.86	-	522	0.05	0.75
H-[Al]SBA-15	12	0.59	-	0.19	442	0.03	0.72
A200	>1600	0.39	-	-	198	-	0.76
Na-STA@A200	12 ^{d)}	0.57	0.25	0.09	120	-	0.49
H-STA@A200	12 ^{d)}	0.52	-	0.34	123	-	0.56

a) Determined by ICP-OES; accuracy $\pm 10\%$; b) Determined by ^1H MAS NMR; c) After NH_3 loading and determined by ^1H MAS NMR; d) Si/W ratio for STA@A200.

8.3 Methanol on Siliceous Materials

Figure 8.1 shows the ^1H MAS NMR and DRIFTS spectra of samples after methanol saturation and then after stepwise desorption of the methanol from the siliceous materials. In order to easily and clearly describe the states of methanol, the assignments of ^1H MAS NMR signals of these methanol species are summarized in table 8.4. Methanol quantities in siliceous materials are graphically shown in figure 8.2.

Microporous Silicalite is able to capture 2.5 mmol/g methanol from the gas phase at room temperature, which is equal to 3.7 $\text{CD}_3\text{OH}/\text{Si}(\text{OH})$. For this sample, the ^1H MAS NMR signal is found at 3.7 ppm along with a weak shoulder at 7.0 ppm, which is in good agreement with the literature.^[144] Considering that $\text{Si}(\text{OH})$ groups are the only reasonable possible adsorption sites in siliceous materials (see section 7.3.1) and also considering the ratio of methanol to $\text{Si}(\text{OH})$ groups, we assign the main signal to $\text{CD}_3\text{OH} \leftrightarrow \text{CD}_3\text{OH}@\text{Si}(\text{OH})$, *i.e.* the CD_3OH clusters in exchange with methanol at $\text{Si}(\text{OH})$ groups. The chemical shift value of 3.7 ppm is lower than that of liquid methanol at 4.7 ppm, because the $\text{Si}(\text{OH})$ groups at 1.8 ppm join the fast proton exchange averaging both chemical shifts to an intermediate value. Methanol is mostly removed by evacuation at 298 K and less than 0.1 mmol/g of methanol remains in Silicalite after this treatment. In this condition, a signal of isolated $\text{Si}(\text{OH})$ appears at 1.8 ppm with a weak signal at 6.2 ppm is found in the corresponding ^1H MAS NMR spectrum. The high chemical shift of the latter signal indicates a strong bonding of CD_3OH on this site. Thus, we assign it to methanol directly bonded at defect sites (hydrogen-bonded silanol nests). An IR band at 3500 cm^{-1} in desorption state supports the existence of such defect sites.^{[166],[177]} In the DRIFTS spectrum of the saturated sample, signals at 2854, 2952 and 2994 cm^{-1} are attributed to the CH stretching vibrations and the signal at 2920 cm^{-1} is caused by OH stretching vibration of methanol.^[167] The broad signal centered at around 3300 cm^{-1} indicates the hydrogen bonding of methanol molecules and $\text{Si}(\text{OH})$ groups interacting with methanol molecules, which occurs at high methanol loading.^[167] A slim signal at 3630 cm^{-1} is assigned to the $\text{Si}(\text{OH})$ groups disturbed by methanol, *i.e.* $\text{CD}_3\text{OH}@\text{Si}(\text{OH})$, because of its high wavenumber and gradual absence in the following desorption step. A signal at 3725 cm^{-1} appears in the IR spectra upon desorption. It is assigned to the isolated $\text{Si}(\text{OH})$ groups corresponding to the ^1H signal at 1.8 ppm.^[178] It is worth noting that, in contrast to the almost identical ^1H MAS NMR spectra, the IR bands remarkably shift during desorption at elevated temperature and methanol signals are still present even after desorption at 723 K. This is due to the fact that IR spectroscopy is much more sensitive and its data reflects the state of a signal molecule within a very short time,

8. Influence of Confinement and Surface Sites on Methanol Adsorption

whereas solid-state NMR spectroscopy acquires a time- and ensemble-averaged results.^[67]

Methanol capacity is much higher for mesoporous SBA-15 and 9.9 mmol/g methanol is filled into SBA-15 mesopores in the saturation step. This is about 4 times the methanol quantity loaded into Silicalite. In the ¹H MAS NMR spectrum, the main signal is at 4.8 ppm, close to the value of 4.7 ppm of liquid methanol.^[144] Therefore, it is referred to by the term “liquid-like methanol” in the following text. It suggests that intermolecular forces (especially hydrogen bonds) between methanol molecules are the main interaction in this condition. A small signal at 7.9 ppm is assigned to methanol at defects, as discussed for Silicalite. Nearly 90% of the initially present methanol is removed during the desorption at 298 K. We note that also here, the signal of isolated Si(OH) groups appears at 1.8 ppm. The remaining methanol gives now rise to a broad shoulder at around 3 ppm, which is assigned to CD₃OH<>CD₃OH@Si(OH). DRIFTS measurements show similar results to those recorded for Silicalite. The IR band of isolated Si(OH) appears at 3740 cm⁻¹ after the first desorption step. At high temperatures, the signal at 3500 cm⁻¹ is absent, which indicates the absence of the interaction between methanol and the H-bonded Si(OH).

Switching to the non-porous silica A200, the spectroscopic results of methanol saturation and desorption are similar to those of SBA-15. On A200 only 2.8 mmol/g methanol is adsorbed in saturation, however, both A200 and SBA-15 are amorphous silica materials, in contrast to the crystalline Silicalite. Most methanol belongs to liquid-like species with an intensive signal at 4.6 ppm. Some methanol again strongly interacts with defect sites, which leads to the appearance of a signal at 7.8 ppm. Additionally, a slim signal appears at 3.2 ppm, which is close to the signal at 3.7 ppm in Silicalite and is also attributed to CD₃OH<>CD₃OH@Si(OH). The lower chemical shift is probably due to a lower CD₃OH/Si(OH) ratio. Furthermore, the presence of this signal indicates some small cavities exists in A200, where methanol molecules cannot fast exchange with the liquid-like species on the external surface. After the vacuum treatment at 298 K, a slim signal of the individual Si(OH) groups appears at 1.8 ppm. The shoulder on the left side of this is again the CD₃OH<>CD₃OH@Si(OH) species on the surface. This signal gradually disappears in the subsequent desorption steps.

8. Influence of Confinement and Surface Sites on Methanol Adsorption

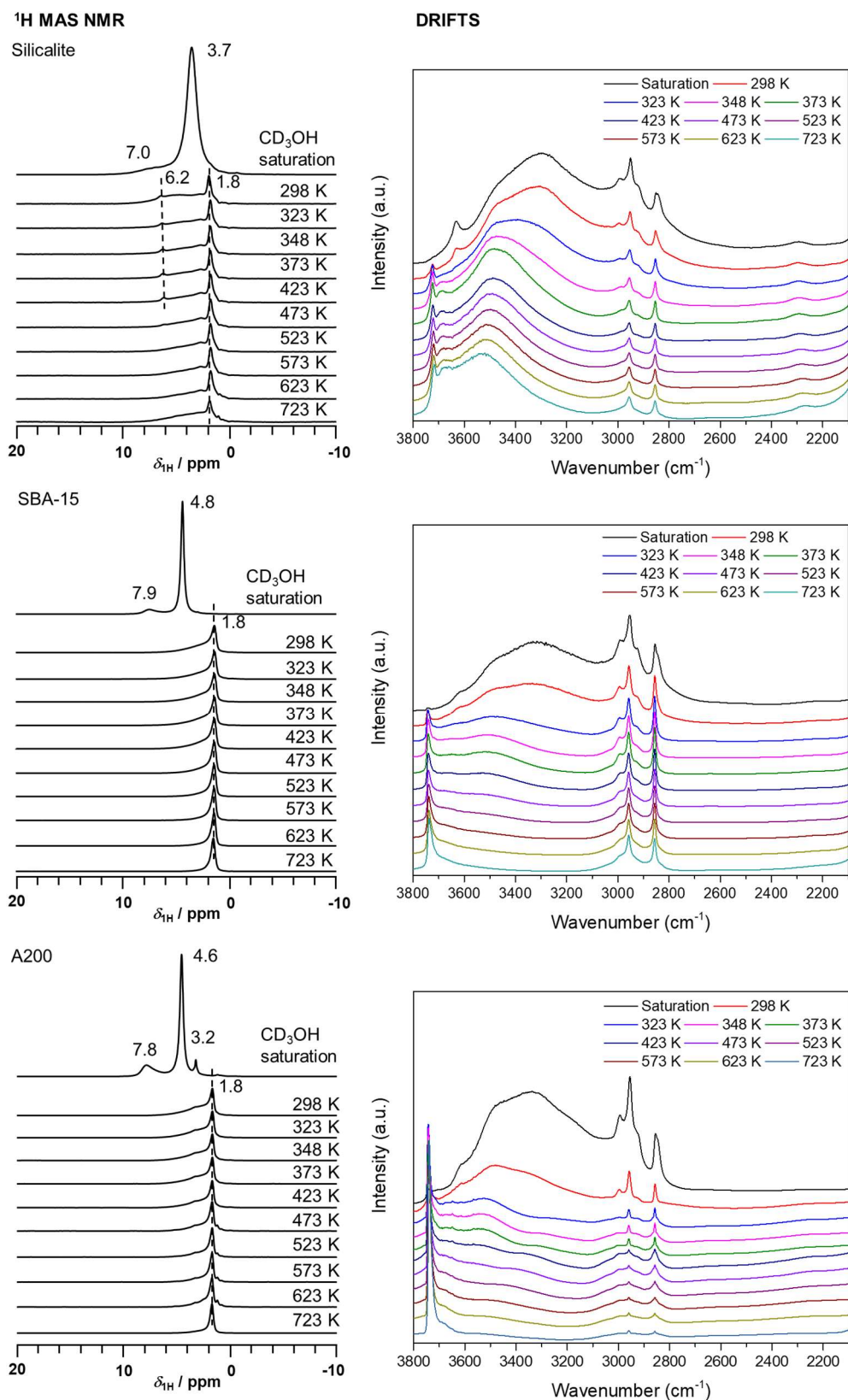


Figure 8.1 ^1H MAS NMR (left) and DRIFTS (right) spectra of methanol saturation at room temperature and desorption at elevated temperature on Silicalite, SBA-15 and A200 (from top to bottom).

8. Influence of Confinement and Surface Sites on Methanol Adsorption

Table 8.4: ^1H MAS NMR signal assignment for methanol (CD_3OH) loaded catalysts

$\delta_{1\text{H}}$ [ppm]	Sample	Description	References
14.4	H-ZSM-5	DME@H^+ ; isolated Si(OH)Al proton coordinating (CD_3) $_2\text{O}$ (DME)	this study
9.8 – 6.8 (6.0)	H-ZSM-5, STA materials	$\text{CD}_3\text{OH} \leftrightarrow \text{CD}_3\text{OH@H}^+$; liquid-like methanol species in exchange with protonated ones	[157],[168], this study
7.9 – 6.2	Silicalite, A200, SBA-15 materials, H-ZSM-5	$\text{CD}_3\text{OH@Si(OH)}$; broad shoulders of initial peaks and later weak and slim signals, OH-groups in hydrogen bonding associated with defects	[144],[179], this study
5.3 – 4.6	A200, SBA-15 and STA materials	Liquid and liquid-like CD_3OH , higher shifts indicate strong surface interactions with counter ions	[144], this study
3.9 – 3.0	All pure silica materials, H-ZSM- 5, STA materials	$\text{CD}_3\text{OH} \leftrightarrow \text{CD}_3\text{OH@Si(OH)}$, liquid-like methanol in exchange with adsorbed species at Si(OH) surface sites	[144],[179]
3.2 – 2.2	Na-ZSM-5, Na-[Al]SBA-15	$\text{CD}_3\text{OH} \leftrightarrow \text{CD}_3\text{OH@Na}^+$; liquid-like methanol in exchange with complexes at the Na^+ counter ion	[168], this study
0.02, 4.7	CD_3OH	Gas and liquid phase CD_3OH	[144], [168]

We graphically compare the methanol quantities on different materials to investigate how the confinement effect influences methanol adsorption. The commonly used absolute values and data normalized by different surface areas and by different Si(OH) densities are shown in figure 8.2. In respect of the absolute quantities (figure 8.2, left), SBA-15 is outstanding in both adsorbing and maintaining methanol throughout desorption steps in vacuum. Similar amounts of methanol are adsorbed on A200 and Silicalite, whereas more methanol remains on A200 during desorption. If taking surface areas or Si(OH) densities into account, the uptake behaviors are more comparable than using the absolute value. This change indicates the primary factor for maximizing methanol saturation is a large surface area with an abundance of Si(OH) groups, as on SBA-15. However, it is impossible to distinguish whether surface area or Si(OH) quantity is the major influence here, because these three materials have comparable Si(OH) density in

8. Influence of Confinement and Surface Sites on Methanol Adsorption

a range of 1.9 to 2.5 $\mu\text{mol}/\text{m}^2$. Furthermore, A200 surpasses SBA-15 in methanol saturation as indicated in the plots in figure 8.2 (middle and right), which reveals the unconfined structure benefits methanol saturation. Upon desorption at elevated temperatures, Silicalite is the worst model material in withholding methanol, even though it has similar Si(OH) density to SBA-15 and A200. However, due to the micropore structure, the confinement effect of Silicalite is much stronger than the other two materials. This means that when a methanol molecule enters the hydrophobic micropore, it is automatically close to the surface without Si(OH) groups, where no binding sites exist. Thus, a binding to other methanol molecules is more favored than adsorption in hydrophobic micropores, apart from Silanol nests present in them. In comparison, materials with large pores or even without pores, but rich in Si(OH), are able to reduce the influence from the hydrophobic surface areas. This phenomenon is known from water adsorption in hydrophobic micropores.^[180] Thus, the stronger the confinement, the stronger the “repulsive” effect. However, this effect cannot explain why A200 outperforms SBA-15 in desorption steps as the mesopore diameter of SBA-15 is 7.1 nm. The pore size of SBA-15 is too large for other surface areas to interact with the adsorbed methanol. Considering Si(OH) groups, especially the defects, are the adsorption sites, we assume A200 could have more defect sites to strongly binding methanol molecules.

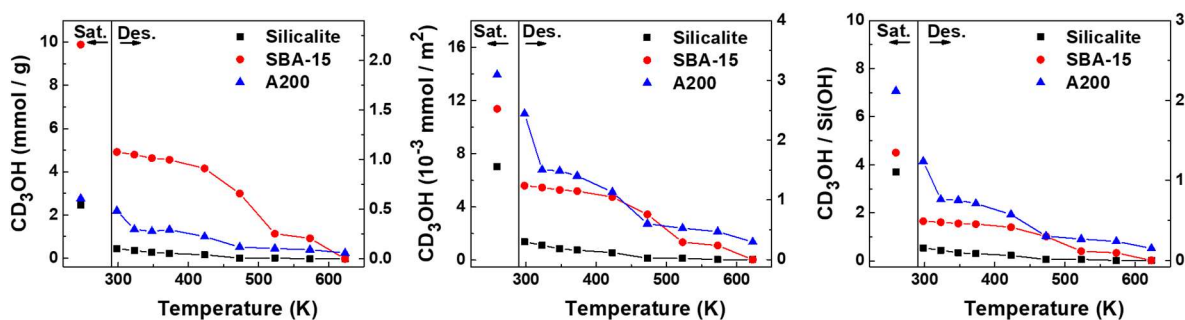


Figure 8.2 Methanol quantities on siliceous materials, plotting in absolute quantities per mass (left), in absolute quantities per surface area (middle), and in the ratio of $\text{CD}_3\text{OH}/\text{Si(OH)}$ (right). The results are from quantitative ^1H MAS NMR measurements with an external standard.

8.4 Methanol on Na-form Materials

For Na-form materials, ^1H MAS NMR and DRIFTS spectra are shown in figure 8.3, and the quantification results are shown in figure 8.4. About 3.0 mmol/g (5.1 $\text{CD}_3\text{OH}/\text{Na}^+$) methanol is adsorbed on Na-ZSM-5 by saturating the material and the methanol causes thereby a broad signal at 3.0 ppm assigned to $\text{CD}_3\text{OH}\langle\rangle\text{CD}_3\text{OH}@\text{Na}^+$ in previous literature.^[144] This low chemical shift, compared with the signal of liquid methanol at 4.7 ppm, is due to the methanol interaction with Na^+ cations. The shift value later decreases further upon the removal of parts of the liquid-like methanol. In the DRIFTS spectra, IR bands of methanol are found in the range of 2845-2995 cm^{-1} , as discussed in section 8.3. According to the literature, the signal at 3614 cm^{-1} is OH stretching of $\text{CD}_3\text{OH}@\text{Na}^+$ species.^[178] The broad signal at 3400 cm^{-1} is the indication of hydrogen bonds. Since the Si(OH) content is only 0.08 mmol/g, this signal must indicate the hydrogen bonds between methanol molecules represented by the ^1H MAS NMR signal at 2.2 ppm. Si(OH) groups have negligible influence on methanol adsorption on Na-ZSM-5 and no clear signals implicate $\text{CD}_3\text{OH}@\text{Si}(\text{OH})$ species in both NMR and IR spectra.

In the saturation state, despite the presence of Na^+ cations and a lower Si(OH) content, the result of Na-[Al]SBA-15 is similar to its parent material, SBA-15. 8.8 mmol/g methanol is loaded on Na-[Al]SBA-15. This high loading, accompanied by a main ^1H MAS NMR signal at 4.9 ppm close to the shift of liquid methanol (4.7 ppm), indicates the intermolecular interactions between liquid-like methanol are dominant in this state. The weak hump at 7.7 ppm can be assigned to methanol binding within defects as discussed for SBA-15. Again, about 90% of the initial methanol is removed during the room-temperature evacuation. Now, a peak at 3.2 ppm appears and is assigned to $\text{CD}_3\text{OH}\langle\rangle\text{CD}_3\text{OH}@\text{Na}^+$, like in Na-ZSM-5. However, in contrast to the remarkable persistence of this complex in micropores, this species directly vanishes in the next desorption step when using mesoporous material in Na-form. Conclusively, the $\text{CD}_3\text{OH}\langle\rangle\text{CD}_3\text{OH}@\text{Na}^+$ species is not as stable in the weak confinement of Na-[Al]SBA-15 as it was in Na-ZSM-5 micropores. This leads to the observed faster removal of methanol than in Na-ZSM-5. In addition, there is no clear signal present at around 3615 cm^{-1} in the DRIFTS measurement. In other words, the remaining methanol binds at Si(OH) groups instead of at Na^+ species in Na-[Al]SBA-15, which agrees with ^{23}Na MAS NMR results in section 7.3.2.

8. Influence of Confinement and Surface Sites on Methanol Adsorption

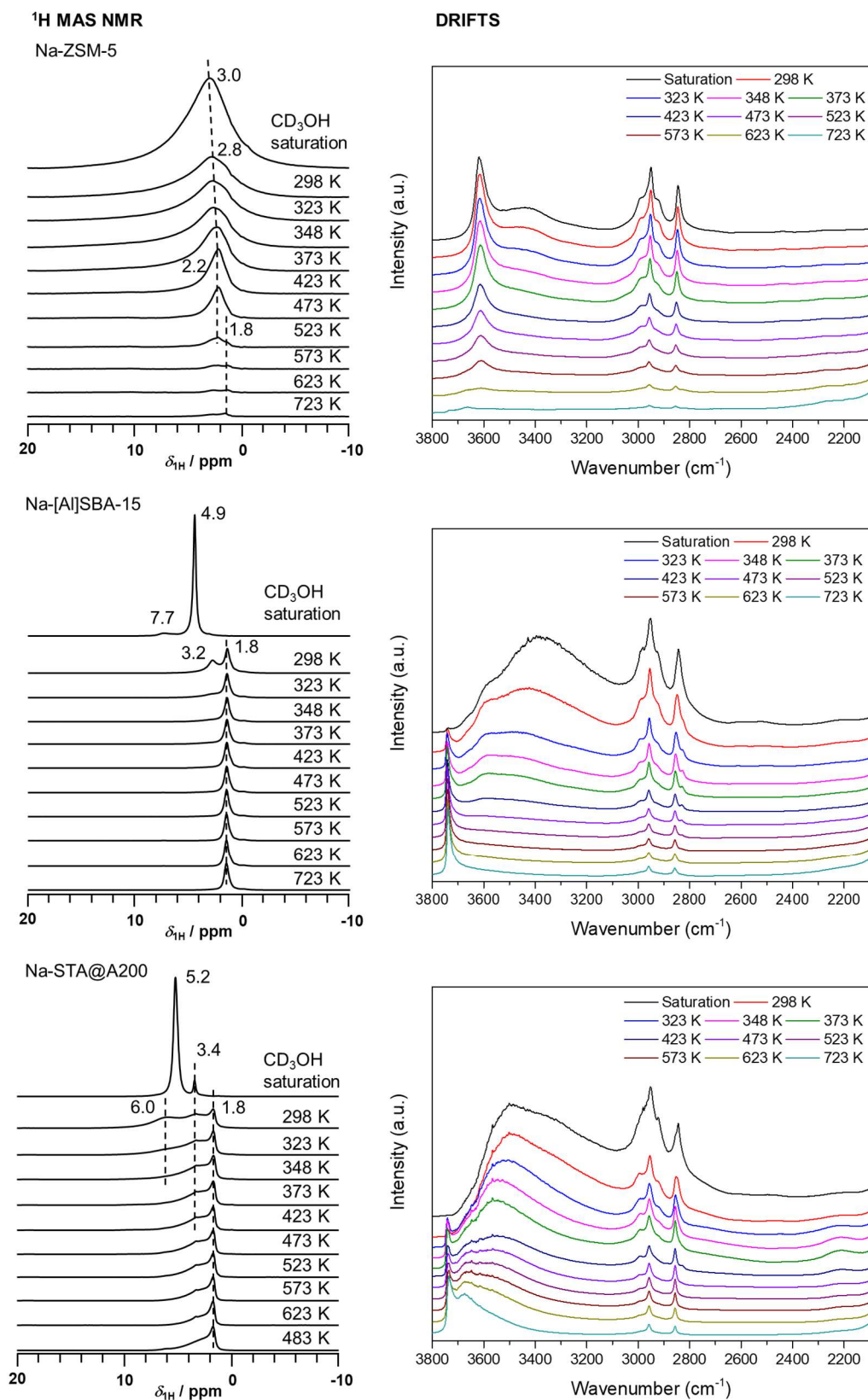


Figure 8.3 ^1H MAS NMR (left) and DRIFTS (right) spectra of methanol saturation at room temperature and desorption at elevated temperature on Na-ZSM-5, Na-[Al]SBA-15 and Na-STA@A200 (from top to bottom).

8. Influence of Confinement and Surface Sites on Methanol Adsorption

Na-STA@A200 captures 3.6 mmol/g of methanol in the saturation step. In the ^1H MAS NMR spectrum, the main signal is present at 5.2 ppm, a little higher than the signal of liquid methanol. This slim signal vanishes in the first desorption step, along with the appearance of a broad signal at 6.0 ppm. Its chemical shift of 6.0 ppm is too high for $\text{CD}_3\text{OH}@\text{Na}^+$ complexes. Meanwhile, it should also not be methanol at defects, since STA is supported on bare A200 and no such signal appears during the removal of methanol from A200. Considering the trace amount of Brønsted acid sites (BAS, 0.09 mmol/g) that are still present on this material, this high shift is, therefore, assigned to $\text{CD}_3\text{OH}@\text{H}^+$ species (detailed explanation see section 8.5). However, we cannot rule out the possibility that $\text{CD}_3\text{OH}@\text{Na}^+$ and $\text{CD}_3\text{OH}@\text{H}^+$ are close and are able to exchange with each other. But, anyway, H^+ cations must be involved in this 6.0 ppm signal. Therefore, the 5.2 ppm signal in saturation state is assigned to liquid-like species in exchange with surface methanol complexes ($\text{CD}_3\text{OH}@\text{Na}^+$ and $\text{CD}_3\text{OH}@\text{H}^+$). Similar to the findings and discussion made for Na-[Al]SBA-15, the surface complexes no longer persist and the signal at 6.0 ppm disappears fast after evacuation at higher temperatures. This supports that the stability of complexes with counter ions in unconfined structures is weaker than in micropore confined Na-ZSM-5. In addition, the initially appearing slim signal at 3.4 ppm is similar to the signal at 3.2 ppm in methanol saturated A200. Thus, it is attributed to isolated methanol clusters' hydrogen bonding with Si(OH) groups ($\text{CD}_3\text{OH} \leftrightarrow \text{CD}_3\text{OH}@\text{Si}(\text{OH})$ species) of the support. It must be noted that, in order to prevent the decomposition of the Keggin units of STA, the reference spectrum of Na-STA@A200 is only treated at 483 K prior to further loadings. The slim signal at 1.8 ppm and broad hump at around 2.5 ppm are the isolated and hydrogen-bonded Si(OH) groups, respectively.^[60]

Detailed comparisons of methanol quantities on Na-from materials are shown in figure 8.4. In the saturation state, mesoporous material, Na-[Al]SBA-15, is the winner with a methanol capacity of 8.8 mmol/g. After normalizing the absolute quantities with surface areas and surface sites, we see again the non-porous material surpasses the mesoporous one, just as the siliceous material does. As shown in table 8.3, the main differences between Na-[Al]SBA-15 and Na-STA@A200 are surface area and the number of Na^+ sites. Considering the liquid-like CD_3OH is the dominant species in both of them, the surface area should be more important than surface sites for methanol uptake in these weak confined materials. In contrast, Na-ZSM-5 has comparable surface areas and surface sites to Na-[Al]SBA-15. But the different restriction of methanol within micropores respectively mesopores leads to a huge difference in pore volumes which clearly influences the quantity of methanol adsorption. However, the

8. Influence of Confinement and Surface Sites on Methanol Adsorption

liquid-like species is removed fast from Na-[Al]SBA-15 and Na-STA@A200, whereas Na-ZSM-5 maintains most CD₃OH molecules during the desorption steps in form of surface adsorbates. The CD₃OH \leftrightarrow CD₃OH@Na⁺ species in Na-ZSM-5 are strongly restricted in the pores and are able to persist at above 423 K. Since Na⁺ cations are found to dominate the methanol adsorption in Na-ZSM-5, it can be concluded that the restricted confinement is attributed to the stabilization of methanol complex in micropores.

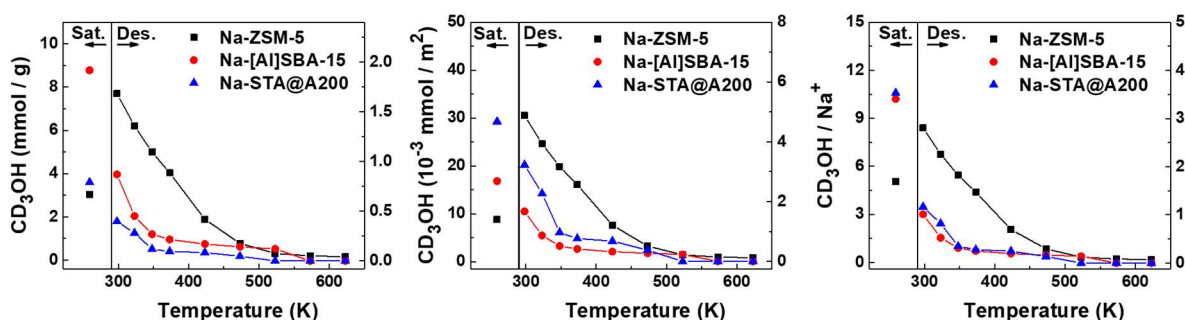


Figure 8.4 Methanol quantities on Na-form materials, plotting in absolute quantities per mass (left), in absolute quantities per surface area (middle), and in the ratio of CD₃OH/Na⁺ (right). The results are from quantitative ¹H MAS NMR measurements with an external standard.

8.5 Methanol on H-form Materials

For H-ZSM-5, the main signal appears at 7.7 ppm in the saturation state (figure 8.5). In contrast to the Na⁺ cations discussed in the previous section, the H⁺ cations in H-forms are actively involved in the fast proton exchange with protons of methanol hydroxyl groups. Hunger et al. showed that the pure chemical shift of methanol disturbed BAS could be higher than 14 ppm.^[157] Thus, when the H⁺ cations and methanol OH groups exchange with each other, this must result in an averaged signal of both species that is then expected in the lower field (high chemical shift) region relative to the signal of liquid methanol. In addition, Zachariou et al. demonstrated methanol molecules are hydrogen-bonded with each other in H-ZSM-5 at 298K.^[181] Therefore, the signal at 7.7 ppm is an averaged signal and assigned to liquid-like methanol in fast exchange with surface methanol complexes (CD₃OH \leftrightarrow CD₃OH@H⁺). It is worth noting that the chemical shift value of an averaged signal is variable, as it depends on the specific methanol/H⁺ ratio of the surface complex of the signal. Chemical shifts of such averaged signals were found to increase from 8.5 ppm to 9.5 ppm when the ratio of CD₃OH/H⁺

8. Influence of Confinement and Surface Sites on Methanol Adsorption

decreased from 3 to 1.^[157] In our spectra, this averaged signal gradually shifts to 9.3 ppm and then shifts back to 8.5 ppm along with the decrease of $\text{CD}_3\text{OH}/\text{H}^+$ ratio from 7.4 to 0.3, when methanol is desorbed at elevated temperatures. Another initial signal at 3.5 ppm can be assigned to $\text{CD}_3\text{OH} \leftrightarrow \text{CD}_3\text{OH}@\text{Si}(\text{OH})$, referred to similar findings for the Silicalite. This species is rather stable in H-ZSM-5 and still persists even after desorption at 373 K. The signals that appear at 6.5-7.0 ppm are again assigned to methanol at defect sites. In addition to the aforementioned signals, a downfield-shifted signal at 14.4 ppm appears after desorption at 423 K. Signals in this area have been observed at a low temperature of 153 K, where the proton exchange process is slow and individual species are detectable.^[157] The authors concluded that when $\text{CD}_3\text{OH}/\text{H}^+$ is 1:1, a signal at 14.2 ppm was due to the bridging $\text{Si}(\text{OH})\text{Al}$ group disturbed by adsorbed methanol. However, our measurement is conducted at 298 K. At this temperature, the $\text{Si}(\text{OH})\text{Al}$ sites should be in proton exchange with the nearby CD_3OH molecules and result in merging ^1H MAS NMR signals. The averaged signal would then be expected in the range of 7.7-9.5 ppm, as discussed above.

To clarify this unknown signal, we study the DRIFTS spectra. When H-ZSM-5 is saturated by methanol (figure 8.5, top), IR bands are present at 2846-2995 cm^{-1} and at around 3300 cm^{-1} corresponding to individual methanol molecules and the hydrogen bonds among them, respectively. The IR band of bridging $\text{Si}(\text{OH})\text{Al}$ locates at around 3600 cm^{-1} . Initially, it is a little broad due to the interaction with methanol.^[182] After 523 K, the band becomes slim, indicating the intact bridging $\text{Si}(\text{OH})\text{Al}$. It is worth noting that the intensity of this band decreases at elevated temperatures and almost vanishes after heating at 473 K. This can be attributed to the occurrence of methanol dimerization, forming dimethyl ether (DME) adsorbed on the BAS.^[178] Meanwhile, new IR bands at 2840, 2945, 2969 and 3010 cm^{-1} appear, confirming the existence of DME.^{[178],[183]}

8. Influence of Confinement and Surface Sites on Methanol Adsorption

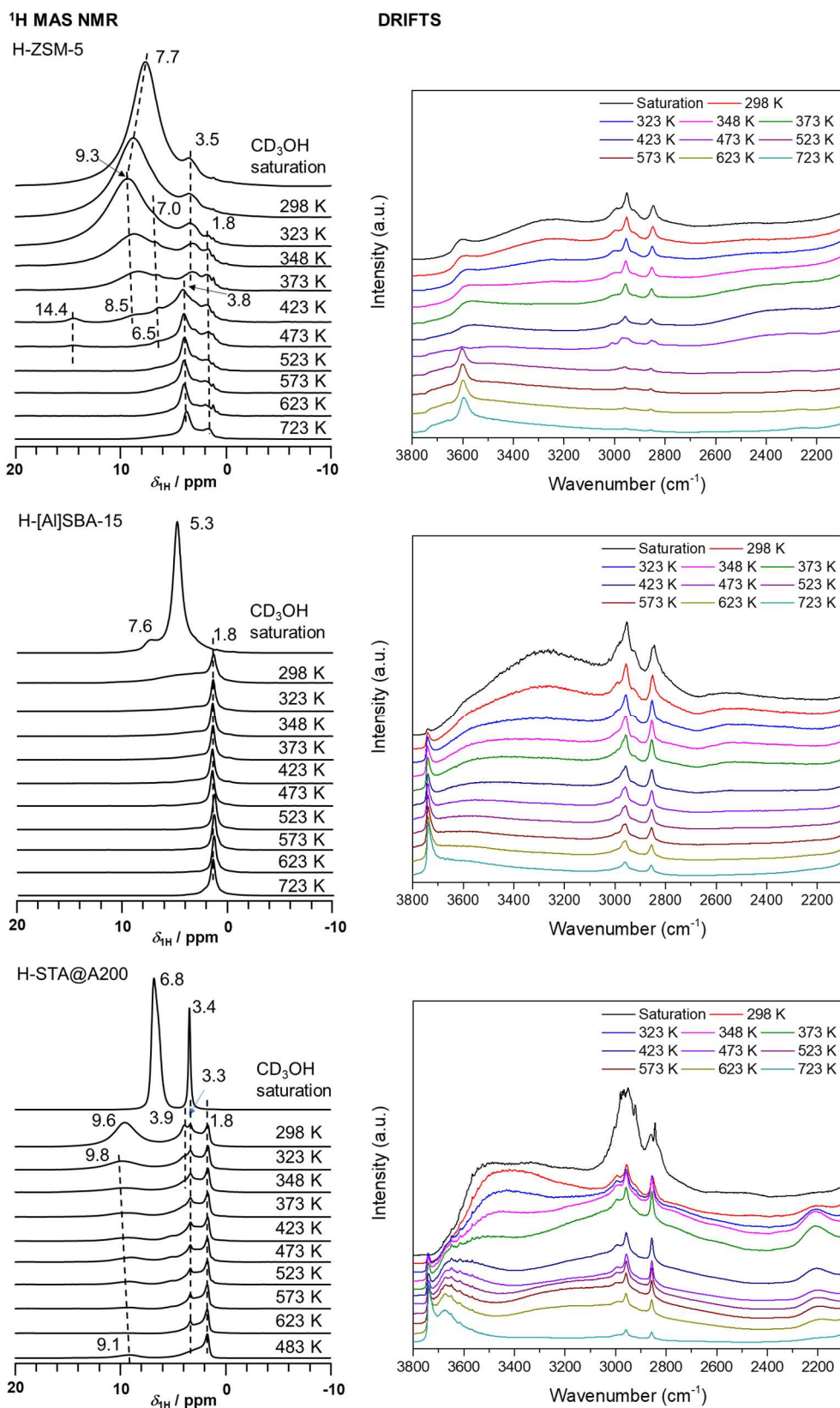


Figure 8.5 ^1H MAS NMR (left) and DRIFTS (right) spectra of methanol saturation at room temperature and desorption at elevated temperature on H-ZSM-5, H-[Al]SBA-15 and H-STA@A200 (from top to bottom).

8. Influence of Confinement and Surface Sites on Methanol Adsorption

To verify the DME species, ^{13}C CP MAS NMR was performed with ^{13}C labeled methanol ($^{13}\text{CH}_3\text{OH}$) during the stepwise desorption of methanol (figure 8.6, left). The methanol signal appears at 50 to 53 ppm (table 8.5) initially and its intensity decreases upon stepwise methanol desorption.^[184-186] After the evacuation at 423 K, new signals at 59 and 63 ppm appear. Such signals are commonly assigned to DME by other studies.^{[184],[185],[187]} It is worth noting that CD_3OH was used for ^1H MAS NMR measurements. Therefore, the formed DME must also be completely deuterated and conclusively it remains invisible in the ^1H MAS NMR spectra (figure 8.5). However, the proton affinity of DME is 792 kJ/mol, which is 38 kJ/mol higher than that of methanol.^[188] Therefore, it is reasonable to assign this ^1H signal at 14.4 ppm to the DME adsorbed at BAS, *i.e.* DME@H⁺ species. We note that the methanol conversion to DME is accompanied by the formation of water on the sample. However, due to the low quantities of water generated, no corresponding signals appear in ^1H MAS NMR spectra. Surface methoxy species (SMS) could also be formed as an intermediate, as they are in acid zeolite catalyzed methanol conversion. The SMSs' chemical shift ($\delta_{13\text{C}} = 59.5$ ppm) is similar to that of DME.^{[185],[186]} However, according to the literature, the SMS leads to the decreased quadrupolar coupling constant (C_q) of the corresponding framework aluminum.^[187] Thus, to clarify the SMS, ^{27}Al MAS NMR spectra were collected upon the stepwise methanol desorption (figure 8.6, right). With the removal of methanol, the signal of tetrahedral aluminum at 55 ppm becomes weak and broad, and then disappears after desorption at 423 K. It indicates a strong increase of the C_q value. In other words, the symmetry of Al atoms decreases due to few adsorbates located there. Conclusively, few or no SMS have formed that keep the aluminum in tetrahedral coordination and thus a negligible effect from SMS is present in our measurements. This also clarifies that SMS are not the major contributor to the ^{13}C signal at 60 ppm, which is important for later quantification discussion. After desorption at 473 K, methanol and DME related signals almost vanish from ^1H MAS NMR spectra, whereas the corresponding ^{13}C signals and IR bands persist at higher temperatures. It indicates the latter two methods are more sensitive in the detection of methanol and DME.

8. Influence of Confinement and Surface Sites on Methanol Adsorption

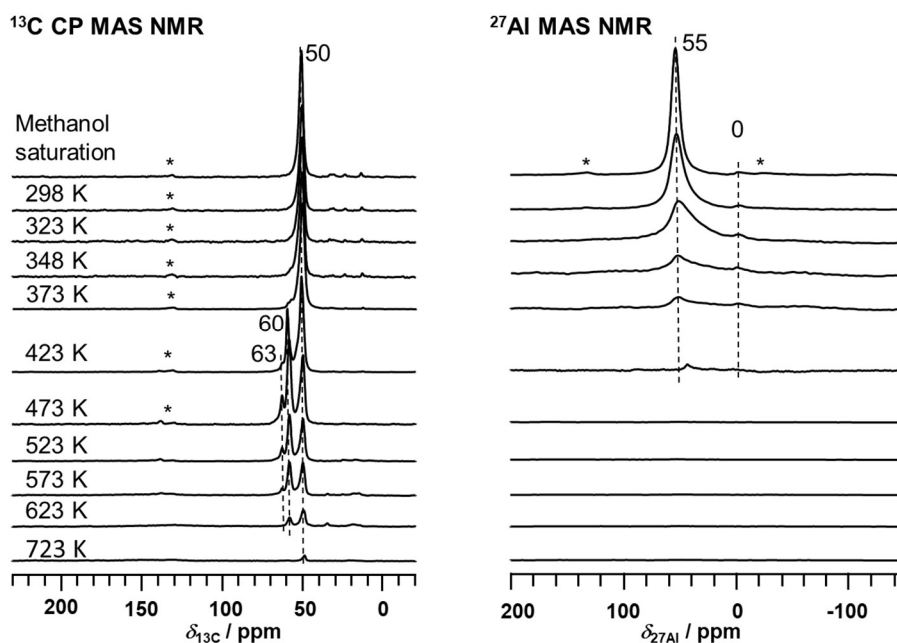


Figure 8.6 ^{13}C CP MAS NMR, ^{27}Al MAS NMR spectra of stepwise CH_3OH desorption from H-ZSM-5.

Table 8.5: ^{13}C CP MAS NMR signal assignments after $^{13}\text{CH}_3\text{OH}$ loadings on H-ZSM-5 and H-STA@A200

Chemical shift $\delta_{^{13}\text{C}}$ (ppm)	sample	References
78	<i>gem</i> -Diol-type species on STA Keggin units	[189]
66	$^{13}\text{CH}_3\text{OH}$ on STA	This study
63	Dimethyl ether, side-on configuration	[165],[184]
60.5 - 59.5	Dimethyl ether, end-on configuration	[184] [185]
50 - 53	$^{13}\text{CH}_3\text{OH}$ in side-on and end-on configuration	[185],[186]

Compared to H-ZSM-5, methanol adsorbed on mesoporous H-[Al]SBA-15 shows a different picture. The material is initially loaded with 5.18 mmol/g of CD_3OH , which is about 1.5 times the loading that was achieved for H-ZSM-5 (figure 8.8). In the ^1H MAS NMR spectrum, methanol saturated H-[Al]SBA-15 shows a major signal at 5.3 ppm and a weak shoulder at 7.6 ppm. Both signals are again assigned to liquid-like species and methanol at defect sites, respectively. After desorption at 298 K, the initial signals disappear, accompanied by the appearance of an isolated Si(OH) signal at 1.8 ppm. The DRIFTS spectra are in good

8. Influence of Confinement and Surface Sites on Methanol Adsorption

agreement with ^1H MAS NMR spectra on this. The signal of methanol shows in the range of $2845\text{-}3000\text{ cm}^{-1}$ and a broad band of hydrogen-bonded methanol appears at around 3300 cm^{-1} . However, no signal indicates the protonated CD_3OH , *i.e.* $\text{CD}_3\text{OH}@\text{H}^+$ complexes, in ^1H MAS NMR and DRIFTS spectra. This must be attributed to the weak BAS acid strength in this material, as demonstrated in section 6.4.

In $\text{H-STA}@\text{A200}$, the saturation loading is 5.3 mmol/g . The main signal appears at 6.8 ppm representing the liquid-like methanol in exchange with $\text{CD}_3\text{OH}@\text{H}^+$ species ($\text{CD}_3\text{OH} \leftrightarrow \text{CD}_3\text{OH}@\text{H}^+$), referred to H-ZSM-5. Its lower chemical shift compared to the value of 7.7 ppm in H-ZSM-5 is due to the high $\text{CD}_3\text{OH}/\text{H}^+$ ratio, *i.e.* high amount of liquid-like CD_3OH (chemical shift of 4.7 ppm). The slim signal at 3.4 ppm is similar in nature to that at 3.2 ppm in A200 and assigned to methanol in exchange with the $\text{CD}_3\text{OH}@\text{Si}(\text{OH})$ species, which is trapped in special cavities preventing the methanol exchange with the external surface. Upon desorption at 298 K and 323 K , the signal stepwise shifts downfield to 9.8 ppm . This shift is caused by the removal of liquid-like methanol contributing to the coalescence signal. Again, this is comparable to the observations on H-ZSM-5 and to observations from the literature.^[157] New signals appearing between 3.3 and 3.9 ppm are explained by $\text{CD}_3\text{OH} \leftrightarrow \text{CD}_3\text{OH}@\text{Si}(\text{OH})$ species. In the DRIFT spectra, again, only methanol and hydrogen bond species are observed in the saturated condition. The IR band of $\text{Si}(\text{OH})$ appears again at 3742 cm^{-1} after desorption at 298 K . This agrees to the presence of the ^1H signal at 1.8 ppm . Because STA is a strong acid catalyst, methanol dimerization could happen on it like on H-ZSM-5. Although no DME or SMS related signal is observed in the spectra of ^1H MAS NMR and DRIFTS, ^{13}C labeled methanol and ^{13}C CP MAS NMR spectroscopy were applied to verify whether the reaction occurs on the acidic surface of $\text{H-STA}@\text{A200}$ (figure 8.7). Besides the methanol signal at 51 ppm , a signal at 66 ppm initially appears in the ^{13}C CP MAS NMR spectrum. This chemical shift is close to the above-mentioned DME signal of $60\text{-}63\text{ ppm}$. However, it seems impossible for methanol conversion to DME at room temperature. Therefore, this signal is tentatively assigned to methanol adsorbed at Keggin units. After desorption at 373 K , an additional signal at 78 ppm appears. This chemical shift is typical for the *gem*-diol type structure, which is formed by a carbonyl group adsorbed on an open M-OH site.^[189] In our case, such *gem*-diol type structures could come from traces of formaldehyde reacting at W-OH sites on STA, since the formation of formaldehyde has been reported in methanol conversion at elevated temperature.^[190] Meanwhile, another possibility is a methanol molecule adsorbs on the W=O site in Keggin units and forms the *gem*-diol type structure. After the treatment at 623 K , only

8. Influence of Confinement and Surface Sites on Methanol Adsorption

a trace amount of methanol is observable in the ^{13}C CP MAS NMR and no DME forms throughout methanol desorption from H-STA@A200.

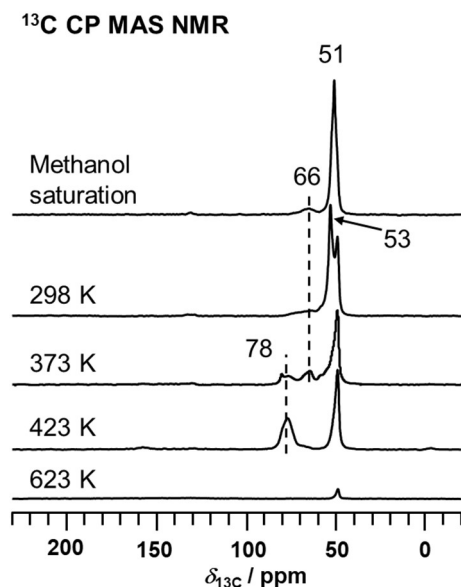


Figure 8.7 ^{13}C CP MAS NMR of CH_3OH desorption from H-STA@A200.

The quantifications of stepwise methanol desorption on H-form materials are found in figure 8.8. Comparable quantities (5.2-5.3 mmol/g) of methanol are captured by H-[Al]SBA-15 and H-STA@A200, which are higher than the 3.6 mmol/g of H-ZSM-5. The ratio of the absolute values among these three materials are about 2 : 3 : 3 (H-ZSM-5 : H-[Al]SBA-15 : H-STA@A200). Whereas the ratio of $\text{CD}_3\text{OH}/\text{H}^+$ ratios among them is around 2 : 7 : 4. The discrepancy of the two ratios reveals that the methanol saturation quantities are not correlated to the number of acid sites. H-ZSM-5 surpasses the other H-form materials in reserving methanol at temperatures below 373 K. At 373 to 523 K, comparable quantities of methanol are maintained by H-ZSM-5 and H-[Al]SBA-15. At this point, trace amounts of DME are found in H-ZSM-5. After 523 K, comparable low quantities of methanol stay on these three materials, similar to the Na-forms. When surface areas are taken into account, H-STA@A200 outperforms porous H-form materials in methanol saturation due to its un-confined structure. The large difference between H-STA@A200 and H-[Al]SBA-15 may indicate that strong acidity also contributes to methanol saturation. After normalizing the absolute methanol quantity with H^+ density, the $\text{CD}_3\text{OH}/\text{H}^+$ ratio of H-ZSM-5 is higher than that found for H-STA@A200. This indicates that a strong micropore confinement benefits the stability of

8. Influence of Confinement and Surface Sites on Methanol Adsorption

$\text{CD}_3\text{OH}@H^+$ complexes, as it did for complexes at Na^+ . Note that normalizing with H^+ density is meaningless for H-[Al]SBA-15, because, as observed in the MAS NMR and DRIFTS spectra, the weak BAS barely bind methanol molecules on this mesoporous material.

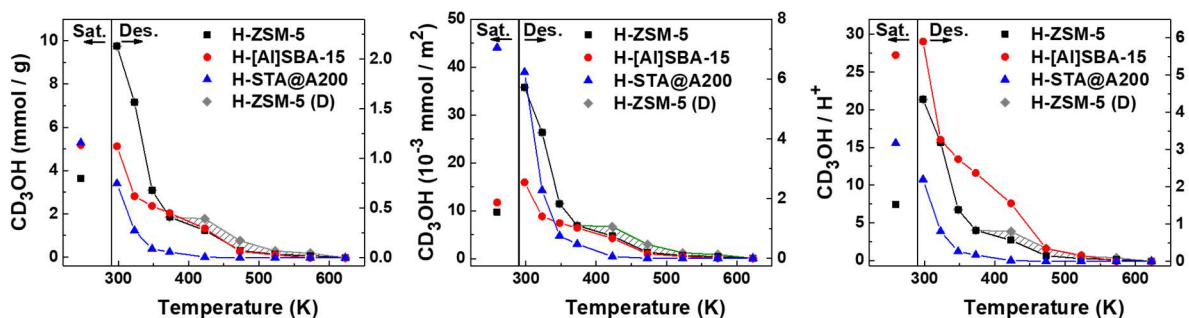


Figure 8.8 Methanol quantities on H-form materials, plotted in absolute quantities per mass (left), in absolute quantities per surface area (middle), and in the ratio of $\text{CD}_3\text{OH}/H^+$ (right). The results are from quantitative ^1H MAS NMR measurements with an external standard. H-ZSM-5(D) represents the quantity of methanol corrected by the quantity of DME in methanol equivalents (= two times n_{DME}) and the shaded area thus represents the quantity of DME on H-ZSM-5 in methanol equivalents. The quantity of DME is from quantitative ^{13}C MAS NMR using ^{13}C signal of methanol as internal standard.

8.6 Influence of Material Surface Groups and Confinement

In the previous pages, how confinement influences methanol adsorption on siliceous, Na-form, and H-form materials has been separately discussed. Here, we put the absolute methanol uptakes at the chosen steps of all the materials mentioned above together to comprehensively overview on the impacts of material surface sites on the methanol adsorption (figure 8.9). For the methanol saturation, mesoporous SBA-15 materials, especially the parent SBA-15, surpasses other microporous and non-porous analogues. In this condition, a liquid-like methanol species is the major component present on the material. Here the intermolecular interactions, mostly hydrogen bonds between methanol molecules, are dominating and interactions between adsorbate and surface sites are of minor importance. Thus, materials with a large surface area and pore volume are able to store more methanol in this liquid-like form. However, it is noteworthy that the presence of counter ions, such as Na^+ and H^+ , is helpful for a higher methanol loading. Considering the methanol reservation capacities after the first desorption at 298 K, aluminum-containing microporous zeolites outperform the other materials. As discussed above, at this step, $\text{CD}_3\text{OH} \leftrightarrow \text{CD}_3\text{OH}@Na^+$ and $\text{CD}_3\text{OH} \leftrightarrow \text{CD}_3\text{OH}@H^+$ are

8. Influence of Confinement and Surface Sites on Methanol Adsorption

dominant in Na-ZSM-5 and H-ZMS-5, respectively. Nevertheless, such species are almost absent in the mesoporous and non-porous analogues. Only few $\text{CD}_3\text{OH} \leftrightarrow \text{CD}_3\text{OH}@\text{H}^+$ species are present in H-STA@A200, whereas they decomposed quickly in the following desorption steps. Thus, the strong confinement of micropores shows a significant promotion on the interactions between methanol and counter ions. In the desorption at 373 K, it is expected that ZSM-5 materials can still save some methanol at the Na^+ or H^+ cations in their constrained micropores. However, a higher amount of methanol persists in SBA-15 due to the extremely high surface area and Si(OH) content, which indicates the Si(OH) groups could be strong binding sites for methanol.

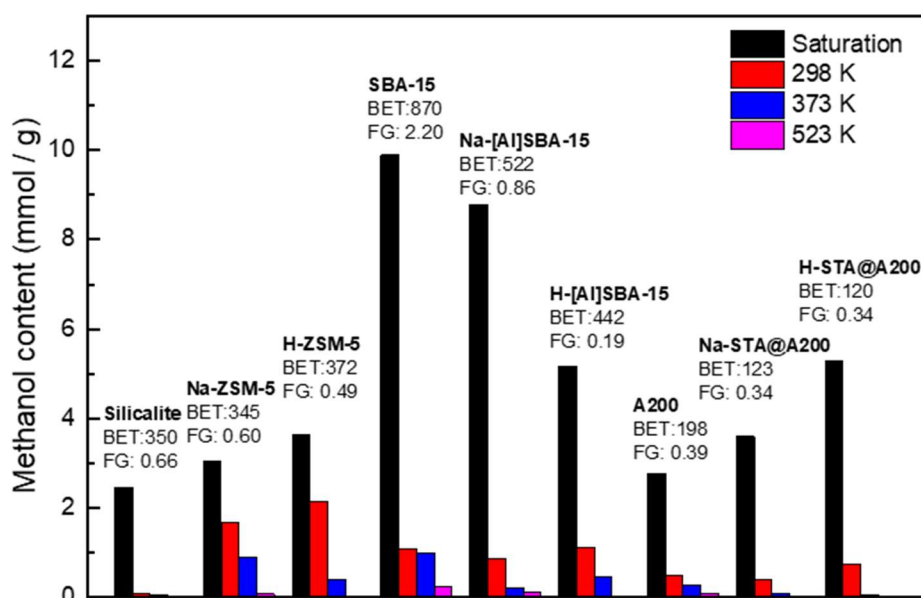


Figure 8.9 Methanol quantities of materials with different surface sites and confinement at chosen steps. From left to right: microporous MFI zeolites, mesoporous SBA-15 materials, and non-porous A200 supported STA. The unit of the BET surface area (BET) is m²/g and the unit of number of the functional groups is given in mmol/g.

8.7 Conclusions

In summary, by using solid-state NMR spectroscopy and DRIFTS, we qualitatively and quantitatively investigate methanol saturation and stepwise desorption on microporous MFI zeolites, mesoporous SBA-15 materials and A200 supported STA materials in their siliceous, Na-forms and H-forms. Upon methanol saturation, liquid-like species appear in all the materials. The available porosity, *i.e.* surface area and pore volume, is the key parameter that determines the saturation adsorption capacity of methanol. A liquid-like species forms, where interactions between methanol molecules are more pronounced than interactions with surface sites. However, methanol adsorption can also be improved by inducing Na⁺ or H⁺ counter ions, if modification barely changes the surface area and pore volume.

The microporous confinement, strengthening adsorbate-surface interactions, is a double-edged sword for preserving methanol and its effect depends on the respective surface sites of materials. Its impact becomes obvious after the desorption at 298 K. On the one hand, the strong confinement stabilizes the surface complexes (CD₃OH/Na⁺ or CD₃OH/H⁺) and gives rise to a high methanol quantity after the first desorption step. The complexes at Na⁺ cations even persist up to 523 K. These complexes are not found or decompose significantly faster on [Al]SBA-15 and STA@A200 materials. Whereas Si(OH) defects become the strong binding sites on these materials. In addition, dimethyl ether was identified in H-ZSM-5 instead of H-[Al]SBA-15 and H-STA@A200. Another implication is that microporous confinement enhances the interactions between methanol and counter ions.

On the other hand, confinement in siliceous materials causes a repulsive effect on methanol molecules, as no surface complexes can form except interaction with Si(OH) sites. During the first desorption step, most methanol molecules are evacuated and only negligible amounts of methanol remain adsorbed at defects on Silicalite. At the same time, on the less confined SBA-15 and A200 a lot of methanol is still present due to a different surface rich in Si(OH). Some of formed CD₃OH@Si(OH) species persist even after desorption at 523 K. In other words, the retention of methanol on these materials is thus determined by the surface Si(OH)_x groups (defects) and not by confinement. This explains why defect sites influence the catalytic performance during methanol conversion on heterogeneous catalysts.

9. Influence of Confinement and Surface Sites on Water Adsorption

9.1 Introduction

Water is commonly present as a reactant, co-product or solvent in chemical reactions, especially in conversions of regenerative feedstocks. However, researchers have reported the presence of water on solid catalysts can crucially impact the performance achieved by heterogeneous catalysis. For example, in the decarbonylation of 5-hydroxymethylfurfural to furfuryl alcohol, the presence water can form hydrogen bonds with furfuryl alcohol. This prevents the further side reactions and increases the selectivity of furfuryl alcohol.^[191] If water is present, the reaction of cyclohexanol dehydration occurs on different routes, because the active acid sites change from bridge OH groups to hydronium ions.^[132] Another example is that traces of water on acidic H-ZSM-5 can facilitate the C-H activation rate, whereas higher water contents (> 2 water/BAS) retard it.^[131] For analysis, water titration combined with ¹H MAS NMR spectroscopy is typically used for investigating interactions between water and surface sites in zeolites. This approach enables the quantitative determination of formed surface complexes.^{[143],[192]} However, what is measured by this method is a clean surface instead of a “real” surface that has been contacted with water for several hours. This is important, as the long-time contact with water can break the Si-O-Si bonds and dissolve it into framework silica-oxygen tetrahedral with silanol groups, Si(OH), present on them.^[136] It is thus no surprise that the water-involving reactions that are observed normally occur in an imperfect zeolite. However, interaction of water with this partially etched surface is very seldom investigated in scientific investigations and mostly model systems are found.

The interactions of water with the surface of these materials is reflected by the chemical shift, δ_{1H} , of the protons on water molecules in the ¹H MAS NMR spectroscopy. For example, gaseous water not involved in hydrogen bonding has a chemical shift of $\delta_{1H} = 0.31$ ppm, whereas the formation of H-bonds amongst water molecules in the liquid state lead to a significantly higher chemical shift of $\delta_{1H} = 4.8$ ppm.^{[140],[141]} For detecting protons in fast exchange, *e.g.* water adsorbed at BAS, only an averaged signal is usually observed, despite the individual chemical shifts of water and BAS. This is because the exchange of protons occurs too fast to be distinguished by the traditional ¹H MAS NMR spectroscopy. The signal maximum of the averaged signal is determined by the proportion and the chemical shift of the individual species. Thus, a shift of the averaged signal maximum is visible if the ratio of the

9. Influence of Confinement and Surface Sites on Water Adsorption

different species is altered. Individual species in the coalescence signal can be separated at low temperatures by “freezing” proton exchange process.^[157] In addition, a sufficiently long distance between different species can disable this proton exchange. Therefore, in chapter 7, we monitor several individual signals after desorption of methanol from H-ZSM-5. For hydrated acidic zeolites, a broad signal with a signal maximum at around 5 to 7 ppm is typically observed when the surface is saturated with water. In this case what is seen is an averaged signal of water molecules adsorbed on Brønsted acid sites (BAS).^[193] This signal shifts to a low field area when the number of water molecules decrease to 9-2 water/BAS.^[143] No isolated hydronium ion (H_3O^+) has ever been experimentally observed and only theoretical calculation predicted a chemical shift of $\delta_{\text{1H}} = 12.7$ ppm. Furthermore, noteworthy signals of water on Lewis acid site (LAS) and $\text{Al}(\text{H}_2\text{O})_6^{3+}$ species are found at 6.5 and 9.2 ppm, respectively.^[194]

It is well known that nanoscale confinement impacts the physical and chemical properties of molecular aggregates. For water clusters in nanocavities, decreases in the dielectric constant, melting point, density and surface tension, as well as the increase of H-bonding strength, were reported by various authors.^[195-197] Theoretical studies of water adsorption on MFI zeolites reveal that steric restriction by confinement is to a larger extent responsible for water adsorption than the present surface sites.^{[180],[198]} Furthermore, the confinement also shows influences on catalysis. For example, a suitable pore structure can stabilize the transition states of reactants, which leads to higher catalytic rates than on unconfined analogs.^{[10],[199]} The different pore sizes of mesoporous MCM-41 and SBA-15 result in different hydration mechanisms present on both materials.^[175] These large pores are also possible to increase the H-bonding strength within water clusters.^[200] Besides porous materials, unconfined non-porous silica materials supporting active species are also commonly used as catalysts. For example, heteropoly acids (HPA), are commonly deposited on nonporous silica for ethanol dehydration to ethene.^{[201],[202]} In this way, acid sites can be introduced onto materials without introducing confinement in parallel. However, systematic and comparing studies of water adsorption on acidic mesoporous aluminosilicates and nonporous materials are still absent.

In this study, we systematically investigate the influences of confinement and surface sites on water adsorption, using identical materials and methods as chapter 8. The corresponding physicochemical properties of materials are summarized in table 8.1 and section 8.2. Upon desorption of water at elevated temperature, different surface species are quantitatively identified by solid-state NMR and DRIFTS spectroscopies. To explicitly explain the adsorbed species, the same symbols, “@”, “<” and “/” (see table 8.2) are likewise used in

this chapter. Finally, we find largely comparable desorption properties of water and methanol from identical solid materials.

9.2 Water on Siliceous Materials

Silicalite's initial water loading after saturating the surface with water is 0.54 mmol/g. This value is much lower than the loading of methanol on this material (2.5 mmol/g, section 8.3) due to the higher polarity of water compared with methanol (dipole moment of H₂O is 6.17×10^{-30} C m and that of methanol is 5.67×10^{-30} C m).^[203] In other words, the hydrophobic inner surface of Silicalite gives rise to a strong repulsive force to water molecules, restricting a high water capacity. Therefore, obvious signals of isolated Si(OH) groups already appear at 1.8-1.1 ppm directly after saturation (figure 9.1).^{[75],[204]} This indicates that these groups are not covered by water molecules. Similar to the methanol saturated Silicalite (section 8.3), the main signal at 3.5 ppm is an averaged signal of surface Si(OH) groups (at 1.8 ppm) and adsorbates (4.8 ppm) in fast exchange.^{[75],[141]} Considering the loading of 0.54 mmol/g is equal to 0.8 H₂O/Si(OH), we can approximate a 1:1 ratio between the two species. For supporting this and according to literature, a rough calculation of the averaged chemical shift could be performed: $\delta_{\text{IH}} = (2 \times (4.8 \text{ ppm}) + 1 \times 1.8 \text{ ppm})/3 = 3.8 \text{ ppm}$.^{[175],[194]} Keeping in mind that the stoichiometry is lower than 1 and that the proportion of Si(OH) sites participating in the proton exchange could be higher in the silanol nests, the calculation reasonably agrees with the experimental chemical shift of 3.5 ppm. If more water is adsorbed in Silicalite, the averaged signal shifts to the low field and causes a chemical shift close to that of liquid water.^[142] A slim peak at around 6.7 ppm was previously assigned to water adsorbed at Lewis acidic defects.^[194] Such a downfield shift does not exist when water is loaded on weak Lewis acid sites (LAS), e.g. Na⁺ cations, in the isostructural Na-ZSM-5 (section 9.3, figure 9.3). A more reasonable explanation of this signal is water adsorbed on silanol defects, whereby we reference to the previous chapter dealing with methanol adsorption (section 8.3). After desorption at 298 K, most of the water is removed except a trace amount of water at defects. This strongly bonded species is persistent until the desorption temperature is higher than 473 K. In addition, a background at ca. 3 ppm appears upon vacuum treatment. This signal is assigned to H₂O@Si(OH) species which persists in elevated temperatures.^{[205],[206]} The broad IR band in a range of 3600-2800 cm⁻¹ indicates the O-H stretching of hydrogen-bonded H₂O and Si(OH). Upon desorption, the peak of this broad signal gradually shifts to 3500 cm⁻¹, corresponding to the hydrogen-bonded silanol

9. Influence of Confinement and Surface Sites on Water Adsorption

nects.^{[166],[177]} Meanwhile, slim signals at 3725 cm^{-1} and 3680 cm^{-1} appear since the first desorption, representing the external and internal Si(OH) groups, respectively.^[166] This is in accordance with the appearance of the ^1H MAS NMR signal at 1.8 ppm at the same desorption steps.

In the mesoporous SBA-15, the water loading of 8.98 mmol/g is more than 15 times that found for Silicalite (0.54 mmol/g), determining a dominant chemical shift of 4.2 ppm in the ^1H MAS NMR spectrum. Because of the high $\text{H}_2\text{O}/\text{Si}(\text{OH})$ ratio, the chemical shift is much higher than that of Silicalite (3.5 ppm) and close to the chemical shift of liquid water (4.8 ppm).^[141] This signal is attributed to the liquid-like water species, $\text{H}_2\text{O} \leftrightarrow \text{H}_2\text{O}@\text{Si}(\text{OH})$, as supported by a previous assignment in literature.^[175] It is noteworthy that the chemical shift of 4.2 ppm is lower than that of the liquid-like methanol species in SBA-15 at 4.8 ppm (see section 8.3). Because, as observed by the ^{29}Si CP MAS NMR in section 7.3.1, the distance between H and Si atom on a Si(OH) is shorter after water adsorption and after methanol adsorption. Therefore, the chemical shift of water disturbed Si(OH) is lower than that of methanol disturbed one, resulted in a lower shift of the averaged signal. A weak shoulder appears at around 6.2 ppm. Grünberg et al. assigned a signal at a similar shift of 5.5 ppm to water clusters in mesopores.^[175] However, their explanation remains unclear on how water species (4.8 ppm) interacting with Si(OH) groups (1.8 ppm) could probably average to a signal at 5.5 ppm. The interaction with acid sites is also excluded because acid sites can be excluded to be present on the herein investigated siliceous SBA-15, as proven in section 6.4. However, we found that the amorphous surface in SBA-15, is rich in $\text{Si}(\text{OH})_2$ groups. Such groups play an important role in water adsorption (section 7.3.1), whereas such groups are widely absent on surfaces of herein investigated crystalline materials. Thus, the signal at 6.2 ppm is tentatively assigned to water adsorbed at amorphous defect sites. In contrast to the observation in Silicalite, the corresponding signal in SBA-15 is broad and it only exists after saturation. Thus, water at defects is less stable in amorphous SBA-15 than in Silicalite. Upon evacuation at room temperature (298 K) most of the water is already removed. The signal of Si(OH) groups at 1.8 ppm appears and is accompanied by a shoulder at around 3 ppm. The later signal has been explained by strongly bounded $\text{H}_2\text{O}@\text{Si}(\text{OH})$ species similar to Silicalite.^{[205],[206]} Results from DRIFTS measurement are in accordance with observations from ^1H MAS NMR. The broad IR band of O-H bonds appears at $3700\text{-}2600\text{ cm}^{-1}$ and narrows to $3700\text{-}3200\text{ cm}^{-1}$ after desorption at 348 K. Isolated external Si(OH) groups are present at 3745 cm^{-1} in all spectra and become increasingly intense upon desorption steps.

9. Influence of Confinement and Surface Sites on Water Adsorption

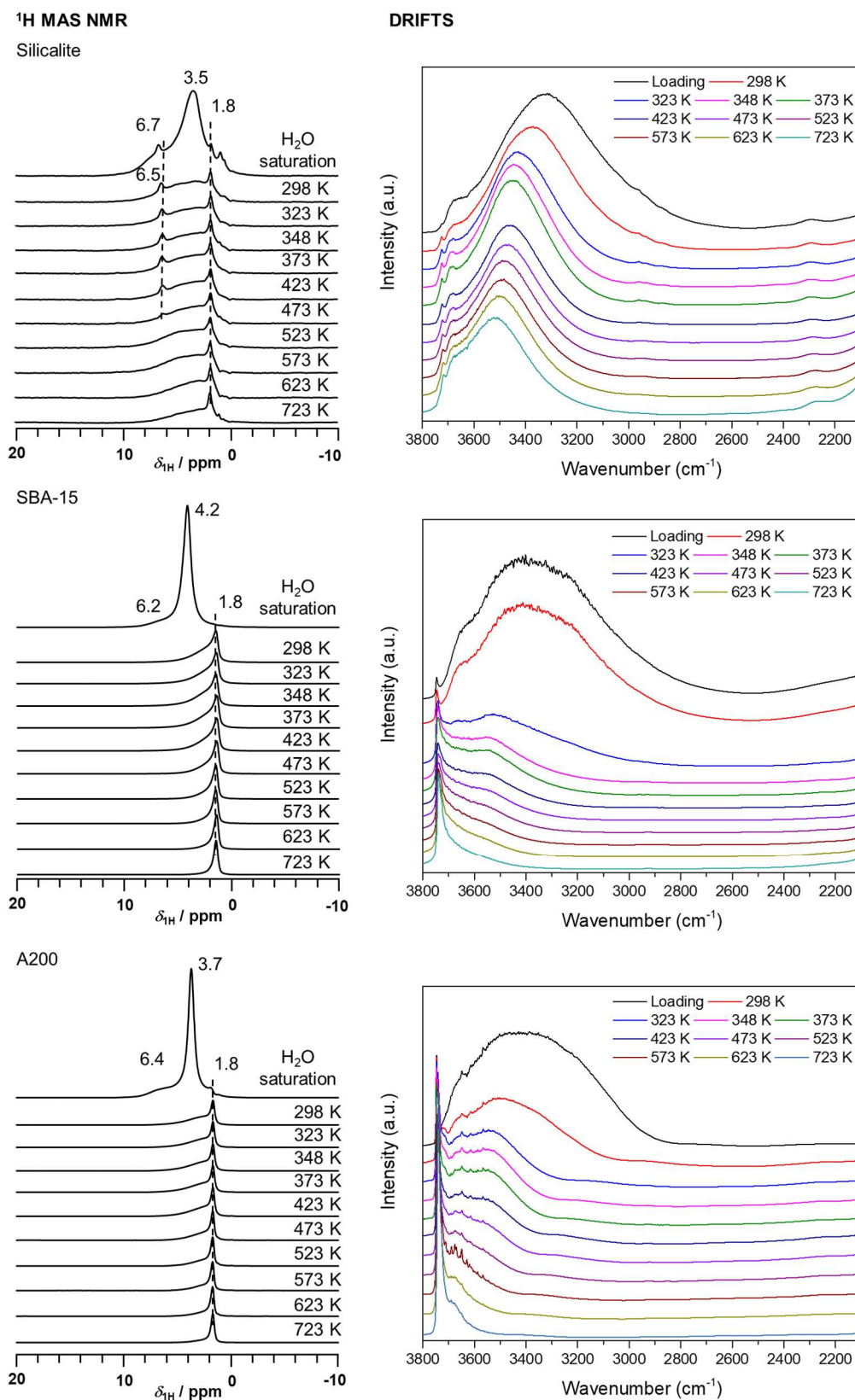


Figure 9.1 ^1H MAS NMR (left) and DRIFTS (right) spectra of water saturation at room temperature and desorption at elevated temperature on Silicalite, SBA-15 and A200 (from top to bottom).

9. Influence of Confinement and Surface Sites on Water Adsorption

Table 9.1: ^1H MAS NMR signal assignment for water H_2O loaded catalysts

$\delta_{1\text{H}}$ [ppm]	sample	Description	References
9.1 – 8.1	H-ZSM-5, H-STA@A200	$\text{H}_2\text{O} \leftrightarrow \text{H}_2\text{O}@\text{H}^+$, hydronium	[143], this study
6.8 – 6.0	Silicalite, H-ZSM-5, SBA-15, A200	stable at elevated temperature in Silicalite and H-ZSM-5 and explained by water on a Lewis-Acid or in a silanol nest; elsewhere only visible upon saturation	[194], this study
6.1 – 5.9	H-ZSM-5, H-STA@A200	Broad saturation peak of liquid-like water in interaction with acidic surfaces at 7-10 $\text{H}_2\text{O}/\text{H}^+$, broad IR bands between 3700 and 3400 cm^{-1}	this study
4.9 – 4.0	SBA-15 materials	Liquid-like water in weak interaction with the surface; the ratio between water and surface site protons determines the exact shift	[175],[193], [205],[207]
3.2 – 2.8	Na-ZSM-5, Na-[Al]SBA-15	Liquid-like or isolated $\text{H}_2\text{O} \leftrightarrow \text{H}_2\text{O}@\text{Na}^+$; shows distinct IR bands of hydration shells at 3660, 3476, and 3257 cm^{-1}	[142],[208], this study
4.0 – 2.3	Silicalite, H-ZSM-5, SBA-15, A200, STA materials	$\text{H}_2\text{O}@\text{Si}(\text{OH})$ (for silanol groups in hydrogen bonding: water/silanol ratio < 1); broad peak; also visible in materials with supported STA	[60],[193], [205]
0.3 – 0.8; 4.8	H_2O	Gas and liquid phase H_2O	[140-142]

The results of A200 are similar to that of SBA-15. The major signal locates at 3.7 ppm, which is in between the shifts found on Silicalite (3.5 ppm) and on SBA-15 (4.2 ppm). This is due to the fact that the $\text{H}_2\text{O}/\text{Si}(\text{OH})$ ratios increase in the order of Silicalite < A200 < SBA-15 (figure 9.2, right). A weak hump at ca. 6.4 ppm is again explained by water at defects. The signal of external $\text{Si}(\text{OH})$ groups at 1.8 ppm is present since the saturation step along with the corresponding IR band at 3745 cm^{-1} . The IR band at around 3680 cm^{-1} is attributed to the internal $\text{Si}(\text{OH})$ groups at defects, as previously reported for Silicalite.^[166]

A comparison of water contents on these three siliceous materials is shown in figure 9.2. The absolute quantity of SBA-15 (8.98 mmol/g) is remarkably higher than those of the other

9. Influence of Confinement and Surface Sites on Water Adsorption

two materials (< 1 mmol/g). This is explained by the large surface area of SBA-15, considering that all the materials have comparable Si(OH) densities of $1.9\text{--}2.5$ $\mu\text{mol}/\text{m}^2$. Besides, when the values are normalized by the surface areas or Si(OH) densities (figure 9.2, middle and right), SBA-15 is still the best in terms of maximum water adsorption. It is noteworthy that the highest water density (normalized by surface area) of SBA-15 indicates confinement of mesopores is more suitable for increasing the water loading than the micropores or the unconstrained surface. In other words, the size of mesopore is neither too small to cause a too strong interaction with the inner pore surfaces nor too large to cause weak interactions between water and adsorbents. This observation is different from methanol saturation, where the unconfined A200 performs the best (section 8.3). Thus, the silica surface prefers less polar adsorbates as methanol. Upon stepwise evacuation, most water is removed from the silica surface, and $\text{H}_2\text{O}/\text{Si}(\text{OH})$ ratios are lower than 1. SBA-15 still surpasses the other materials in absolute water quantities. However, when the values are corrected by surface areas and surface sites, A200 contains comparable water as SBA-15. Therefore, the large surface area is dominant for water persistence if the density of Si(OH) defect sites are almost equal. However, confinement of micropores is detrimental to water retention due to the strong repulsive effect.

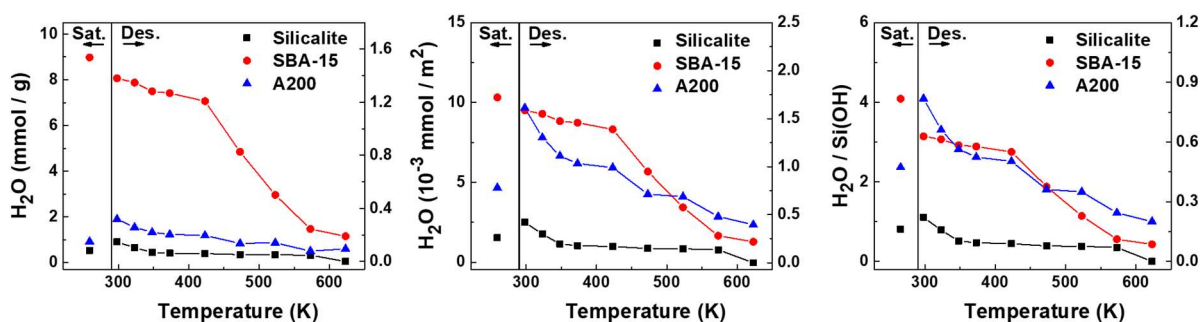


Figure 9.2 Water quantities on siliceous materials, plotting in absolute quantities per mass (left), in absolute quantities per surface area (middle), and in the ratio of $\text{H}_2\text{O}/\text{Si}(\text{OH})$ (right). The results are from quantitative ^1H MAS NMR measurements with an external standard.

9.3 Water on Na-form Materials

In the following Na-form materials are discussed similarly to the siliceous forms and relative ^1H MAS NMR and DRIFTS spectra are shown in figure 9.3. The hydrophilic Na-ZSM-5 adsorbs 3.95 mmol/g water ($6.6 \text{ H}_2\text{O}/\text{Na}^+$) in its micropores. This is much higher than in hydrophobic Silicalite. The initial ^1H MAS NMR signal at 3.2 ppm indicates a $\text{H}_2\text{O} \langle \rangle \text{H}_2\text{O}@\text{Na}^+$ species, because water is adsorbed at Na^+ cations in Na-ZSM-5, as confirmed in section 7.3.2. Compared to the chemical shift of liquid water, the lower chemical shift of this species is attributed to the presence of Na^+ cations that weakens the hydrogen bond between water molecules.^[142] The signal broadens and shifts to around 2.6 ppm upon water removal, indicating a changing stoichiometry between water and surface site. After desorption at 423 K, most water is evacuated and the loading declines to 0.19 mmol/g. The signal at 1.8 ppm appears at this temperature, indicating the few Si(OH) groups on Na-ZSM-5. Meanwhile, the aforementioned signal at 2.6 ppm splits into two individual signals at 3.2 ppm and 2.3 ppm, respectively. The downfield one is at 3.2 ppm and again assigned to $\text{H}_2\text{O} \langle \rangle \text{H}_2\text{O}@\text{Na}^+$. Because the upfield signal (at 2.3 ppm) decreases accompanied by an increase of signal intensity at 1.8 ppm in the next desorption steps, it must be associated with the trace amount of Si(OH) groups. However, the chemical shift is lower than the 3.5 ppm of $\text{H}_2\text{O}@\text{Si}(\text{OH})$, that was observed on Silicalite with $\text{H}_2\text{O}/\text{Si}(\text{OH})$ equal to 1. This observation could be due to the introduction of hydrogen bonds between $\text{H}_2\text{O}@\text{Na}^+$ species and Si(OH) groups, *i.e.* the water molecule is adsorbed at Na^+ species. It could also be explained by the $\text{H}_2\text{O}@\text{Si}(\text{OH})$ species near a Na^+ cation, *i.e.* the water molecule is adsorbed at a silanol group. Considering the binding sites are Na^+ cations in Na-ZSM-5, the first assumption is more likely than the second. The DRIFTS spectra support the ^1H MAS NMR spectra. Three IR bands are initially present at 3257, 3475 and 3660 cm^{-1} . These signals indicate the core-shell structure of the $\text{H}_2\text{O} \langle \rangle \text{H}_2\text{O}@\text{Na}^+$ species.^[208] The IR band at 3257 cm^{-1} is attributed to the peripheral water molecules, which disappears upon desorption at elevated temperatures. The IR band at 3475 cm^{-1} is in the range of hydrogen binds of water. It shifts to high wavenumbers during water desorption and after the treatment at 423 K. The IR band at 3660 cm^{-1} splits into to IR bands at 3598 and 3663 cm^{-1} after desorption at 298 K. In accordance with the literature, these two bands are the symmetric and asymmetric stretches of H_2O adsorbed at Na^+ cation, respectively.^[208]

9. Influence of Confinement and Surface Sites on Water Adsorption

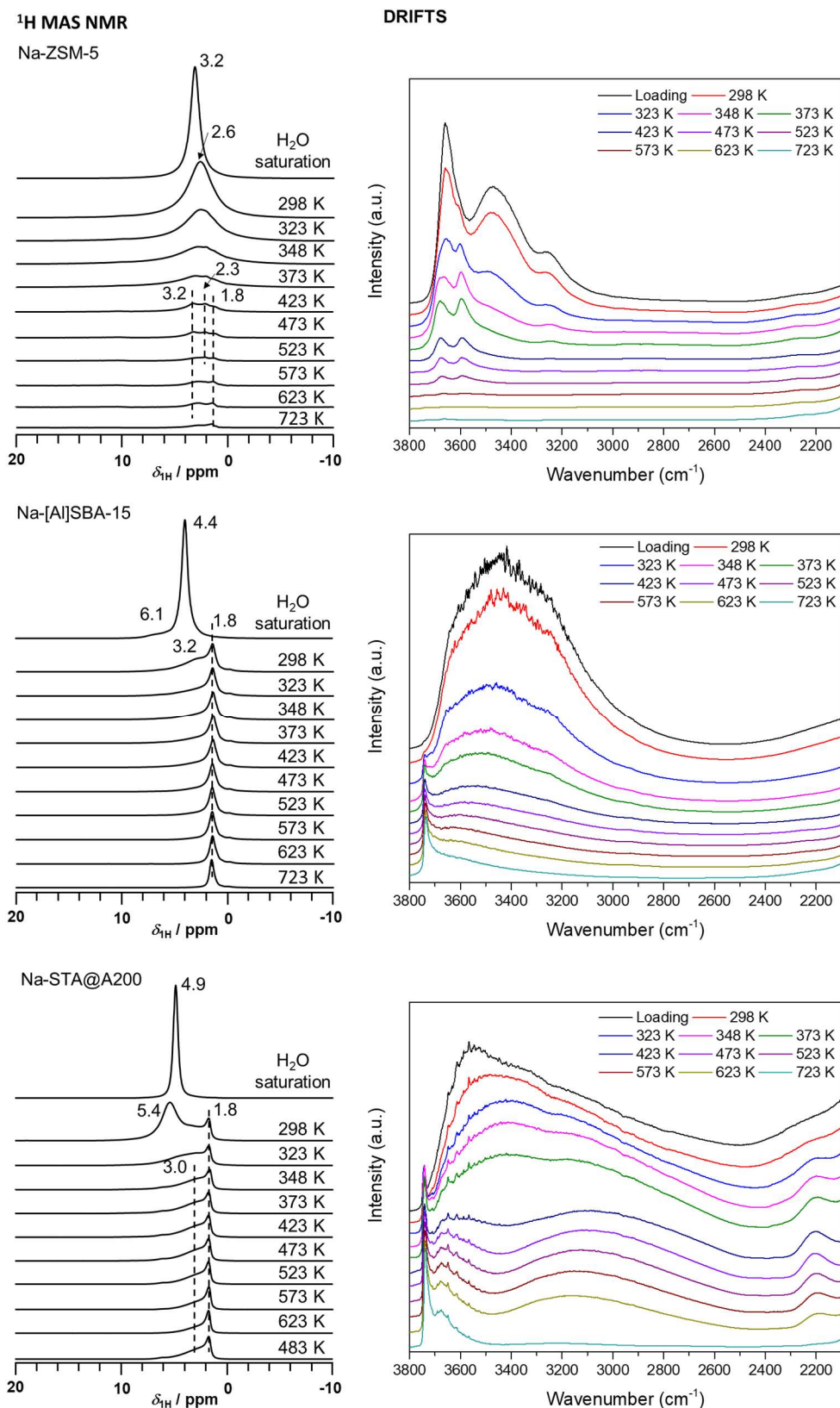


Figure 9.3 ^1H MAS NMR (left) and DRIFTS (right) spectra of water saturation at room temperature and desorption at elevated temperature on Na-ZSM-5, Na-[Al]SBA-15 and Na-STA@A200 (from top to bottom).

9. Influence of Confinement and Surface Sites on Water Adsorption

On the mesoporous Na-[Al]SBA-15, the saturation loading reaches 7.33 mmol/g water. Due to the high water content, a liquid-like water species is present in the mesopores. It has a chemical shift at 4.4 ppm, close to that of liquid water at 4.8 ppm. The lower chemical shift is due to the presence of Na⁺ (0.86 mmol/g) and Si(OH) groups (1.14 mmol/g) as described in Na-ZSM-5 and SBA-15, respectively. It is noteworthy that the saturated water adsorption of Na-[Al]SBA-15 is lower than that of SBA-15 (8.98 mmol/g), whereas the water density (water per surface area) of the Na-form (ca. 15 $\mu\text{mol}/\text{m}^2$) is 50% higher than that of the siliceous form (15 $\mu\text{mol}/\text{m}^2$). Considering their comparable density of surface sites (2.0 mmol/g of Si(OH)+Na⁺ for Na-[Al]SBA-15 and 2.2 mmol/g Si(OH) for SBA-15), the increased surface hydrophilicity must be associated with the high density of binding sites or/and the presence of Na⁺ cations. Upon vacuum treatment at 298 K, the Si(OH) signal appears at 1.8 ppm with a broad shoulder at ca. 3.2 ppm. The later signal could be assigned to H₂O \leftrightarrow H₂O@Na⁺ or/and H₂O@Si(OH). However, the chemical shifts of the two species are too close to each other and are impossible to distinguish. This signal almost vanishes after desorption at 323 K. In other words, the H₂O \leftrightarrow H₂O@Na⁺ species is either absent or decomposes before 323 K in Na-[Al]SBA-15. This observation differs from the aforementioned H₂O \leftrightarrow H₂O@Na⁺ present on Na-ZSM-5, which persists even after 573 K. This indicates that the water-Na⁺ complexes are more stable in micropores than in mesopores, explainable by the microporous confinement effect similar to that for methanol (section 8.4). The DRIFTS spectra initially show a broad IR band in the range of 2700-3700 cm⁻¹. It indicates that the liquid-like species dominates in the water-saturation state, which is in good agreement with the signal at 4.4 ppm found in the ¹H MAS NMR spectrum. The IR band of Si(OH) appears at 3740 cm⁻¹ after desorption at 298 K. This IR band is gradually enhanced after desorption at elevated temperatures, which implies water is continuously released from Si(OH) groups. After 323 K, a signal at 3200-3300 cm⁻¹ appears, indicating the presence of the H₂O \leftrightarrow H₂O@Na⁺ species as discussed previously in Na-ZSM-5 and in the literature.^[208] However, this signal is weaker than that in the Na-ZSM-5, which indicates that most water does not coordinate at Na⁺ cations but at Si(OH) groups in Na-[Al]SBA-15. This again agrees well with the finding in section 7.3.2 for methanol adsorption on the same material, Na-[Al]SBA-15.

The non-porous Na-STA@A200 material contains 0.25 mmol/g Na⁺ and 0.57 mmol/g Si(OH) groups on the surface. The water capacity at saturation is 2.90 mmol/g. A chemical shift of 4.9 ppm in the ¹H MAS NMR spectrum again indicates a liquid-like species. However, the shift is higher than that on the aforementioned Na-form materials and liquid water, which

9. Influence of Confinement and Surface Sites on Water Adsorption

is explained by the existence of a trace amount of BAS (0.09 mmol/g) on the Na-STA@A200 material. The individual BAS on STA@A200 usually have a higher chemical shift at around 9.1 ppm (see the next section, H-STA@A200). When BAS are involved in the proton exchange with water molecules, this usually leads to a higher chemical shift of the averaged signal. The signal shifts to 5.4 ppm, after evacuation at room temperature (298 K), due to the removal of liquid-like water. This observation confirms the high-chemical-shift species, *i.e.* H⁺ cations, must be involved in the proton exchange with liquid-like water. Other surface sites (Si(OH) and Na⁺) lead to an upfield shift as described for siliceous materials and Na-ZSM-5, respectively. Upon desorption at elevated temperatures, the usual Si(OH) signal appears at 1.8 ppm. Meanwhile, a weak hump at ca. 3.0 ppm indicates the strongly bonded H₂O@Si(OH) species as in siliceous materials (section 9.2). It must be noted that the signal of pure BAS upon desorption is not present in ¹H MAS NMR spectra due to its low quantity. In the DRIFTS measurements, the broad IR band initially shown up between 2600 and 3700 cm⁻¹ is mainly attributed to the hydrogen-bonded water.^[209] After water desorption at 298 K, a Si(OH) band appears at 3741 cm⁻¹. However, no visible IR band is associated with the H₂O@Na⁺ complex as previously found on Na-ZSM-5. This indicates the weak stability of such species on the unconfined Na-STA@A200. A broad band appears at 3400-2500 cm⁻¹ after the treatment at 423 K, and it suddenly disappears again at 723 K. This IR band does not appear on A200. Thus, considering it is located in the range of the OH stretching vibration, this broad IR band is tentatively assigned to water bound at Keggin units of the STA. Such a species has been reported for other supported heteropoly acids.^[210] The IR band corresponds to the ¹H MAS NMR signal at 3.2 ppm, which does not appear on the A200 material.

As for the siliceous materials, also here comparisons of water contents in the absolute quantity, water density and water per Na⁺ site are conducted to investigate the confinement effect on water capacities for Na-form materials (figure 9.4). The mesoporous Na-[Al]SBA-15 outperforms the microporous and non-porous analogs in absolute water amounts after saturation. However, when the water contents are normalized by surface areas, the highest water density is observed on the non-porous Na-STA@A200. This differs from the observations on siliceous materials, where mesoporous SBA-15 exhibit the highest water density. This difference between siliceous and Na-form materials could be explained by one or both of the following two reasons: (1) Considering that the main binding sites on Na-[Al]SBA-15 and Na-STA@A200 are Si(OH) groups, the higher Si(OH) density (Na-STA@A200, 4.75 μmol/m²; Na-[Al]SBA-15, 2.18 μmol/m²) leads to the higher water density in the saturation

9. Influence of Confinement and Surface Sites on Water Adsorption

step. (2) Compared to siliceous forms, The surfaces in Na-forms are more polar, which causes higher water density when the confinement is less. Upon desorption at elevated temperatures, especially at temperatures higher than 348 K, Na-[Al]SBA-15 is again the best water catcher. The microporous confinement of Na-ZSM-5 only contributes to water retention at low temperatures (< 323 K), whereas Na-ZSM-5 performs worse at higher temperatures, both regarding the absolute water contents and the contents corrected by the surface area and number of Na^+ sites, respectively. As discussed above and in section 7.3.2, water mainly adsorbs at Na^+ cations on Na-ZSM-5, whereas water mostly interacts with $\text{Si}(\text{OH})$ on Na-[Al]SBA-15 and Na-STA@A200. Therefore, the binding strength of water at Na^+ in micropores is weaker than that of surface $\text{Si}(\text{OH})$ groups. In other words, although micropores stabilize the $\text{H}_2\text{O}@\text{Na}^+$ complexes, the stabilized water- Na^+ species is still weaker than water bound at some $\text{Si}(\text{OH})$ groups.

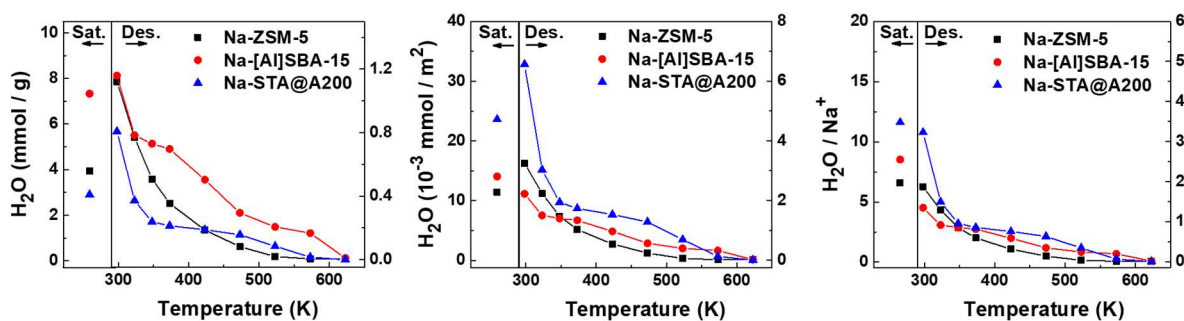


Figure 9.4 Water quantities on Na-form materials, plotting in absolute quantities per mass (left), in absolute quantities per surface area (middle), and in the ratio of $\text{H}_2\text{O}/\text{Na}^+$ (right). The results are from quantitative ^1H MAS NMR measurements with an external standard.

9.4 Water on H-form Materials

Finally, we come to the acidic H-form materials. Microporous H-ZSM-5 initially adsorbs 3.78 mmol/g of water (equals to 7.7 H₂O/H⁺), which is comparable to the loading on the Na-ZSM-5 (3.95 mmol/g, 6.6 H₂O/Na⁺). The corresponding ¹H MAS NMR signal is found at 5.9 ppm (figure 9.5). Taking the H₂O/H⁺ ratio into account, this signal is assigned to the liquid-like water species. Similar to water adsorption on Na-STA@A200 (section 9.4), the chemical shift is here higher than that of pure liquid water (4.8 ppm) and water saturated on Na-ZSM-5 (3.2 ppm). This is the case because the proton exchange process in H-ZSM-5 involves the acidic BAS (0.49 mmol/g) that have a high chemical shift.^[157]

Upon desorption at 298 K, only 0.69 mmol/g water remains on H-ZSM-5 and the initial signal splits into a peak manifold with signals at 9.0, 6.8, 3.5 and 1.8 ppm. This observation indicates the primary proton exchange consists of water and different surface protons, a finding that is supported by the broad IR bands between 2600 to 3700 cm⁻¹ in the DRIFTS measurement. The signal at 9.0 ppm is assigned to H₂O <> H₂O@H⁺ species. It shifts upfield to 8.6 ppm after desorption at 373 K. This is explained by the variation of the water contents at H⁺ sites. In the literature, a similar change of chemical shift was observed when the H₂O/H⁺ ratio decreased from 5 to 2.^[143] It is worth noting that this H₂O <> H₂O@H⁺ signal is more intense in our measurements than theirs. This is due to the different experimental procedures. Our samples are firstly equilibrated at saturated vapor pressure for more than 24 h and then evacuated at elevated temperatures, whereas their measurements were performed directly after adsorbing water at ambient humidity. The long equilibration time in our method leads to the formation of more H₂O <> H₂O@H⁺ complexes that is only partially reversible.^[208] In the subsequent desorption steps, weakly bounded water are removed, whereas the stable H⁺(H₂O)_n clusters remain, leading to a clear signal in the ¹H MAS NMR spectra. Wang et al. also predicted the averaged chemical shift of H⁺(H₂O)_n via the density functional theory (DFT) calculations, where the chemical shifts are found at 8.2 and 8.5 ppm in case of n = 3 and 4, respectively.^[143] A signal located at 6.8 ppm was assigned to be a surface species associated with BAS or LAS.^{[193],[194]} It maintains a stable chemical shift during water removal at 523 K, indicating a constant H₂O/site ratio and higher stability than the aforementioned H₂O <> H₂O@H⁺ species. This observation reminds of the signal at 6.7 ppm found in Silicalite (figure 9.1 top). Therefore, this signal is assigned to water binding at the defect sites or silanol nests. However, due to the presence of Al in the H-ZSM-5 sample, we cannot rule out the possibility of water binding at LAS, as described in the literature.^[194] The signal of H₂O@Si(OH) appears at 3.5 ppm, as

9. Influence of Confinement and Surface Sites on Water Adsorption

discussed for Silicalite. Noted that this signal is absent in the adsorption measurement and a broad signal at ca. 6.8 ppm gradually enhances instead (The signal at 6.8 ppm in their work is attributed to the $\text{H}^+(\text{H}_2\text{O})_n$ species, because the broadness of it indicates a high mobility of this species. This is different from the $\text{H}_2\text{O}@$ defects species in our study).^[143] This observation points out the difference between water adsorption and desorption measurements. For the water adsorption method, water prefers to directly form large clusters with H^+ cations, resulting in a broad ^1H MAS NMR signal covers the signal of minor species, such as $\text{H}_2\text{O}@$ defects. While the desorption method can give a clear distinction on specific species. Uncovered $\text{Si}(\text{OH})$ groups are also present since the room-temperature evacuation and show a signal at 1.8 ppm in ^1H MAS NMR and an IR band at 3717 cm^{-1} .

After further desorption at 373 K, a signal of $\text{H}_2\text{O} \leftrightarrow \text{H}_2\text{O}@\text{H}^+$ disappears and uncovered bridging OH groups suddenly appear at 3.8 ppm. Meanwhile, the corresponding IR band located at 3605 cm^{-1} appears at the expense of bands at ~ 2900 and $\sim 2500\text{ cm}^{-1}$, respectively. The latter two bands are associated with perturbed $\text{Si}(\text{OH})\text{Al}$ groups in a low water loading.^{[209],[211]} The abrupt presence of BAS indicates that the hydronium ion is not stable in zeolites, which supports the finding from literature.^[143] In summary, in H-ZSM-5 most signals that we find are associated with protonated water species.

9. Influence of Confinement and Surface Sites on Water Adsorption

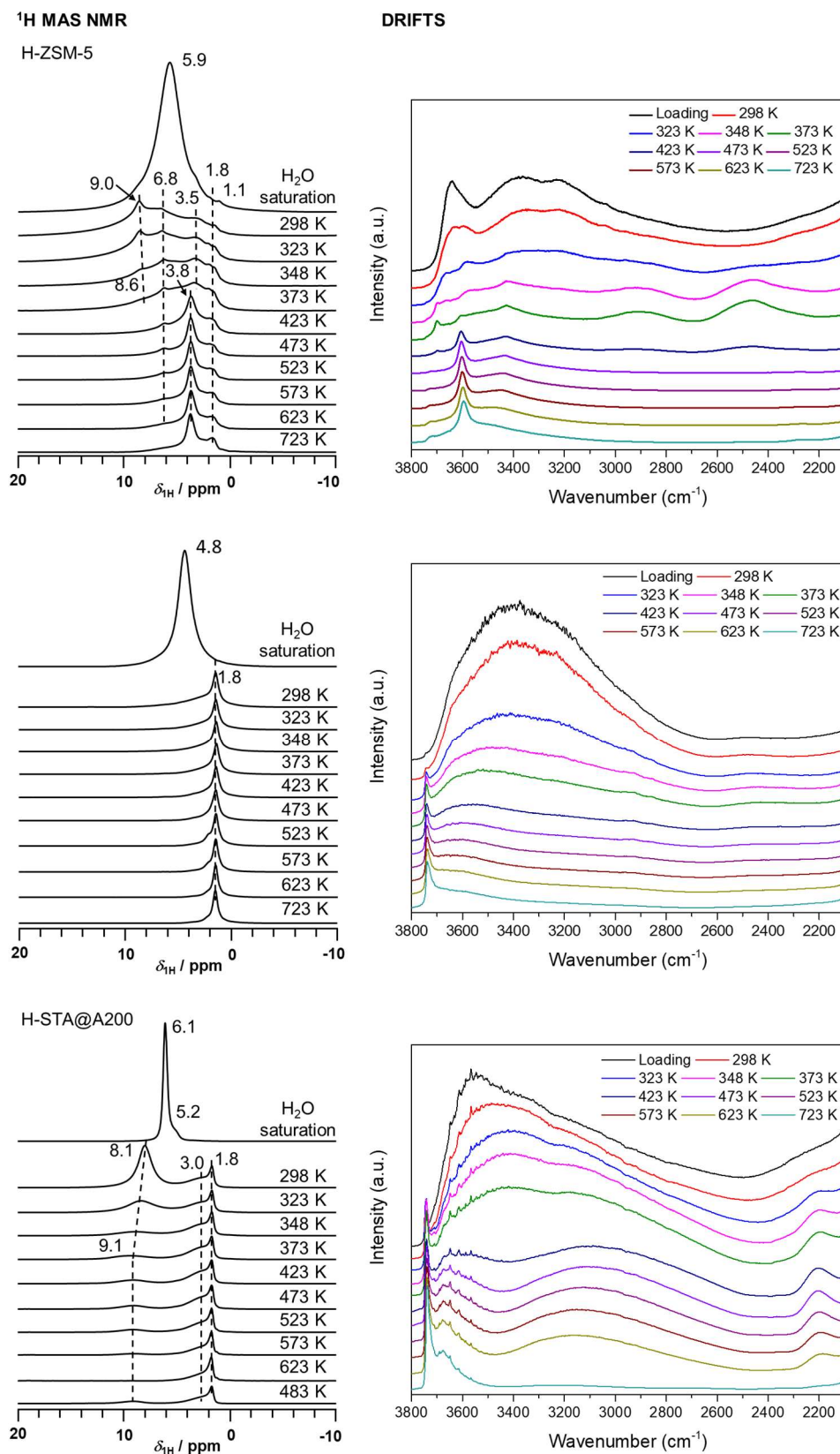


Figure 9.5 ^1H MAS NMR (left) and DRIFTS (right) spectra of water saturation at room temperature and desorption at elevated temperature on H-ZSM-5, H-[Al]SBA-15 and H-STA@A200 (from top to bottom).

9. Influence of Confinement and Surface Sites on Water Adsorption

In the water-saturated state, mesoporous H-[Al]SBA-15 is able to take in 6.18 mmol/g water. The ^1H MAS NMR causes a chemical shift at 4.8 ppm (figure 9.5, middle). It is noteworthy that the equivalent chemical shift with liquid water does not mean the surface species are pure water. It is because both BAS (0.19 mmol/g) and Si(OH) (0.59 mmol/g) on H-[Al]SBA-15 are involved in the proton exchange with water clusters. Therefore, like other SBA-15 materials, this signal is assigned to liquid-like species at the high water loading. The liquid-like water clusters cause a vast IR band in $2600\text{-}3700\text{ cm}^{-1}$. Upon the first desorption step, most of the water is removed and the signal of the bare Si(OH) groups appears at 1.8 ppm in the ^1H MAS NMR spectrum, accompanied by the corresponding band at 3741 cm^{-1} in the DRIFTS spectrum. The broad downfield shoulder at 2-5 ppm indicates the strongly bonded water species with the amorphous silica surface.^[175] However, protonated species as in H-ZSM-5 are not observed on H-[Al]SBA-15. This is explained by the weak acid strength of BAS formed by the flexible coordination, as previously discussed in section 6.4. It is worth noting that no aluminum-related signal is found in adsorption and desorption measurements despite the presence of aluminum sites, especially those in pentahedral or octahedral coordination (see figure 7.3). Therefore, we can conclude that Si(OH) groups are the major binding sites for water in H-[Al]SBA-15.

On H-STA@A200, a loading of 3.48 mmol/g is reached in the water-saturated state. In the corresponding ^1H MAS NMR spectrum (figure 9.5, bottom), the main signal is slim and located at 6.1 ppm. This signal is caused by the liquid-like H_2O in fast exchange with BAS on STA. A weak upfield shoulder appears at 5.2 ppm, associated with H_2O adsorbed at the silica support. The difference in signal intensities of these two signals indicates most water is adsorbed on the strong solid acid, STA, and only about 5% of water is adsorbed on the A200 support. The room-temperature evacuation removes 83% of the total water content and the remaining 0.60 mmol/g water causes two signals at 8.1 and 3.0 ppm. The downfield signal at 8.1 ppm is assigned to $\text{H}_2\text{O} \leftrightarrow \text{H}_2\text{O}@\text{H}^+$ species, as in case of H-ZSM-5. In the following desorption steps, water is gradually removed from BAS and the signal at 8.1 ppm further shifts downfield until the signal of bare BAS becomes visible at 9.1 ppm.^[60] The upfield signal is similarly observed as on pure A200 material and is attributed to $\text{H}_2\text{O}@\text{Si(OH)}$. Isolated Si(OH) groups appears upon the first desorption step as a signal at 1.8 ppm and a band at 3741 cm^{-1} in ^1H MAS NMR and DRIFTS, respectively. The retention of $\text{H}_2\text{O} \leftrightarrow \text{H}_2\text{O}@\text{H}^+$ at up to 373 K indicates the higher water affinity of strong BAS compared to the affinity of weak BAS in H-[Al]SBA-15. In addition, the absence of confinement, when compared to H-ZSM-5, explains

9. Influence of Confinement and Surface Sites on Water Adsorption

the faster decomposition of $\text{H}_2\text{O} \rightleftharpoons \text{H}_2\text{O}@\text{H}^+$ clusters. In other words, confinement can stabilize the protonated water complexes as was previously observed for Na^+ counter ions.

A detailed comparison of the water content on H-form materials in saturation and stepwise desorption is shown in figure 9.6. The mesoporous H-form, H-[Al]SBA-15, adsorbs the most water in saturation, which is attributed to the large surface area and similar to the aforementioned siliceous and Na-form materials. When water contents are normalized by the surface area, H-STA@A200 surpasses H-[Al]SBA-15. Similar to Na-form materials, this observation can be rationalized by the higher Si(OH) density on H-STA@A200 ($4.75 \mu\text{mol}/\text{m}^2$) compared to that on H-[Al]SBA-15 ($1.33 \mu\text{mol}/\text{m}^2$) or/and the preference of water adsorption on the unconfined and polarized surface. Here, the plot of $\text{H}_2\text{O}/\text{H}^+$ (figure 9.6, right) is meaningless because the weak BAS on H-[Al]SBA-15 has a negligible effect on water desorption. During the whole desorption process, H-[Al]SBA-15 contains more water than H-ZSM-5 and H-STA@A200. This reveals that Si(OH) groups bind water more strongly than BAS, when it comes to maintaining water in vacuum. In addition, water contents on H-ZSM-5 and H-STA@A200 are more or less comparable, although the micropores in H-ZSM-5 stabilize the $\text{H}_2\text{O} \rightleftharpoons \text{H}_2\text{O}@\text{H}^+$ species. This supports again the significant role of Si(OH) groups.

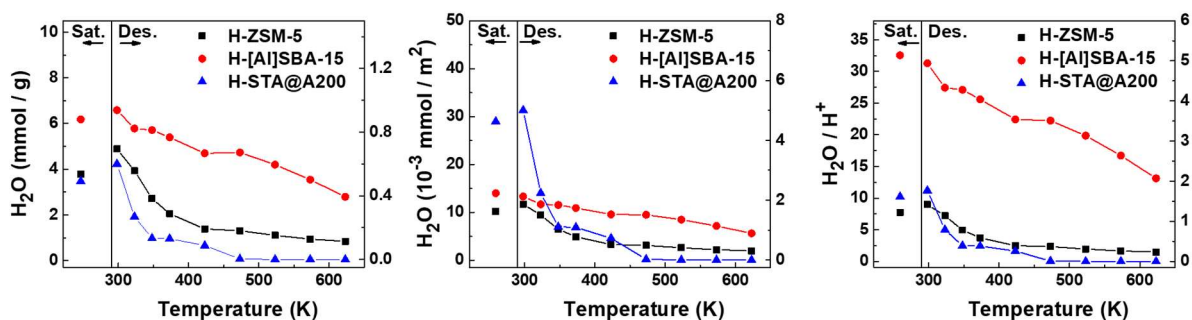


Figure 9.6 Water quantities on H-form materials, plotting in absolute quantities per mass (left), in absolute quantities per surface area (middle), and in the ratio of $\text{H}_2\text{O}/\text{H}^+$ (right). The results are from quantitative ^1H MAS NMR measurements with an external standard.

9.5 Influence of Material Surface Groups and Confinement and Comparing with Methanol Adsorption

To overview the influencing factors of binding sites and confinement, we summarize the absolute water contents of nine solid materials in the saturation state as well as in several chosen desorption steps (figure 9.7). In addition, we also herein compared these results with the corresponding methanol contents discussed in section 8.6 in order to explain the impact of the adsorbate itself. This comparison is worthwhile because methanol is a good model for other alcohols. And conversions of alcohols, such as methanol-to-olefins (MTO), are always accompanied by water as a by-product or co-feed.^{[212],[213]}

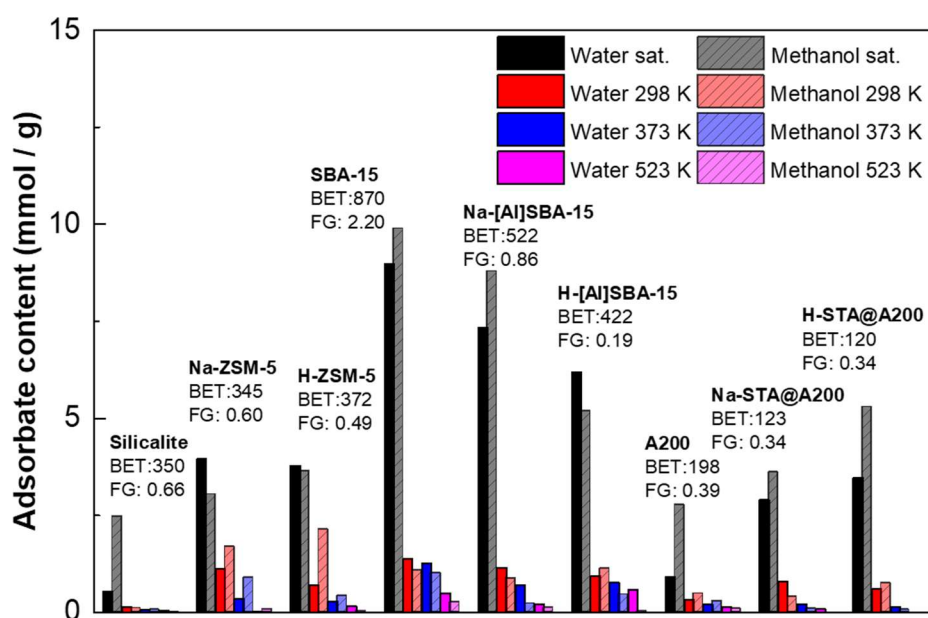


Figure 9.7 Water quantities of materials with different surface sites and confinement at chosen desorption steps. From left to right: microporous MFI zeolites, mesoporous SBA-15 materials, and non-porous A200 supported STA. The unit of the BET surface area (BET) is m²/g and the quantities of functional groups (FG) are given in mmol/g. The mentioned functional groups are Si(OH) for siliceous materials, Na⁺ for Na-form materials, and H⁺ for H-form materials.

In water adsorption, the mesoporous SBA-15 materials, especially the siliceous SBA-15, surpass other microporous and non-porous materials. In saturation, liquid-like water species form in these materials. Thereby water molecules mostly interact with each other instead of with the surface groups. Materials with larger surface areas and pore volumes are able to carry more water molecules. The only exception is Silicalite. In this material, liquid-like water is

9. Influence of Confinement and Surface Sites on Water Adsorption

absent and the saturated water content is the lowest, although its surface area is higher than that of A200 materials. This is explained by the strong confinement in microporous Silicalite, causing a repulsive effect on the polar molecule as mentioned in section 9.2. Besides the major influence of surface area, surface sites also show an impact on water adsorption. Each series of materials for MFI-type zeolites and A200 materials have comparable surface areas. However, water contents in the siliceous forms are lower than those of their isostructural Na- and H-forms. This trend applies equally to SBA-15 materials, if the water contents are normalized by surface areas. The water density of SBA-15 is $10.3 \mu\text{mol}/\text{m}^2$, which is lower than those of Na- and H-[Al]SBA-15 of $\sim 14.0 \mu\text{mol}/\text{m}^2$ (figure 9.2, 9.4 and 9.6). Upon evacuation at 298 K, most water has been removed from the solid materials. In this condition, SBA-15 materials again outperforms MFI-type zeolites and A200 materials. Na-ZSM-5 now maintains comparable amounts of water molecules as the SBA-15 materials. However, it is worth noting that the binding sites of Na-ZSM-5 are the confined Na^+ cations, whereas the binding sites of SBA-15 materials are Si(OH) groups. Further desorption at 373 K leads to a sudden drop in the water content of Na-ZSM-5 due to the decomposition of water/ Na^+ complexes. In contrast, for SBA-15 materials, Si(OH) groups still bind some water molecules even up to 523 K, which means that the Si(OH) groups are the stronger adsorption sites than Na^+ or H^+ cations.

The behaviour of water and methanol in saturation and desorption are similar in most materials. For Silicalite, the methanol content is higher than the water content found in the saturation step. This is explained by a stronger repulsive effect for water than methanol, since water is more polar than methanol.^[203] The saturation contents of water and methanol are similar in Na-ZSM-5 and H-ZSM-5. However, the methanol quantities are obviously higher than water quantities after desorption at elevated temperatures, although the boiling temperature of methanol is lower than water. It indicates methanol binds more strongly at counter ions (Na^+ or H^+) than water under the confinement of micropores. This observation explains why methanol conversion continuously processes without the deactivation by the generated by-product, water. For most SBA-15 and A200 materials, more methanol is adsorbed than water in saturation, because Si(OH) groups are dominant in these materials. However, H-[Al]SBA-15 is out of the tendency and adsorbs more water than methanol. This is probably associated with lots of extra-framework aluminum generated during the alumination process, improving the water-surface interaction. In contrast to adsorption, there is no certain trend in retaining water and methanol from the less confined SBA-15 and A200 materials.

9.6 Conclusions

In summary, we quantitatively investigated the water adsorption and desorption process on different surface sites and under different confinements. For most materials, saturation water loadings are dominantly affected by the surface area. Therefore, SBA-15, with the largest surface area of 870 m²/g, holds the most water molecules in the saturation step. When water contents are shown in water per surface area, it clearly indicates the presence of counter ions, such as Na⁺ or H⁺, is beneficial for water adsorption due to the polarization of the surface. It is worth noting that the strong confinement in Silicalite's micropores avoids the formation of water clusters and thus causes the lowest water saturation content. In contrast, mesopores in silica materials can promote water saturation. For Na- and H-form materials, the micropores in Na-ZSM-5 or H-ZSM-5 stabilizes the water-cation. Interestingly, even without confinement, most water is adsorbed on the Keggin units of STA materials. Upon desorption, Si(OH) groups bind water molecules strongly. A broad variety of water species is found and assigned throughout the water desorption from H-ZSM-5.

The saturation and desorption of water behave very similar to those of methanol. In the saturation, large surface areas with lots of Si(OH) groups favor the high loadings of adsorbate. The stability of adsorbate-cation complexes is determined by the microporous confinement. However, due to the lower dipole moment of the methanol molecule, *i.e.* the lower polarity, its content is higher than that of water in the saturated state on Silicalite and A200. In addition, in Na-ZSM-5 and H-ZSM-5, the surface-adsorbate interaction is stronger for methanol than for water. This interprets why acid sites are not deactivated by water in MTO reactions.

10. Conclusions and Outlook

The present work focuses on the alumination of porous silica materials with sodium aluminate and investigates the mechanism of alumination process, the acid properties of aluminated materials, the binding sites and binding energies of water and methanol on the parent silica and aluminated materials, and the influences of confinements and surface sites on water and methanol adsorption.

During the alumination process, the silica surface is partially dissolved in alkaline NaAlO₂ solution, forming Si(OH)_x groups (x = 1 to 3). Then NaAlO₂ reacts with some of these silanol groups and forms the tetrahedral aluminum known as framework aluminum. The alumination performance depends on the concentration of NaAlO₂ solution, the temperature and the pore structure of parent silica materials. The generated Na-form materials are good ion exchangers and more than 99% Na⁺ can be exchanged by NH₄⁺. However, only some (< 20%) of NH₄⁺ cations can transfer into Brønsted acid sites (BAS), due to the formation of extra-framework aluminum upon calcination. In mesoporous materials, the strength of BAS is weak, because of the flexible aluminum coordination with Si(OH) groups. Whereas the post-formed BAS in microporous DeA-Y zeolite are as strong as the directly synthesized one. In this research, TMPO loading combined with ³¹P MAS NMR a successful distinguish of different types of Brønsted and Lewis acid sites on acidic materials.

The binding sites and binding energies of water and methanol on siliceous and aluminated materials with different confinements are studied by MAS NMR spectroscopy and TGA-DSC analysis. For siliceous Silicalite and SBA-15, Si(OH) groups are determined as the main adsorption sites by ²⁹Si CP MAS NMR measurements. In microporous Na-ZSM-5, Na⁺ cations are the binding sites of water and methanol with desorption heats of 66-74 kJ/mol. In contrast, Si(OH) groups instead of Na⁺ are the dominant adsorption sites in Na-[Al]SBA-15. The desorption heats of water and methanol in this material are 44-60 kJ/mol. For acidic solids like H-ZSM-5, BAS are normally known as adsorption sites. However, we found water and methanol are mainly adsorbed on Si(OH) groups of H-[Al]SBA-15, as in the case of Na-[Al]SBA-15.

MAS NMR and IR spectroscopies were applied to investigate how confinements and surface sites impact water and methanol adsorption. The adsorbates are stepwise desorbed from microporous MFI zeolites, mesoporous SBA-15 materials and amorphous silica supported silicotungstic acid (STA) in their isostructural siliceous, Na-, and H-forms. In the saturated

10. Conclusions and Outlook

state, liquid-like species are present and the quantities of adsorbates are controlled by surface areas and Si(OH) densities. For water and methanol saturation in Silicalite, a repulsive effect is observed, which is explained by the synergy of microporous confinement and hydrophobic Si-O-Si structure in crystalline Silicalite. Adsorbate-cation complexes are present in Na- and H-ZSM-5 at elevated temperatures, due to the confinement in micropores. However, such complexes are absent or dissociate fast under less confinement on Na- and H-forms of SBA-15 and STA materials. This observation indicates that confinement is essential for forming stable surface complexes in aluminum-containing materials. We find that Si(OH) groups can strongly bind methanol, which explains why side-reactions frequently occur if zeolite catalysts are rich in Si(OH) groups or defects. In addition, more methanol than water adsorbates binds at counter ions of ZSM-5, proving why methanol conversion continuously occurs on acidic zeolites.

In summary, we systematically investigated the NaAlO₂-modification of micro- and mesoporous silica. The alumination, combined with various confinements and surface sites, results in different acid properties and diverse adsorption properties for the parent and aluminated materials. This study helps to optimize catalysts for reactions with the co-presences of water and alcohol, such as biomass conversion. However, there are still some questions that can be further investigated:

(1) How do the surface sites and confinement influence the performance of active species when the silicates or aluminosilicates are used as support materials.

(2) In practice, how to rationally control the Si(OH) and defect-site densities on aluminosilicate catalysts is still a big problem that puzzle the scientists in zeolite synthesis area.

(3) Is it possible to synthesize mesoporous aluminosilicates with strong BAS is still unknown.

References

- [1] K. S. W. Sing, *Pure and Applied Chemistry*, 1985, **57**, 603-619.
- [2] <http://www.iza-structure.org/database>.
- [3] Y. Li, L. Li and J. Yu, *Chem*, 2017, **3**, 928-949.
- [4] M. Estermann, L. B. McCusker, C. Baerlocher, A. Merrouche and H. Kessler, *Nature*, 1991, **352**, 320-323.
- [5] M.-D. Jia, B. Chen, R. D. Noble and J. L. Falconer, *Journal of Membrane Science*, 1994, **90**, 1-10.
- [6] M. Pera-Titus, *Chemical Reviews*, 2014, **114**, 1413-1492.
- [7] M. R. Hudson, W. L. Queen, J. A. Mason, D. W. Fickel, R. F. Lobo and C. M. Brown, *Journal of the American Chemical Society*, 2012, **134**, 1970-1973.
- [8] Y. Li and J. Yu, *Chem Rev*, 2014, **114**, 7268-7316.
- [9] H. v. Koningsveld, *Compendium of Zeolite Framework Types: Building Schemes and Type Characteristics*, Elsevier, Amsterdam, 2007.
- [10] E. M. Gallego, M. T. Portilla, C. Paris, A. León-Escamilla, M. Boronat, M. Moliner and A. Corma, *Science*, 2017, **355**, 1051-1054.
- [11] G. R. L. Robert J Argauer, US3702886A, 1972.
- [12] Z. Wan, G. Li, C. Wang, H. Yang and D. Zhang, *Catalysis Today*, 2018, **314**, 107-113.
- [13] Q. Wen, J. Di, L. Jiang, J. Yu and R. Xu, *Chemical Science*, 2013, **4**, 591-595.
- [14] D. H. Olson, G. T. Kokotailo, S. L. Lawton and W. M. Meier, *The Journal of Physical Chemistry*, 1981, **85**, 2238-2243.
- [15] I. Díaz, E. Kokkoli, O. Terasaki and M. Tsapatsis, *Chemistry of Materials*, 2004, **16**, 5226-5232.
- [16] G. Bonilla, I. Díaz, M. Tsapatsis, H.-K. Jeong, Y. Lee and D. G. Vlachos, *Chemistry of Materials*, 2004, **16**, 5697-5705.
- [17] X. Zhang, D. Liu, D. Xu, S. Asahina, K. A. Cychosz, K. V. Agrawal, Y. Al Wahedi, A. Bhan, S. Al Hashimi, O. Terasaki, M. Thommes and M. Tsapatsis, *Science*, 2012, **336**, 1684-1687.
- [18] W. Dai, C. Kouvatas, W. Tai, G. Wu, N. Guan, L. Li and V. Valtchev, *Journal of the American Chemical Society*, 2021, **143**, 1993-2004.
- [19] G. Singh, J. Lee, A. Karakoti, R. Bahadur, J. Yi, D. Zhao, K. AlBahily and A. Vinu, *Chemical Society Reviews*, 2020, **49**, 4360-4404.
- [20] W. Zhu, Z. Chen, Y. Pan, R. Dai, Y. Wu, Z. Zhuang, D. Wang, Q. Peng, C. Chen and Y. Li, *Advanced Materials*, 2019, **31**, 1800426.
- [21] C. Perego and R. Millini, *Chemical Society Reviews*, 2013, **42**, 3956-3976.
- [22] W. Li, J. Liu and D. Zhao, *Nature Reviews Materials*, 2016, **1**, 16023.
- [23] T. Wagner, S. Haffer, C. Weinberger, D. Klaus and M. Tiemann, *Chemical Society Reviews*, 2013, **42**, 4036-4053.
- [24] D. Chen, Q. Xie and J. Zhu, *Accounts of Chemical Research*, 2019, **52**, 1449-1460.

References

- [25] B. Yang, Y. Chen and J. Shi, *Advanced Materials*, 2019, **31**, 1901778.
- [26] N. Linares, A. M. Silvestre-Albero, E. Serrano, J. Silvestre-Albero and J. García-Martínez, *Chemical Society Reviews*, 2014, **43**, 7681-7717.
- [27] J. Chmiola, G. Yushin, Y. Gogotsi, C. Portet, P. Simon and P. L. Taberna, *Science*, 2006, **313**, 1760-1763.
- [28] C. T. Kresge, M. E. Leonowicz, W. J. Roth, J. C. Vartuli and J. S. Beck, *Nature*, 1992, **359**, 710-712.
- [29] J. S. Beck, J. C. Vartuli, W. J. Roth, M. E. Leonowicz, C. T. Kresge, K. D. Schmitt, C. T. W. Chu, D. H. Olson, E. W. Sheppard, S. B. McCullen, J. B. Higgins and J. L. Schlenker, *Journal of the American Chemical Society*, 1992, **114**, 10834-10843.
- [30] C. T. Kresge, J. C. Vartuli, W. J. Roth and M. E. Leonowicz, in *Studies in Surface Science and Catalysis*, ed. O. Terasaki, Elsevier, 2004, vol. 148, pp. 53-72.
- [31] Q. Huo, R. Leon, P. M. Petroff and G. D. Stucky, *Science*, 1995, **268**, 1324-1327.
- [32] D. Zhao, Q. Huo, J. Feng, B. F. Chmelka and G. D. Stucky, *Journal of the American Chemical Society*, 1998, **120**, 6024-6036.
- [33] D. Zhao, J. Feng, Q. Huo, N. Melosh, G. H. Fredrickson, B. F. Chmelka and G. D. Stucky, *Science*, 1998, **279**, 548-552.
- [34] U. Ciesla and F. Schüth, *Microporous and Mesoporous Materials*, 1999, **27**, 131-149.
- [35] X. He and D. Antonelli, *Angewandte Chemie International Edition*, 2002, **41**, 214-229.
- [36] H. Guo, W. Xu, M.-H. Cui, N.-L. Yang and D. L. Akins, *Chemical Communications*, 2003, 1432-1433.
- [37] Z. Luan, M. Hartmann, D. Zhao, W. Zhou and L. Kevan, *Chemistry of Materials*, 1999, **11**, 1621-1627.
- [38] A. S. Maria Chong, X. S. Zhao, A. T. Kustedjo and S. Z. Qiao, *Microporous and Mesoporous Materials*, 2004, **72**, 33-42.
- [39] J. Lei, J. Fan, C. Yu, L. Zhang, S. Jiang, B. Tu and D. Zhao, *Microporous and Mesoporous Materials*, 2004, **73**, 121-128.
- [40] G. Kickelbick, *Angewandte Chemie International Edition*, 2004, **43**, 3102-3104.
- [41] S. Inagaki, S. Guan, Y. Fukushima, T. Ohsuna and O. Terasaki, *Journal of the American Chemical Society*, 1999, **121**, 9611-9614.
- [42] T. Asefa, M. J. MacLachlan, N. Coombs and G. A. Ozin, *Nature*, 1999, **402**, 867-871.
- [43] Y. Yue, A. Gédéon, J.-L. Bonardet, J.-B. D'Espinose, J. Fraissard and N. Melosh, *Chemical Communications*, 1999, 1967-1968.
- [44] S. Wu, Y. Han, Y.-C. Zou, J.-W. Song, L. Zhao, Y. Di, S.-Z. Liu and F.-S. Xiao, *Chemistry of Materials*, 2004, **16**, 486-492.
- [45] Y. Li, Q. Yang, J. Yang and C. Li, *Journal of Porous Materials*, 2006, **13**, 187-193.
- [46] S. Sumiya, Y. Oumi, T. Uozumi and T. Sano, *Journal of Materials Chemistry*, 2001, **11**, 1111-1115.
- [47] S.-R. Zhai, L. Wei, F.-Z. Qu and S.-J. Wang, *Journal of the Chinese Chemical Society*, 2006, **53**, 1053-1058.

References

- [48] S. Lang, M. Benz, U. Obenaus, R. Himmelmann, M. Scheibe, E. Klemm, J. Weitkamp and M. Hunger, *Topics in Catalysis*, 2017, **60**, 1537-1553.
- [49] H. Kloepfer, Germany Pat., DE000000762723A, 1942.
- [50] S. E. Pratsinis, *Progress in Energy and Combustion Science*, 1998, **24**, 197-219.
- [51] N. Ibaseta and B. Biscans, *Powder Technology*, 2010, **203**, 206-210.
- [52] W. Stöber, A. Fink and E. Bohn, *Journal of Colloid and Interface Science*, 1968, **26**, 62-69.
- [53] T. Yokoi, J. Wakabayashi, Y. Otsuka, W. Fan, M. Iwama, R. Watanabe, K. Aramaki, A. Shimojima, T. Tatsumi and T. Okubo, *Chemistry of Materials*, 2009, **21**, 3719-3729.
- [54] K. Osseo-Asare and F. J. Arriagada, *Colloids and Surfaces*, 1990, **50**, 321-339.
- [55] F. Venditti, R. Angelico, G. Palazzo, G. Colafemmina, A. Ceglie and F. Lopez, *Langmuir*, 2007, **23**, 10063-10068.
- [56] R. P. Bagwe, L. R. Hilliard and W. Tan, *Langmuir*, 2006, **22**, 4357-4362.
- [57] X. He, H. Nie, K. Wang, W. Tan, X. Wu and P. Zhang, *Analytical Chemistry*, 2008, **80**, 9597-9603.
- [58] S. Legrand, A. Catheline, L. Kind, E. C. Constable, C. E. Housecroft, L. Landmann, P. Banse, U. Pieleles and A. Wirth-Heller, *New Journal of Chemistry*, 2008, **32**, 588-593.
- [59] H. Kanai, Y. Okumura, K. Utani, K. Hamada and S. Imamura, *Catalysis Letters*, 2001, **76**, 207-211.
- [60] R. Himmelmann, E. Klemm and M. Dyballa, *Catalysis Science & Technology*, 2021, **11**, 3098-3108.
- [61] P. Burattin, M. Che and C. Louis, *The Journal of Physical Chemistry B*, 1999, **103**, 6171-6178.
- [62] C. P. Slichter, *Principles of Magnetic Resonance*, Springer Berlin Heidelberg, 2010.
- [63] J. M. Thomas and J. Klinowski, in *Advances in Catalysis*, eds. D. D. Eley, H. Pines and P. B. Weisz, Academic Press, 1985, vol. 33, pp. 199-374.
- [64] M. Mehring, *High Resolution NMR Spectroscopy in Solids*, Springer Berlin Heidelberg, 2012.
- [65] E. R. Andrew, A. Bradbury and R. G. Eades, *Nature*, 1958, **182**, 1659-1659.
- [66] D. Schulze, H. Ernst, D. Fenzke, W. Meiler and H. Pfeifer, *The Journal of Physical Chemistry*, 1990, **94**, 3499-3502.
- [67] G. Paul, C. Bisio, I. Braschi, M. Cossi, G. Gatti, E. Gianotti and L. Marchese, *Chemical Society Reviews*, 2018, **47**, 5684-5739.
- [68] G. Mestl and H. Knözinger, in *Handbook of Heterogeneous Catalysis*, 2008, pp. 932-971.
- [69] E. Brunner, H. G. Karge and H. Pfeifer, *Zeitschrift für Physikalische Chemie*, 1992, **176**, 173-183.
- [70] NETZSCH, *Journal*.
- [71] M. Ghamami and L. B. Sand, *Zeolites*, 1983, **3**, 155-162.
- [72] M. Dyballa, P. Becker, D. Trefz, E. Klemm, A. Fischer, H. Jakob and M. Hunger,

References

- Applied Catalysis A: General*, 2016, **510**, 233-243.
- [73] V. Meynen, P. Cool and E. F. Vansant, *Microporous and Mesoporous Materials*, 2009, **125**, 170-223.
- [74] J. F. Haw, M. B. Hall, A. E. Alvarado-Swaisgood, E. J. Munson, Z. Lin, L. W. Beck and T. Howard, *Journal of the American Chemical Society*, 1994, **116**, 7308-7318.
- [75] Y. Jiang, J. Huang, W. Dai and M. Hunger, *Solid State Nuclear Magnetic Resonance*, 2011, **39**, 116-141.
- [76] W. Dai, X. Sun, B. Tang, G. Wu, L. Li, N. Guan and M. Hunger, *Journal of Catalysis*, 2014, **314**, 10-20.
- [77] J. Jänchen, J. H. M. C. van Wolput, L. J. M. van de Ven, J. W. de Haan and R. A. van Santen, *Catalysis Letters*, 1996, **39**, 147-152.
- [78] E. B. Whipple, P. J. Green, M. Ruta and R. L. Bujalski, *The Journal of Physical Chemistry*, 1976, **80**, 1350-1356.
- [79] S. Lang, M. Benz, U. Obenaus, R. Himmelmann and M. Hunger, *ChemCatChem*, 2016, **8**, 2031-2036.
- [80] D. Massiot, F. Fayon, M. Capron, I. King, S. Le Calvé, B. Alonso, J.-O. Durand, B. Bujoli, Z. Gan and G. Hoatson, *Magnetic Resonance in Chemistry*, 2002, **40**, 70-76.
- [81] J.-P. Amoureux, C. Fernandez and S. Steuernagel, *Journal of Magnetic Resonance, Series A*, 1996, **123**, 116-118.
- [82] H. Kim, H. J. Cho, S. Narayanan, S. Yang, H. Furukawa, S. Schiffres, X. Li, Y.-B. Zhang, J. Jiang, O. M. Yaghi and E. N. Wang, *Scientific Reports*, 2016, **6**, 19097.
- [83] J. Scherzer and J. L. Bass, *Journal of Catalysis*, 1977, **46**, 100-108.
- [84] D. Freude, E. Brunner, H. Pfeifer, D. Prager, H. G. Jerschkewitz, U. Lohse and G. Oehlmann, *Chemical Physics Letters*, 1987, **139**, 325-330.
- [85] Y. Fan, X. Lin, G. Shi, H. Liu and X. Bao, *Microporous and Mesoporous Materials*, 2007, **98**, 174-181.
- [86] A. Corma, *Chemical Reviews*, 1997, **97**, 2373-2420.
- [87] A. J. J. Koekkoek, J. A. R. van Veen, P. B. Gerttisen, P. Giltay, P. C. M. M. Magusin and E. J. M. Hensen, *Microporous and Mesoporous Materials*, 2012, **151**, 34-43.
- [88] Y. Li, W. Zhang, L. Zhang, Q. Yang, Z. Wei, Z. Feng and C. Li, *The Journal of Physical Chemistry B*, 2004, **108**, 9739-9744.
- [89] H.-M. Kao, C.-C. Ting and S.-W. Chao, *Journal of Molecular Catalysis A: Chemical*, 2005, **235**, 200-208.
- [90] Z. Zhang, X. Liu, Y. Xu and R. Xu, *Zeolites*, 1991, **11**, 232-238.
- [91] H. Hamdan, S. Endud, H. He, M. N. M. Muhid and J. Klinowski, *Journal of the Chemical Society, Faraday Transactions*, 1996, **92**, 2311-2315.
- [92] Z. Talha, C. Bachir, S. Ziri, S. Bellahouel, A. Bengueddach, F. Villières, M. Pelletier, P. G. Weidler and R. Hamacha, *Catalysis Letters*, 2017, **147**, 2116-2126.
- [93] W. Hu, Q. Luo, Y. Su, L. Chen, Y. Yue, C. Ye and F. Deng, *Microporous and Mesoporous Materials*, 2006, **92**, 22-30.
- [94] A. Galarneau, M. Nader, F. Guenneau, F. Di Renzo and A. Gedeon, *The Journal of*

References

- Physical Chemistry C*, 2007, **111**, 8268-8277.
- [95] Y. Sakamoto, M. Kaneda, O. Terasaki, D. Y. Zhao, J. M. Kim, G. Stucky, H. J. Shin and R. Ryoo, *Nature*, 2000, **408**, 449-453.
- [96] A. H. Janssen, A. J. Koster and K. P. de Jong, *Angewandte Chemie International Edition*, 2001, **40**, 1102-1104.
- [97] A. H. Janssen, A. J. Koster and K. P. de Jong, *The Journal of Physical Chemistry B*, 2002, **106**, 11905-11909.
- [98] A. Corma, in *Studies in Surface Science and Catalysis*, eds. P. A. Jacobs and R. A. van Santen, Elsevier, 1989, vol. 49, pp. 49-67.
- [99] P. Kortunov, S. Vasenkov, J. Kärger, R. Valiullin, P. Gottschalk, M. Fé Elía, M. Perez, M. Stöcker, B. Drescher, G. McElhiney, C. Berger, R. Gläser and J. Weitkamp, *Journal of the American Chemical Society*, 2005, **127**, 13055-13059.
- [100] M. Dybala, U. Obenaus, M. Rosenberger, A. Fischer, H. Jakob, E. Klemm and M. Hunger, *Microporous and Mesoporous Materials*, 2016, **233**, 26-30.
- [101] M. Dybala, U. Obenaus, M. Blum and W. Dai, *Catalysis Science & Technology*, 2018, **8**, 4440-4449.
- [102] A. Zukal, J. Mayerová and J. Čejka, *Physical Chemistry Chemical Physics*, 2010, **12**, 5240-5247.
- [103] A. Takahashi, R. T. Yang, C. L. Munson and D. Chinn, *Langmuir*, 2001, **17**, 8405-8413.
- [104] J. Klinowski, S. Ramdas, J. M. Thomas, C. A. Fyfe and J. S. Hartman, *Journal of the Chemical Society, Faraday Transactions 2: Molecular and Chemical Physics*, 1982, **78**, 1025-1050.
- [105] J. Klinowski, J. M. Thomas, C. A. Fyfe, G. C. Gobbi and J. S. Hartman, *Inorganic Chemistry*, 1983, **22**, 63-66.
- [106] G. Engelhardt, B. Fahlke, M. Mägi and E. Lippmaa, *Zeolites*, 1983, **3**, 292-294.
- [107] C. A. Fyfe, Y. Feng, H. Grondey, G. T. Kokotailo and H. Gies, *Chemical Reviews*, 1991, **91**, 1525-1543.
- [108] C. A. Fyfe, J. M. Thomas, J. Klinowski and G. C. Gobbi, *Angew Chem Int Ed Engl*, 1983, **22**, 259-336.
- [109] E. Lippmaa, M. Maegi, A. Samoson, G. Engelhardt and A. R. Grimmer, *Journal of the American Chemical Society*, 1980, **102**, 4889-4893.
- [110] E. Lippmaa, M. Mägi, A. Samoson, M. Tarmak and G. Engelhard, *J Am Chem Soc*, 1981, **103**, 4492-4496.
- [111] G. Engelhardt, W. Altenburg, D. Hoebbel and W. Wieker, *Zeitschrift für anorganische und allgemeine Chemie*, 1977, **428**, 43-52.
- [112] G. Engelhardt, U. Lohse, A. Samoson, M. Mägi, M. Tarmak and E. Lippmaa, *Zeolites*, 1982, **2**, 59-62.
- [113] D. Margolese, J. A. Melero, S. C. Christiansen, B. F. Chmelka and G. D. Stucky, *Chemistry of Materials*, 2000, **12**, 2448-2459.
- [114] A. Madani, A. Aznar, J. Sanz and J. M. Serratos, *The Journal of Physical Chemistry*, 1990, **94**, 760-765.

References

- [115] S. F. Dec, G. E. Maciel and J. J. Fitzgerald, *Journal of the American Chemical Society*, 1990, **112**, 9069-9077.
- [116] A. Omega, J. A. van Bokhoven and R. Prins, *The Journal of Physical Chemistry B*, 2003, **107**, 8854-8860.
- [117] A. Samoson, E. Lippmaa, G. Engelhardt, U. Lohse and H. G. Jerschke, *Chemical Physics Letters*, 1987, **134**, 589-592.
- [118] M. J. Remy, D. Stanica, G. Poncelet, E. J. P. Feijen, P. J. Grobet, J. A. Martens and P. A. Jacobs, *The Journal of Physical Chemistry*, 1996, **100**, 12440-12447.
- [119] Q. Luo, F. Deng, Z. Yuan, J. Yang, M. Zhang, Y. Yue and C. Ye, *The Journal of Physical Chemistry B*, 2003, **107**, 2435-2442.
- [120] X. Yi, H.-H. Ko, F. Deng, S.-B. Liu and A. Zheng, *Nature Protocols*, 2020, **15**, 3527-3555.
- [121] A. Zheng, S.-B. Liu and F. Deng, *Chemical Reviews*, 2017, **117**, 12475-12531.
- [122] P. V. Wiper, J. Amelse and L. Mafra, *Journal of Catalysis*, 2014, **316**, 240-250.
- [123] U. Obenaus, M. Dyballa, S. Lang, M. Scheibe and M. Hunger, *The Journal of Physical Chemistry C*, 2015, **119**, 15254-15262.
- [124] D. J. Zaleski, P. J. Chu, P. N. Tutunjian and J. H. Lunsford, *Langmuir*, 1989, **5**, 1026-1030.
- [125] E. F. Rakiewicz, A. W. Peters, R. F. Wormsbecher, K. J. Sutovich and K. T. Mueller, *The Journal of Physical Chemistry B*, 1998, **102**, 2890-2896.
- [126] Q. Zhao, W.-H. Chen, S.-J. Huang, Y.-C. Wu, H.-K. Lee and S.-B. Liu, *The Journal of Physical Chemistry B*, 2002, **106**, 4462-4469.
- [127] S. Xin, Q. Wang, J. Xu, Y. Chu, P. Wang, N. Feng, G. Qi, J. Trébosc, O. Lafon, W. Fan and F. Deng, *Chemical Science*, 2019, **10**, 10159-10169.
- [128] C. Bornes, M. Sardo, Z. Lin, J. Amelse, A. Fernandes, M. F. Ribeiro, C. Geraldes, J. Rocha and L. Mafra, *Chemical Communications*, 2019, **55**, 12635-12638.
- [129] Y. Zhi, H. Shi, L. Mu, Y. Liu, D. Mei, D. M. Camaioni and J. A. Lercher, *Journal of the American Chemical Society*, 2015, **137**, 15781-15794.
- [130] Q. Wang, H. Fan, S. Wu, Z. Zhang, P. Zhang and B. Han, *Green Chemistry*, 2012, **14**, 1152-1158.
- [131] K. Chen, J. Damron, C. Pearson, D. Resasco, L. Zhang and J. L. White, *ACS Catalysis*, 2014, **4**, 3039-3044.
- [132] Y. Liu, A. Vjunov, H. Shi, S. Eckstein, D. M. Camaioni, D. Mei, E. Baráth and J. A. Lercher, *Nature Communications*, 2017, **8**, 14113.
- [133] R. Weng, Z. Yu, J. Xiong and X. Lu, *Green Chemistry*, 2020, **22**, 3013-3027.
- [134] S. Eckstein, P. H. Hintermeier, M. V. Olarte, Y. Liu, E. Baráth and J. A. Lercher, *Journal of Catalysis*, 2017, **352**, 329-336.
- [135] G. N. Kalantzopoulos, F. Lundvall, K. Thorshaug, A. Lind, P. Vajeeston, I. Dovgaliuk, B. Arstad, D. S. Wragg and H. Fjellvåg, *Chemistry of Materials*, 2020, **32**, 1495-1505.
- [136] S. Proding, M. A. Derewinski, A. Vjunov, S. D. Burton, I. Arslan and J. A. Lercher, *Journal of the American Chemical Society*, 2016, **138**, 4408-4415.

References

- [137] S. J. Freakley, N. Dimitratos, D. J. Willock, S. H. Taylor, C. J. Kiely and G. J. Hutchings, *Accounts of Chemical Research*, 2021, **54**, 2614-2623.
- [138] M. Dyballa, D. K. Pappas, K. Kvande, E. Borfecchia, B. Arstad, P. Beato, U. Olsbye and S. Svelle, *ACS Catalysis*, 2019, **9**, 365-375.
- [139] I. Yarulina, A. D. Chowdhury, F. Meirer, B. M. Weckhuysen and J. Gascon, *Nature Catalysis*, 2018, **1**, 398-411.
- [140] H. Pfeifer, D. Freude and M. Hunger, *Zeolites*, 1985, **5**, 274-286.
- [141] H. E. Gottlieb, V. Kotlyar and A. Nudelman, *The Journal of Organic Chemistry*, 1997, **62**, 7512-7515.
- [142] P. H. Kasai and P. M. Jones, *Journal of Molecular Catalysis*, 1984, **27**, 81-93.
- [143] M. Wang, N. R. Jaegers, M.-S. Lee, C. Wan, J. Z. Hu, H. Shi, D. Mei, S. D. Burton, D. M. Camaioni, O. Y. Gutiérrez, V.-A. Glezakou, R. Rousseau, Y. Wang and J. A. Lercher, *Journal of the American Chemical Society*, 2019, **141**, 3444-3455.
- [144] M. W. Anderson, J. Klinowski and P. J. Barrie, *The Journal of Physical Chemistry*, 1991, **95**, 235-239.
- [145] J. P. Chauvel and N. S. True, *Chemical Physics*, 1985, **95**, 435-441.
- [146] E. M. Flanigen, J. M. Bennett, R. W. Grose, J. P. Cohen, R. L. Patton, R. M. Kirchner and J. V. Smith, *Nature*, 1978, **271**, 512-516.
- [147] T. Schmeling and K. Strey, *Berichte der Bunsengesellschaft für physikalische Chemie*, 1983, **87**, 871-874.
- [148] B. Hunger, M. Heuchel, S. Matysik, K. Beck and W. D. Einicke, *Thermochimica Acta*, 1995, **269-270**, 599-611.
- [149] B. Hunger, S. Matysik, M. Heuchel and W.-D. Einicke, *Langmuir*, 1997, **13**, 6249-6254.
- [150] C. C. Lee, R. J. Gorte and W. E. Farneth, *The Journal of Physical Chemistry B*, 1997, **101**, 3811-3817.
- [151] C. G. Pope, *Journal of the Chemical Society, Faraday Transactions*, 1993, **89**, 1139-1141.
- [152] M. Hunger and T. Horvath, *Berichte der Bunsengesellschaft für physikalische Chemie*, 1995, **99**, 1316-1320.
- [153] F. Haase and J. Sauer, *The Journal of Physical Chemistry*, 1994, **98**, 3083-3085.
- [154] M. Hunger, U. Schenk, M. Breuninger, R. Gläser and J. Weitkamp, *Microporous and Mesoporous Materials*, 1999, **27**, 261-271.
- [155] M. Xu, W. Wang, M. Seiler, A. Buchholz and M. Hunger, *The Journal of Physical Chemistry B*, 2002, **106**, 3202-3208.
- [156] K. Zhang, R. P. Lively, J. D. Noel, M. E. Dose, B. A. McCool, R. R. Chance and W. J. Koros, *Langmuir*, 2012, **28**, 8664-8673.
- [157] M. Hunger and T. Horvath, *Journal of the American Chemical Society*, 1996, **118**, 12302-12308.
- [158] C.-j. Liu, J. Ye, J. Jiang and Y. Pan, *ChemCatChem*, 2011, **3**, 529-541.
- [159] C. Hammond, M. M. Forde, M. H. Ab Rahim, A. Thetford, Q. He, R. L. Jenkins, N. Dimitratos, J. A. Lopez-Sanchez, N. F. Dummer, D. M. Murphy, A. F. Carley, S. H.

References

- Taylor, D. J. Willock, E. E. Stangland, J. Kang, H. Hagen, C. J. Kiely and G. J. Hutchings, *Angewandte Chemie International Edition*, 2012, **51**, 5129-5133.
- [160] B. Cañete, C. E. Gigola and N. B. Brignole, *Industrial & Engineering Chemistry Research*, 2014, **53**, 7103-7112.
- [161] W. Wang, S. Wang, X. Ma and J. Gong, *Chemical Society Reviews*, 2011, **40**, 3703-3727.
- [162] G. W. Huber, S. Iborra and A. Corma, *Chemical Reviews*, 2006, **106**, 4044-4098.
- [163] P. Tian, Y. Wei, M. Ye and Z. Liu, *ACS Catalysis*, 2015, **5**, 1922-1938.
- [164] A. D. Chowdhury, K. Houben, G. T. Whiting, M. Mokhtar, A. M. Asiri, S. A. Al-Thabaiti, S. N. Basahel, M. Baldus and B. M. Weckhuysen, *Angewandte Chemie International Edition*, 2016, **55**, 15840-15845.
- [165] S. Lin, Y. Zhi, W. Chen, H. Li, W. Zhang, C. Lou, X. Wu, S. Zeng, S. Xu, J. Xiao, A. Zheng, Y. Wei and Z. Liu, *Journal of the American Chemical Society*, 2021, **143**, 12038-12052.
- [166] K. Barbera, F. Bonino, S. Bordiga, T. V. W. Janssens and P. Beato, *Journal of Catalysis*, 2011, **280**, 196-205.
- [167] G. Mirth, J. A. Lercher, M. W. Anderson and J. Klinowski, *Journal of the Chemical Society, Faraday Transactions*, 1990, **86**, 3039-3044.
- [168] F. Salehirad and M. W. Anderson, *Journal of Catalysis*, 1998, **177**, 189-207.
- [169] J. Kotrla, D. Nachtigallová, L. Kubelková, L. Heeribout, C. Doremieux-Morin and J. Fraissard, *The Journal of Physical Chemistry B*, 1998, **102**, 2454-2463.
- [170] V. Mouarrawis, R. Plessius, J. I. van der Vlugt and J. N. H. Reek, *Frontiers in Chemistry*, 2018, **6**.
- [171] E. E. Santiso, M. K. Kostov, A. M. George, M. B. Nardelli and K. E. Gubbins, *Applied Surface Science*, 2007, **253**, 5570-5579.
- [172] W. Dai, C. Wang, X. Yi, A. Zheng, L. Li, G. Wu, N. Guan, Z. Xie, M. Dybala and M. Hunger, *Angewandte Chemie International Edition*, 2015, **54**, 8783-8786.
- [173] M. Huang, Q. Wang, X. Yi, Y. Chu, W. Dai, L. Li, A. Zheng and F. Deng, *Chemical Communications*, 2016, **52**, 10606-10608.
- [174] P. Ferri, C. Li, C. Paris, A. Rodríguez-Fernández, M. Moliner, M. Boronat and A. Corma, *ChemCatChem*, 2021, **13**, 1578-1586.
- [175] B. Grünberg, T. Emmler, E. Gedat, I. Shenderovich, G. H. Findenegg, H.-H. Limbach and G. Buntkowsky, *Chemistry – A European Journal*, 2004, **10**, 5689-5696.
- [176] I. V. Kozhevnikov, *Chemical Reviews*, 1998, **98**, 171-198.
- [177] V. Bolis, C. Busco, S. Bordiga, P. Ugliengo, C. Lamberti and A. Zecchina, *Applied Surface Science*, 2002, **196**, 56-70.
- [178] T. R. Forester and R. F. Howe, *Journal of the American Chemical Society*, 1987, **109**, 5076-5082.
- [179] Z. Li, C. Rieg, A.-K. Beurer, M. Benz, J. Bender, C. Schneck, Y. Traa, M. Dybala and M. Hunger, *Adsorption*, 2021, **27**, 49-68.
- [180] T. Zhou, P. Bai, J. I. Siepmann and A. E. Clark, *The Journal of Physical Chemistry C*,

References

- 2017, **121**, 22015-22024.
- [181] A. Zachariou, A. P. Hawkins, R. F. Howe, N. Barrow, J. Bradley, P. Collier, D. Lennon and S. F. Parker, *Topics in Catalysis*, 2021, **64**, 672-684.
- [182] A. Ison and R. J. Gorte, *Journal of Catalysis*, 1984, **89**, 150-158.
- [183] S. M. Campbell, X.-Z. Jiang and R. F. Howe, *Microporous and Mesoporous Materials*, 1999, **29**, 91-108.
- [184] I. I. Ivanova and A. Corma, *The Journal of Physical Chemistry B*, 1997, **101**, 547-551.
- [185] W. Wang, M. Seiler and M. Hunger, *The Journal of Physical Chemistry B*, 2001, **105**, 12553-12558.
- [186] W. Wang, A. Buchholz, M. Seiler and M. Hunger, *Journal of the American Chemical Society*, 2003, **125**, 15260-15267.
- [187] W. Wang, A. Buchholz, A. Arnold, M. Xu and M. Hunger, *Chemical Physics Letters*, 2003, **370**, 88-93.
- [188] E. P. L. Hunter and S. G. Lias, *Journal of Physical and Chemical Reference Data*, 1998, **27**, 413-656.
- [189] G. Qi, Y. Chu, Q. Wang, X. Wang, Y. Li, J. Trébosc, O. Lafon, J. Xu and F. Deng, *Angewandte Chemie International Edition*, 2020, **59**, 19532-19538.
- [190] Y. Liu, F. M. Kirchberger, S. Müller, M. Eder, M. Tonigold, M. Sanchez-Sanchez and J. A. Lercher, *Nature Communications*, 2019, **10**, 1462.
- [191] Q. Meng, D. Cao, G. Zhao, C. Qiu, X. Liu, X. Wen, Y. Zhu and Y. Li, *Applied Catalysis B: Environmental*, 2017, **212**, 15-22.
- [192] K. Chen, J. Kelsey, J. L. White, L. Zhang and D. Resasco, *ACS Catalysis*, 2015, **5**, 7480-7487.
- [193] P. Batamack, C. Doremieux-Morin, J. Fraissard and D. Freude, *The Journal of Physical Chemistry*, 1991, **95**, 3790-3796.
- [194] M. Hunger, D. Freude and H. Pfeifer, *Journal of the Chemical Society, Faraday Transactions*, 1991, **87**, 657-662.
- [195] S. Senapati and A. Chandra, *The Journal of Physical Chemistry B*, 2001, **105**, 5106-5109.
- [196] H. K. Christenson, *Journal of Physics: Condensed Matter*, 2001, **13**, R95-R133.
- [197] T. Takei, K. Mukasa, M. Kofuji, M. Fuji, T. Watanabe, M. Chikazawa and T. Kanazawa, *Colloid and Polymer Science*, 2000, **278**, 475-480.
- [198] E. Grifoni, G. Piccini, J. A. Lercher, V.-A. Glezakou, R. Rousseau and M. Parrinello, *Nature Communications*, 2021, **12**, 2630.
- [199] R. Gounder and E. Iglesia, *Chemical Communications*, 2013, **49**, 3491-3509.
- [200] S. Le Caër, S. Pin, S. Esnouf, Q. Raffy, J. P. Renault, J. B. Brubach, G. Creff and P. Roy, *Physical Chemistry Chemical Physics*, 2011, **13**, 17658-17666.
- [201] J. Haber, K. Pamin, L. Matachowski, B. Napruszewska and J. Połtowicz, *Journal of Catalysis*, 2002, **207**, 296-306.
- [202] R. Al-Faze, A. Finch, E. F. Kozhevnikova and I. V. Kozhevnikov, *Applied Catalysis A: General*, 2020, **597**, 117549.

References

- [203] R. D. Nelson, D. R. Lide, A. A. Maryott, *Selected Values of Electric Dipole Moments for Molecules in the Gas Phase*, U.S. National Bureau of Standards, 1967.
- [204] M. Trzpit, M. Soulard, J. Patarin, N. Desbiens, F. Cailliez, A. Boutin, I. Demachy and A. H. Fuchs, *Langmuir*, 2007, **23**, 10131-10139.
- [205] C. E. Bronnimann, R. C. Zeigler and G. E. Maciel, *Journal of the American Chemical Society*, 1988, **110**, 2023-2026.
- [206] H. Koller, R. F. Lobo, S. L. Burkett and M. E. Davis, *The Journal of Physical Chemistry*, 1995, **99**, 12588-12596.
- [207] Z. Li, C. Rieg, A.-K. Beurer, M. Benz, J. Bender, C. Schneck, Y. Traa, M. Dyballa and M. Hunger, *Adsorption*, 2021, **27**, 49-68.
- [208] A. Zecchina, F. Geobaldo, G. Spoto, S. Bordiga, G. Ricchiardi, R. Buzzoni and G. Petrini, *The Journal of Physical Chemistry*, 1996, **100**, 16584-16599.
- [209] K. Hadjiivanov, in *Advances in Catalysis*, ed. F. C. Jentoft, Academic Press, 2014, vol. 57, pp. 99-318.
- [210] K. M. Rao, R. Gobetto, A. Iannibello and A. Zecchina, *Journal of Catalysis*, 1989, **119**, 512-516.
- [211] F. Haase and J. Sauer, *Journal of the American Chemical Society*, 1995, **117**, 3780-3789.
- [212] M. Stöcker, *Microporous and Mesoporous Materials*, 1999, **29**, 3-48.
- [213] U. Olsbye, S. Svelle, M. Bjørgen, P. Beato, T. V. W. Janssens, F. Joensen, S. Bordiga and K. P. Lillerud, *Angewandte Chemie International Edition*, 2012, **51**, 5810-5831.

List of Publications

Li, Z.; Rieg, C.; Beurer, A.-K.; Benz, M.; Bender, J.; Schneck, C.; Traa, Y.; Dyballa, M.; Hunger, M., Effect of aluminum and sodium on the sorption of water and methanol in microporous MFI-type zeolites and mesoporous SBA-15 materials. *Adsorption* **2020**, *27* (1), 49-68.

Dyballa, M.; Rieg, C.; Dittmann, D.; Li, Z.; Buchmeiser, M.; Plietker, B.; Hunger, M., Potential of triphenylphosphine as solid-state NMR probe for studying the noble metal distribution on porous supports. *Microporous and Mesoporous Materials* **2020**, *293*, 109778.

Li, Z.; Benz, M.; Rieg, C.; Dittmann, D.; Beurer, A.-K.; Häussermann, D.; Arstad, B.; Dyballa, M., The alumination mechanism of porous silica materials and properties of derived ion exchangers and acid catalysts. *Materials Chemistry Frontiers* **2021**, *5* (11), 4254-4271.

Rieg, C.; Li, Z.; Kurtz, A.; Schmidt, M.; Dittmann, D.; Benz, M.; Dyballa, M., A Method for the Selective Quantification of Brønsted acid sites on external surfaces and in mesopores of hierarchical zeolites. *The Journal of Physical Chemistry C* **2021**, *125* (1), 515-525.

Nguyen, H. H.; Li, Z.; Enenkel, T.; Hildebrand, J.; Bauer, M.; Dyballa, M.; Estes, D. P., Probing the interactions of immobilized ruthenium dihydride complexes with metal oxide surfaces by MAS NMR: effects on CO₂ hydrogenation. *The Journal of Physical Chemistry C* **2021**, *125* (27), 14627-14635.

Rieg, C.; Dittmann, D.; Li, Z.; Kurtz, A.; Lorenz, I.; Estes, D. P.; Buchmeiser, M.; Dyballa, M.; Hunger, M., Noble metal location in porous supports determined by reaction with phosphines. *Microporous and Mesoporous Materials* **2021**, *310*, 110594.

Rieg, C.; Dittmann, D.; Li, Z.; Lawitzki, R.; Gugeler, K.; Maier, S.; Schmitz, G.; Kästner, J.; Estes, D. P.; Dyballa, M., Quantitative distinction between noble metals located in mesopores from those on the external surface. *Chemistry – A European Journal* **2021**, *27* (68), 17012-17023.

Maier, S.; Cronin, S. P.; Vu Dinh, M. A.; Li, Z.; Dyballa, M.; Nowakowski, M.; Bauer, M.; Estes, D. P., Immobilized platinum hydride species as catalysts for olefin isomerizations and enyne cycloisomerizations. *Organometallics* **2021**, *40* (11), 1751-1757.

List of Publications

Li, Z.; Dittmann, D.; Rieg, C.; Benz, M.; Dyballa, M., Confinement and surface sites control methanol adsorbate stability on MFI zeolites, SBA-15, and a silica-supported heteropoly acid. *Catalysis Science & Technology* **2022**, *12* (7), 2265-2277.

Li, Z.; Dittmann, D.; Rieg, C.; Benz, M.; Dyballa, M., Hydronium Ion and Water Complexes vs. Methanol on Solid Catalyst Surfaces: How Confinement Determines Stability and Reactivity. *Catalysis Science & Technology* **2022**, *12* (16), 5189-5202.

Acknowledgment

I firstly want to express my profound gratitude to my supervisors Dr. Michael Dyballa and Prof. Dr. Michael Hunger for giving me the opportunity to study in the solid-state NMR group and for their trustworthy instructions during my Ph.D. study.

I am also grateful to the Collaborative Research Center 1333 and German Research Foundation for the financial supporting during my whole Ph.D. period.

I would like to express my sincerest thanks to Prof. Deven Estes, Prof. Elisa Klemm and Prof. Thomas Schleid for their readiness for my Ph.D. examiners.

I sincerely thank all colleagues in the NMR group, Liu Yang, Carolin Rieg, Michael Benz, Daniel Dittmann, Alan Kurtz, and Elif Kaya, for their help during these four years.

I would like to give my special thanks to Dr. Hang Liu and Dr. Caiyun Xu for our friendship and happy times.

I would also like to thank all the colleagues in our institute, Mrs. E. Favaro, Prof. Dr. Y. Traa, H. Fingerle, B. Gehring, I. Lauerwald, I. Nägele, A. N. Merdanoglu, Dr. H. Zuo, A.-K. Beuer, D. Häussermann, Dr. Q. Song, H.-H. Nguyen, M. Schmidt, J. Florenski, M. Oßkopp, J. Hildebrand, S. Maier E. Wimmer and so on for their kindness help during these years.

At the end, I would like to show my deepest gratitude to my dear wife Junli and my cute son Caicheng. Without your accompany and encouragement, I cannot finish this degree.

Curriculum Vitae

Personal Data

Name: Zheng Li
Birth: January 1, 1992, Shanxi, China
Nationality: Chinese

Education

2010-2014 Study at the College of Chemistry and Chemical Engineering, Taiyuan University of Technology, Taiyuan, China (B. Eng.).
2015-2018 Study at Institute of Coal Chemistry, Chinese Academy of Sciences, Taiyuan, China, supervised by Prof. Dr.-Ing Xianglin Hou (M. Eng.).
2018-2022 Study at the Institute of Chemical Technology, University of Stuttgart, Stuttgart, Germany, supervised by Prof. Dr. Michael Hunger, Dr. Michael Dyballa and Jun. Prof. Dr. Deven Estes (Ph.D.).

Employment

2014-2015 Research Associate in the Institute of Coal Chemistry, Chinese Academy of Sciences, Taiyuan, China.